UNIVERSITÀ DEGLI STUDI DI MILANO

Scuola di Dottorato in Fisica, Astrofisica e Fisica Applicata

Dipartimento di Fisica

Corso di Dottorato in Fisica, Astrofisica e Fisica Applicata

Ciclo XXXV

Beta decay studies as a tool to investigate nuclear structure in the n-rich Po-Fr region and in p-rich Cd isotopes

Settore Scientifico Disciplinare FIS/04

Supervisor: Prof. Angela BRACCO

Co-supervisor: Dr. Giovanna BENZONI

Coordinator: Prof. Matteo PARIS

Tesi di Dottorato di:

Marta POLETTINI

Anno Accademico 2021-2022

Referees of the thesis:

Dr Adriana Nannini
INFN Sezione di Firenze, IT-50019 Firenze, Italy

Dr Maria Kmiecik
Institute of Nuclear Physics Polish Academy of Sciences, Radzikowskiego 152, PL-31342 Krakow, Poland

Commission of the final examination:

Prof. Angela Bracco
Dipartimento di Fisica, Università degli Studi di Milano, 20133 Milano, Italy

Prof. Zsolt Podolyak
Department of Physics, University of Surrey, Guildford GU2 7XH, United Kingdom

Prof. Gianluca Imbriani
Dipartimento di Fisica Università di Napoli Federico II, Napoli, Italy

Final examination:

17^{th} February 2023

Università degli Studi di Milano, Dipartimento di Fisica, 20133 Milano, Italy

Cover illustration: Marta Polettini

Internal illustrations: Marta Polettini

Design: Marta Polettini

MIUR subjects:
FIS/04 – Fisica Nucleare e Subnucleare

PACS:
23.40.-s, 29.30.Kv

Contents

List of Figures

List of Tables

Preface

I started my PhD in nuclear structure in October 2019 and I have been involved in the DESPEC collaboration since then. In particular, the PhD research project was focused on the investigation of the structure of heavy neutron-rich 220<A<230 Po-Fr nuclei exploiting beta decay.

The experimental activities of the DESPEC collaboration take place at the GSI-FAIR facility (Darmstadt, Germany), where I have been a visiting student during my master thesis (three months) and my PhD (about one year). There, working with the local Nuclear Spectroscopy group lead by J. Gerl and M. Gorska, I have been deeply involved in the preparation and commissioning of the DESPEC setup. This was the first time this setup has been used for beam measurements.

Since 2019, I have participated in the preparation of the experimental campaigns, being involved in the construction of the setup and development of the analysis procedure. During my stay I have worked on the characterization and readout implementation of several detector systems, such as plastic scintillators, $LaBr_3$(Ce) and HPGe detectors. I have had a role in the development of the analysis code and implementation and in data analysis of all experiments.

The main experiment my PhD project was focused on, referred to as *Dataset1* in this thesis, was initially scheduled in spring 2020 but was postponed to 2021 due to the Covid19 outbreak.

During 2020 and 2021 I have worked on the LISE++ simulations of FRS for our experiment, to optimise the transport of ions of interest to the decay station. I have worked on the implementation of the code for ion-β -γ correlations analysis. Another project I have focussed on during my stay at GSI was the development and testing of a digital front-end electronics coupled to $LaBr_3$(Ce) detectors, which resulted in a publication. This readout was tested for the first time and is now regularly used in the DESPEC and other collaborations.

In spring 2021 I participated not only in the *Dataset1* experiment, but in the full campaign (3 experiments in a 3-month period) having a key role in the data taking of all of them and helping in validating the experimental conditions.

After the campaign, I worked full time on the data analysis of the two experiments (*Dataset1* and *Dataset2*). In the first months I have worked on the FRS analysis, pre-analysis, calibrations and optimisation of the ions identification for both datasets. Afterwards, I have focused on the ion-β -γ correlations analysis. This proved to be very challenging in both experiments. At present, the main outcome of the analysis of *Dataset1* was the measurement of β -decay half-lives, confirming previous measurements in ^{227,229}Rn and providing a first measurement in ^{220,223}Po and ^{225,226}At. In *Dataset2*, thanks the higher

ion implantation rates, the additional result of the beta-delayed spectroscopic information in ^{100,101,102}Cd was achieved.

At present, I continue to be involved in the HISPEC-DESPEC experimental activity at GSI and in data analysis and interpretation of the results. I have helped in the data-taking in the experimental campaign in 2022, and I continue to work on the data analysis in both *Dataset1* and *Dataset2*. I have been attending and presenting my scientific work at regular meetings and workshops of the DESPEC collaboration at GSI.

Besides the experimental work at GSI, I have participated in several experiments in various international facilities: IFIN-HH laboratory, Bucharest (Romania), Argonne National Laboratories (US), LNL-Legnaro (Italy). In particular, since 2021, I have been involved in the experimental campaigns exploiting the AGATA detector at LNL.

During my PhD I have developed experience working on gamma-rays and charge particles detectors and magnetic spectrometers for heavy-ion beams. I have carried out analyses with many different experimental techniques, acquiring expertise in gamma-ray spectroscopy and fast-timing techniques.

The preliminary results of the research project and on-going analysis were presented at summer schools and conferences, where some of the contributions were awarded with the following prizes:

- presentation selected between the best talks in the 106^{th} National Conference of the Italian Physics Society (SIF) in 2020,
- presentation selected between the best talks in the 107^{th} National Conference of the Italian Physics Society (SIF) in 2021,
- student talk distinction in the Joint EPS-SIF International School on Energy 2021,
- 3^{rd} place poster prize in the Euroschool of exotic beams 2021.

I have presented the final results of my PhD project at several national and international conferences, such as the Zakopane Conference on Nuclear Physics, the International Nuclear Physics Conference and the 108^{th} National Conference of the Italian Physics Society. These presentations have resulted in the publication of conference proceedings.

Introduction

Motivation

Beta decay is the most common form of radioactive decay, occurring in isotopes of all known elements along the nuclear chart. This makes it a formidable tool to probe the internal structure of the nuclei both on the proton- and neutron-rich exotic nuclei, at the limit of the existence of the nucleus.

In this thesis work, two regions of the nuclear chart were addressed, the heavy neutron-rich region around mass A$\simeq 225$ and the proton-rich ^{100}Sn region.

The very exotic neutron-rich region of heavy Po-Fr nuclei is an interesting experimental playground as the β decay half-lives and spectroscopic information of daughter nuclei are presently unknown, due to the difficulties in populating them in most facilities around the world. Information on β decay for nuclei beyond N=126 is particularly useful to test the predictions of global nuclear models in exotic nuclei, which are used to describe the r-process of explosive nucleosynthesis in which, together with the s-process, the heaviest chemical elements (A>56) are created.

The long chain of proton-rich Sn isotopes has been the subject of a multitude of experimental and theoretical studies, with the aim to assess the robustness of the N=50 and Z=50 double shell closure. It is a great testing ground for nuclear models studying the evolution of shell structure and the interplay between pairing and quadrupole correlations. A transition from superfluid nuclei to spherical nuclei at mid-shell is also expected approaching the neutron shell closures at N = 50, where the seniority scheme can be adopted to describe the energy spectra and transition strengths.

In order to attack these very exotic regions, two experiments were performed at GSI-FAIR laboratory (Darmstadt, Germany) in spring 2021 using the HISPEC-DESPEC setup. The first experiment, hereafter referred as *Dataset1*, aimed at studying of the structure of 220<A<230 Po-Fr nuclei, with the goal of extending the systematics of the lowest-lying states and provide a measurement of β -decay half-lives of nuclei in this region. The second experiment, referred to as *Dataset2*, was focused on the p-rich ^{100}Sn region, with the aim of studying core-breaking effects with the aim of extending the knowledge on the $B(M1)$ systematics in odd-A tin isotopes and on the $B(E2)$ trend in even-even tin isotopes.

An introduction on atomic nuclei and on the production of exotic nuclei using fragmentation reactions is outlined in the first chapter, together with a description of β decay and of the r-process nucleosynthesis mechanism. The experimental setup, comprising the FRS magnetic spectrometer and the DESPEC decay station were described in detail in the second chapter. The third chapter reports on the first phase of the analysis performed on

the data, consisting of the calibration of the signals recorded from each detector system. The analysis techniques applied to obtain a proper identification of the implanted ions, as well as the logic of the ion-β -γ correlation algorithm, are thoroughly described in the fourth chapter. The experimental results and their interpretation are reported in the final chapter, together with a comparison with theoretical models.

Recent results on the two experiments are reported on in this work. In *Dataset1*, a systematic study of β -decay half-lives was performed, confirming previously obtained values in ^{227,229}Rn and providing a first measurement in ^{220,223}Po and ^{225,226}At. The measured half-lives were compared to theoretical models predictions. In *Dataset2*, the existing knowledge in the β -delayed decay pattern in ^{100,101,102}Cd was extended. Results on ^{101}Cd were compared with *ad-hoc* shell model calculations, highlighting a scheme of allowed β -decay. In ^{100,102}Cd, the levels' β feeding probabilities hint at a possible low lying state in the In mother nuclei, as the systematics for higher-mass indium isotopes suggests.

Thesis overview

This thesis is organised as follows:

- **Chapter 1**: physics motivation and theoretical introduction,
- **Chapter 2**: experimental setup used for the experiments,
- **Chapter 3**: pre-analysis techniques performed on the data,
- **Chapter 4**: analysis tools for ion identification and ion-β -γ correlations,
- **Chapter 5**: presentation of the results and comparison to theoretical models.

CHAPTER 1

Beta decay in neutron-rich and proton-rich exotic nuclei

In the first chapter, an introduction on atomic nuclei and on the production of exotic nuclei using fragmentation reactions is outlined, together with a description of β decay and of the r-process nucleosynthesis mechanism.

1.1 Exotic nuclei

Nuclei are self-bound systems of protons and neutrons kept together by the strong nuclear force [1–4]. All the known nuclear species are listed together in the Segré chart of nuclei, shown in Fig. 1.1, where the x and y axes are the number of neutrons (N) and protons (Z), respectively.

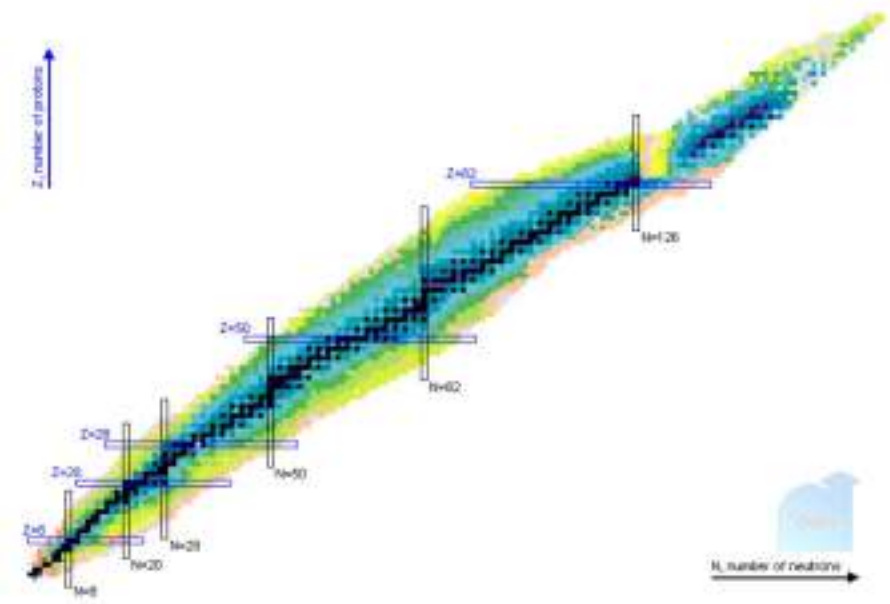

Figure 1.1: Segré chart of nuclides, from the nndc website (https://www.nndc.bnl.gov).

Stable nuclei are represented with black blocks and account for only 284 of the thousands nuclei known at present. Stable isotopes lie on the diagonal N=Z for low Z nuclei, up to Fe, while the heavier ones have a larger content in neutrons. The vast majority of nuclei shows an imbalance between the number of protons and neutrons. Of all bound

nuclei, only ~ 3300 are known at present while approximately 5000 are yet to be discovered [5, 6]. It is possible to add or remove nucleons until a certain limit, beyond which the nucleus becomes unbound. These limits are called *driplines*. The proton dripline has already been reached experimentally, while the neutron dripline has been reached only for the light Z nuclei and is yet to be firmly established for the majority of isotopes.

Of the thousands nuclei studied so far, the largest fraction is radioactive, β decay being the most common decay mode. The availability of highly-energetic intense beams and powerful experimental arrays has allowed, in recent years, to access nuclei characterised by an unbalanced number of neutrons or protons, the so-called *exotic nuclei*, which are defined as neutron-rich (n-rich) if $N \gg Z$ or proton-rich (p-rich) in the opposite case.

The atomic nucleus is one of the building blocks of nature. Therefore, understanding how protons and neutrons are bound together, what is the exact form of their interaction, and how nuclei change their structure as a function of isospin are main questions for fundamental physics. The details of the nuclear structure have an impact in other fields of physics, too. As an example, they are crucial for the understanding of stellar nucleosynthesis and astrophysical phenomena such as the Supernovae or the X-ray Bursts. Another example is provided by the determination of neutrino mass from the β β decays, which relies on precise theoretical calculations of nuclear matrix elements.

1.2 The shell structure of nuclei

The atomic nucleus is a many-body quantum system composed of strongly interacting fermions (protons and neutrons). The force that keeps the nucleus bound is called *nuclear force*. It acts between two nucleons of any type and is short-ranged and attractive, able to overcome to the repulsive Coulomb force acting between protons. The nuclear force has its origin in the exchange of massive mesons between the nucleons, in contrast to the massless photon that mediates the Coulomb interaction.

Being a many-body system, the atomic nucleus should be treated with similar techniques presently used to study condensed-matter physics, but there are fundamental differences, which make the nucleus a much more difficult system to study.

First of all, the nucleus is composed by two different fermions, which display their own internal structure. This results in a much more complicated interaction than the electromagnetic force, with three- and many-body terms playing an important role. Moreover, the energy gap between collective motion and single-particle excitations is small, resulting in an overlap between different energy scales, which complicates the mathematical treating of such systems. Therefore, the nucleus displays, similarly to electrons in atoms, a shell structure behavior. The main difference is that electrons are subject to an external field, due to the attraction of the nucleus, while nuclei are self-bound systems and the shell structure is the consequence of an average potential generated by the nucleons themselves.

1.2.1 The nuclear hamiltonian and the n-n interaction

The general nuclear hamiltonian can be written as:

$$H = \sum_{i=1}^{A} T_i + \sum_{i,j}^{A} V_{ij}, \tag{1.1}$$

where A is the total number of nucleons, T_i is the kinetic energy of the single nucleons and V_{ij} is the two-body interaction potential. It is possible to assume the presence of a

single-particle potential V_i, so that:

$$H = \sum_{i=1}^{A} T_i + \sum_{i=1}^{A} V_i + \sum_{i,j}^{A} V_{ij} - \sum_{i=1}^{A} V_i = \sum_{i=1}^{A} H_i^{s.p.} + \sum_{i,j}^{A} H_{i,j}^{res}, \tag{1.2}$$

where $H_i^{s.p.} = \sum_{i=1}^{A} T_i + \sum_{i=1}^{A} V_i$ is the single-particle Hamiltonian and $H_{i,j}^{res} = \sum_{i,j}^{A} V_{ij} - \sum_{i=1}^{A} V_i$ is the residual interaction given by the fraction of the two-body interaction which is not absorbed by the single-particle potential.
The eigenstates of $H^{s.p.}$ can reproduce the observed shell effects in a first approximation with the use of the harmonic oscillator potential V_c, allowing for an analytical solution for the Schrödinger equation. In this approximation, the Hamiltonian for a given nucleon is:

$$H_i^{s.p.} = \frac{1}{2} M_i v_i^2 + \frac{1}{2} M_i \omega^2 r_i^2, \tag{1.3}$$

where M_i, v_i are the mass and the velocity of the nucleon, respectively, r_i is its radial distance from the centre of the nucleus and ω a dimension parameter. The correspondent eigenfunctions are:

$$\Psi_{n,l,m_l,s,m_s}(r,\theta,\phi) = R_{n,l}(r) Y_l^{m,l}(\theta,\phi) \chi_{1/2}^{m_s}, \tag{1.4}$$

where l and s are the orbital angular momentum and spin quantum numbers, $m - l$ and m_s are their projections on the polar axis and n an integer quantum number. r, θ and ϕ are the polar coordinates used to define the position. $Y_l^{m,l}(\theta,\phi)$ are the spherical harmonics and $\chi_{1/2}^{m_s}$ the spin wave functions. The radial part of the eigenfunctions is represented by:

$$R_{n,l}(r) = \left[\frac{2^{l-n+2}(2l+2n+1)!!\alpha^{2l+3}}{\sqrt{\pi} n![(2l+1)!!]^2} \right]^{1/2} e^{-1/2\alpha^2 r^2} r^l \sum_{k=0}^{n} \frac{(-1)^k 2^k n!(2l+1)!!(\alpha^2 r^2)^k}{k!(n-k)!(2l+2k+1)!!}, \tag{1.5}$$

where $\alpha^2 = \frac{M\omega}{\hbar}$ and $(2n+1)!! = (2n+1)(2n-1)(2n-3)...1$. The eigenvalues of this Hamiltonian are:

$$E_{n,l} = \left(2n + l + \frac{3}{2}\right)\hbar\omega = \left(N + \frac{3}{2}\right) \quad N = 2n + l. \tag{1.6}$$

Since $E_{n,l}$ is not a function of s, m_l and m_s, the energy level degeneration for both protons and neutrons is $2(2l+1)$. The occurrence of magic numbers connected to the shell closures can be seen in a number of effects in the nuclear landscape. The harmonic oscillator potential is able to justify only the first observed magic numbers (2, 8, 20), corresponding to shell-closure. In order to reproduce higher magic numbers (28, 50, 82, 126), a modification of such potential is needed, with the inclusion of a spin-orbit coupling term. The spin-orbit interaction can be expressed as:

$$V_{so} = V_{ls} \cdot \frac{\partial V_c}{\partial r} \cdot \vec{l} \cdot \vec{s}, \tag{1.7}$$

where V_{ls} is a phenomenological constant. The addition of this interaction provides a further splitting between levels with same l but different total angular momentum $\vec{j} = \vec{l} + \vec{s}$, as $j = l \pm 1/2$. As a consequence, the separation between two levels is proportional to $(2l+1)$ and m_l and m_s are no longer good quantum numbers. The

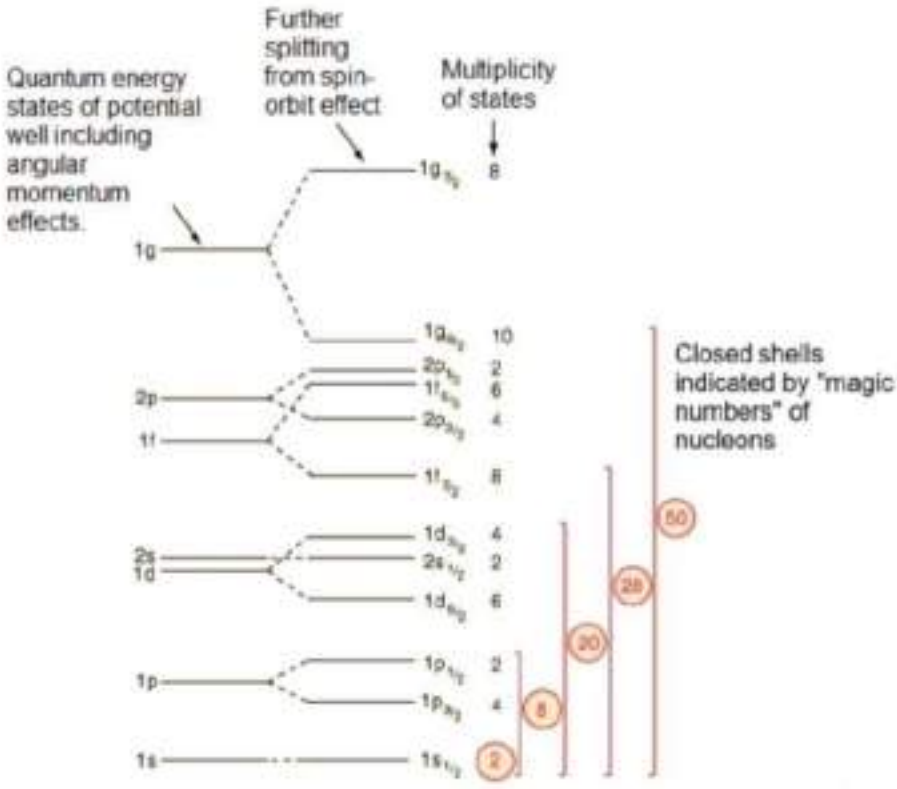

Figure 1.2: A picture of the shell model levels. The levels on the left are given by the Woods-Saxon potential, while the ones on the right are obtained by the Woods-Saxon potential plus a spin-orbit term (adapted from[2]).

addition of the spin-orbit term to a Wood-Saxon potential makes it possible reproduce correctly all magic numbers (Fig. 1.2).

When many nucleons are outside a shell, correlations and interactions between nucleons are to be considered and H^{res} is not negligible anymore. In order to keep the problem computationally treatable, one needs to switch from a full Hilbert space to a restricted space, where effective interactions between single-particles configurations determine the behavior of the system, provided that all expectation values in the full space are equal to the ones obtained in the restricted space. As a result, the shell-model orbits are grouped into an inert core composed of the full single-particle orbits, a valence space in which the orbits are partially populated by nucleons and an external space comprising the remaining empty orbits [7].

1.2.2 The seniority scheme

The seniority scheme is based on the evidence that nuclear forces energetically favour the coupling of two identical nucleons to a total angular momentum $J = 0$ in a shell over all other possible coupling. This combination guarantees the maximum spatial overlap between the two-nucleon densities, provided that the two angular momentum projections point in opposite directions, neglecting spin. As a result, the first excited state in an even-even nucleus can be obtained only by breaking the spin alignment of two nucleons to zero. In an odd nucleus, instead, the excitation is achieved by placing the odd nucleon in a low energy level.
In this framework, one can define *seniority* as the number ν of unpaired nucleons, which is a good quantum number for semi-magic nuclei at first approximation. In such nuclei, the number n of neutrons or protons outside the doubly-magic core will mainly have a j^n configuration, where j is the lowest energy orbital outside the core. In a j^n configuration, the conservation of the seniority quantum number allows a simplified description of the nuclear structure, called seniority scheme. The seniority scheme predicts that the energies of low-spin excited energy levels will be independent on the number of nucleons outside the core. It also provides an analytical estimate of the electromagnetic transition strengths between these states, for which a parabolic behaviour with respect to the number of paired particles, peaking at mid shell, is expected.
The lowest energy states in a j^n configurations are generally the ones displaying the lowest seniority, as breaking a pair of nucleons coupled to angular momentum zero has an energetic cost (*pairing energy*). Therefore, the ground state of even-even semi-magic nuclei has $\nu = 0$, while the lowest levels with $J = 2, 4, 6, ...$ will have most probably $\nu = 2$, i.e. only one broken pair of nucleons. Moreover, in a j^n configuration, due to the Pauli exclusion principle, not all angular momentum couplings of two identical nucleons are possible. The maximum angular momentum that can be created is given by:

$$J^{max} = nj - \frac{n(n-1)}{2}. \tag{1.8}$$

The ^{100}Sn region is an ideal area to test the seniority symmetry, as the seniority scheme is established, in these nuclei, for a configuration of n protons with $j = 9/2$ in the $g_{9/2}$ orbit. Deviations from this scheme have their origin in the mixing with close-by orbitals and by effect of core-excitations across the gap.

1.3 Fragmentation and fission reactions

Neutron-rich nuclei can be produced by several physical processes such as fusion, quasi-elastic or deep inelastic transfer of nucleons, fragmentation, and fission. While fission is suitable to produce medium-mass nuclei on the neutron-rich side of the nuclide chart, fragmentation allows a broader access to all the chart, on the two opposite sides, and is particularly effective for the population of heavy systems. In general, the cross section of fragmentation reactions is large, allowing one to produce a wide range of radioactive beams far from stability with large intensities. Moreover, fragments are emitted in forward direction into a small cone due to the kinematic focussing at high energies. Fission reactions, instead, can be used as an additional production reaction allowing for large reaction cross sections for medium-heavy neutron-rich isotopes. However, in-flight fission causes a larger spread in angle and momentum, as compared to fragmentation [8]. When a highly-energetic heavy ion beam penetrates a target, the projectile and target both can undergo fragmentation. This process consists of two steps, which occur on different time scales: the abrasion and the ablation [9], a schematic of which is given in Fig. 1.3. The use of a heavy ion beam on a light target ensures that a large amount of energy is transferred to the reaction products, needed for their transport and selection.

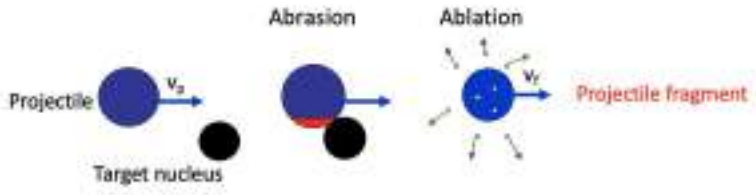

Figure 1.3: Schematic of the projectile fragmentation reaction. It consists of a two-stage process, where nucleons are abraded (Abrasion) and the pre-fragment emits nucleons (Ablation).

In the abrasion step, being the beam relativistic ($\beta \sim 0.8$), the interaction between the nucleons of the beam and the target lasts $\simeq 10^{-23}$ s, while the average nucleon motion is $\simeq 0.1$ fm. Therefore the nucleons can be considered static during the process and can be described with Glauber-type models. Within this approximation, only the nucleons belonging to the geometrically overlapping region are considered *participants* to the reaction, while the nucleons outside the region are *spectators* and continue to travel gaining an excitation energy that is, in first approximation, proportional to the number of abraded nucleons [10]. The relative proportion of spectators and participants depends on the impact parameter, while the average excitation energy of the spectator nucleons is mainly determined by the particle-hole excitations of the nucleons removed by the abrasion.
In the ablation step, the spectator nucleons, which may be excited to levels above the separation threshold, de-excite by an evaporation of neutrons, protons, light particles or fissioning. In the latter case, the two fission fragments are emitted in a narrow forward cone with respect to the beam axis. This process can be described by a statistical model where thermal pre-equilibrium in the excited pre-ablasion fragment is assumed. The characteristic time scale for the emission of particles varies between $\sim 10^{-16}$ s for an excitation energy of 10 MeV and $\sim 10^{-21}$ s at 200 MeV. After the ablation, the fragment will de-excite with the emission of γ rays and high-spin levels can be populated.

A large number of different ion species can be produced with a given beam-target

combination. For example, the ^{238}U fragmentation calculated cross-section for elements with Z= $70 - 92$ are given in Fig. 1.4 [11].

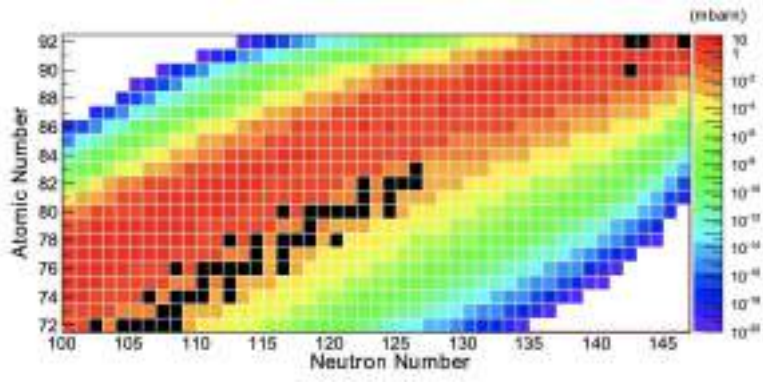

Figure 1.4: Calculated production cross-sections from [11] for projectile fragments from a ^{238}U beam on a ^{9}Be target at 1000 MeV/u (adapted from [12]). Stable nuclei are marked by black boxes.

The reaction products from in-flight fission of ^{238}U, instead, are in the mass ranges of A$\simeq$ $72 - 118$ and A$\simeq$ $120 - 166$, and in atomic number ranges of Z$\simeq$ $28 - 44$ and Z$\simeq$ $50 - 62$.

1.4 Beta decay

One of the earliest observed radioactive phenomena was the emission of electrons. The inverse process of the capture by a nucleus of an electron from its atomic orbital and the process of positive electron (positron) emission were observed much later, in the 1930s. These three nuclear processes are grouped under the common name of *beta (β) decay*, which is the most common form of radioactive disintegration, happening in isotopes of all known elements except for the super-heavy ones [1].

In basic terms, β decay consists in the conversion of a proton into a neutron, or of a neutron into a proton, accompanied by the emission of a neutrino or antineutrino. In an atomic nucleus, this results in a change of both Z and N by one unit: Z $\rightarrow$ Z $\pm$1, N $\rightarrow$ N $\mp$1, while A = Z + N remains constant. As a result, β decay represents a convenient way for an unstable nucleus to reach a stable isobar.

As there are evidences against the presence of electrons as constituents of atomic nuclei, the β decay process can be regarded as the creation of an electron from the available decay energy. The electron is produced in the instant of the decay and is immediately ejected from the nucleus. This happens in contrast with α decay, where the ^{4}He nucleus previously exists inside the nucleus. Moreover, while α particles are emitted with sharp and well defined energies, β decay has the peculiar characteristic of having a continuous energy distribution, from zero up to an upper limit, equals to the energy difference between the initial and final states (Fig. 1.5). In order to explain this behavior, in 1931, Pauli proposed the emittance of a third particle, called *neutrino*. Neutrinos carry the remaining energy of the decay and cannot be detected by a calorimeter, due to their high penetration power. The conservation of electric charge requires the neutrino to be electrically neutral, while the angular momentum conservation and statistical considerations in the decay process require the neutrino to have a spin equal to the one of

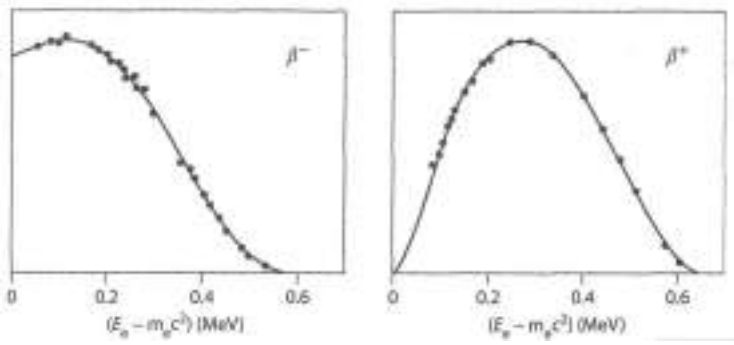

Figure 1.5: Electron (left) and positron (right) energy distribution in ^{64}Cu decay, adapted from Ref. [1]. The low energy part of the electron spectrum is enhanced due to the deceleration caused by the nuclear attraction. The opposite is visible in the positron energy spectrum.

the electron $(1/2)$. Two different kinds of neutrinos can be emitted in β decay: a *neutrino* (ν) in positron emission and an *antineutrino* ($\bar{\nu}$) in the electron emission [2].

To summarise, the three basic β decay processes are:

- $n \rightarrow p + e^- + \bar{\nu}$ negative beta decay (β^-);
- $p \rightarrow n + e^+ + \nu$ positive beta decay (β^+);
- $p + e^- \rightarrow n + \nu$ orbital electron capture (ϵ).

The so-called *weak interaction* is responsible for the transmutation of a neutron into a proton, with the emission of an electron and an antineutrino or of a proton into a neutron with the emission of a positron and a neutrino.

1.4.1 Beta-decay *Q-value*

Every decay process corresponds to the transformation of an unstable nucleus ($parent\ nucleus$) from state of energy ϵ_2 into a more stable configuration ($daughter\ nucleus$) at a state of energy ϵ_1, releasing a well-defined quantity of energy $\epsilon = \epsilon_2 - \epsilon_1$.

The energy available for a decay process is called Q-$value$ and is defined by the atomic mass difference between the initial and final decay products:

$$Q = M_{initial} - M_{final} \tag{1.9}$$

As the decay of a nucleus can usually occur via many competing processes, one can define a $branching\ ratio$, which stands for the probability of each decay path [13].

In the case of β -decay, one can express the Q-value in the form:

$$\begin{aligned} Q_{\beta^-} &= (M_{Z,A} - M_{Z+1,A})c^2 \\ Q_{\beta^+} &= (M_{Z,A} - M_{Z-1,A} - 2m_e)c^2 \end{aligned} \tag{1.10}$$

Eq. 1.10 shows that β^- decay occur whenever the atomic mass of the parent nucleus is larger than that of the daughter nucleus, while for β^+ decay an additional term of two electric masses is present. In both cases the Q value is shared in the form of kinetic energy of the electron (positron), the antineutrino (neutrino) and the energy of the residual recoiling nucleus, which accounts for a very small fraction.

1.4.2 The Fermi theory of β decay

β decay shows some differences from α decay, which is why a new approach was needed for its description. In particular,

- the electron and neutrino do not exists inside the nucleus before the decay happens,
- the electron and neutrino are to be treated relativistically,
- the continuous distribution of electron energies must result from the calculation.

A theory to describe β decay was suggested by Fermi in 1934, on the basis of Pauli's neutrino hypothesis. Although this theory does not permit parity violation, it describes the continuous energy distribution in β decay and gives a qualitative understanding of the values of the decay half-lives. The Fermi theory is based on the assumption that the transition probability for β decay is weak, as compared with the interaction that forms quasi-stationary states, and its characteristic times (half-lives of the order of seconds or longer) are far longer than the characteristic nuclear time (10^{-20} s). The theory is based on an analogy of β decay with the emission of electromagnetic radiation, induced by a time-dependent interaction between the system that irradiates and the electromagnetic field. In the case of β -decay, the decay-causing interaction is the weak force, which can be treated as a weak perturbation, i.e. it is small compared to the forces responsible for maintaining the initial and final quasi-stationary states. This is expressed with the *Fermi's Golden Rule*:

$$\lambda = \frac{2\pi}{\hbar}|\mathcal{M}_{if}|^2 \frac{dN}{dE_T}, \tag{1.11}$$

Here,

$$\mathcal{M}_{if} = \int \psi_f^* \mathcal{V} \psi_i d^3r \tag{1.12}$$

is the matrix element corresponding to the weak interaction $\mathcal{V}$ between the initial and final quasi-stationary states of the system and the factor $\frac{dN}{dE_T}$ is the density of available final states with disintegration energy dE_T.
The final state wave function ψ_f must include both the nucleus, electron and neutrino:

$$\psi_f = \psi_R \phi_e \phi_\nu. \tag{1.13}$$

ϕ_e and ϕ_ν are free particle wave functions and have an expression of plane wave type. Taking into account the fact that the wavelengths associated with leptons are very large as compared to the nuclear dimensions, in the proximity of the nucleus the product of ϕ_e and ϕ_ν is constant and equal to $1/V$. For the solution of the integral in Eq. 1.12, it is necessary to know the form $\mathcal{V}$ of the weak interaction. If one does not take into account the spins of the particles involved, the matrix element constructed from the interaction v has a simple nonrelativistic expression:

$$\mathcal{M}_{if}^F = g_F M_{if}^F, \tag{1.14}$$

where

$$|M_{if}^F|^2 = \sum_{m_f} \left| \int \psi_f^* \left(\sum_k t_\pm^k \right) \psi_i d^3r \right|^2. \tag{1.15}$$

Here, g_F is the coupling constant for Fermi transitions and the matrix element M_{if}^F is dimensionless. The operators $t_\pm = t_x \pm i t_y$, constructed from isospin operators, transform

a neutron into a proton in β^- decay and a proton into a neutron in β^+ decay. The density $\frac{dN}{dE_T}$, where $E_T = E_e + E_\nu$, and, with fixed E_e, $dE_T = dE_\nu$, can be written as:

$$\frac{dN}{dE_T} = \frac{dN_\nu}{dE_\nu} = \frac{V}{2\pi^2(\hbar c)^3}(E_T - E_e)^2. \tag{1.16}$$

A correction factor, referred to as the *Fermi function* $F(Z, E_e)$, is added to take into account nuclear Coulomb field effects over the electron wavefunction, which in reality cannot be represented by a plane wave. The Fermi function is expressed as:

$$F(Z, E_e) = \frac{2\pi\eta}{1 - e^{-2\pi\eta}}, \tag{1.17}$$

where $\eta = \pm Ze^2/\hbar\nu_e$ for electron ($-$) and positron ($+$).
With all the adjustments considered, Fermi's Golden Rule takes the form:

$$\lambda(E) = \frac{F(Z, E_e)}{V\pi\hbar^4c^3}|\mathcal{M}_{if}|^2(E_T - E)^2, \tag{1.18}$$

where $\lambda(E)$ refers to one energy E of the emitted electron.
One can also write the probability per unit time of an electron emission with energy between E and $E + dE$:

$$\lambda(E)dN = \frac{F(Z, E)|\mathcal{M}_{if}|^2}{2\pi^3\hbar^7c^6}E(E^2 - m^2c^4)^{1/2}(E_T - E)^2dE, \tag{1.19}$$

explaining the behaviour of the energy spectra shown in Fig. 1.5.

1.4.3 Beta decay selection rules

Beta decay leads an initial (mother) nucleus of spin I_i to a final (daughter) nucleus of spin I_f, with angular momentum and parity conservation. To establish selection rules for I_i, I_f and the parities of the initial and final states, one has to consider allowed and forbidden decays separately.

Allowed decays

In the allowed approximation, the electron and neutrino wave functions are given by their value at the origin, and therefore do not carry any orbital angular momentum ($l = 0$). Therefore, the only change in angular momentum results from the sums of the spins of the electron and neutrino ($s = 1/2$).
If the spins are antiparallel ($S = 0$), no change in the nuclear spin is possible: $I_i = I_f$. These are known as *Fermi* transitions. If, instead, the electron and neutrino spins are parallel ($S = 1$), then $I_i = I_f + 1$, which is possible only if $\Delta I = 0, 1$, except for the case where $I_i = I_f = 0$. Such transitions are known as *Gamow-Teller* (GT) transitions.
As in allowed β decay $l = 0$, and the parity associated is $(-1)^l$, the parities of the initial and final states must be identical.

Forbidden decays

Forbidden decays are less probable than allowed decays and display generally longer half-lives, but they are the only ones that can occur if the allowed matrix elements vanish. If the initial and final states in the mother and daughter nuclei have opposite parities,

the selection rule for allowed decay is violated. For the parity to change, the electron and neutrino must have an odd value of the orbital momentum relative to the nucleus. Therefore, $l = 1$ decays are called *first-forbidden* (FF) decays, and they can be of Fermi-type ($S = 0$) or Gamow-Teller-type ($S = 1$). In the former case, the coupling of $S = 0$ with $l = 1$ gives a total angular momentum of one unit carried by the β decay, so that $\Delta I = 0$. Coupling $S = 1$ with $l = 1$, instead, gives 0, 1 or 2 units of total angular momentum, i.e. $\Delta I = 0, 1, 2$.
Beta decays with $\Delta I \geq 2$ and no change of parity are known instead as *second-forbidden* decays.

To summarise, the selection rules for β decay are given in Tab. 1.1.

Transition	$\Delta I = I_i - I_f$	Parity change
Allowed	$0, \pm 1$	No
First forbidden	$0, \pm 1, \pm 2$	Yes
Second forbidden	$\pm 2, \pm 3$	No
...	...	...
nth forbidden	$\pm n, \pm(n+1)$	$(-1)^n$

Table 1.1: Selection rules for angular momentum and parity in β decay.

1.4.4 The total decay rate and Logft value

The total decay rate for β decay can be written in the form:

$$\lambda = \frac{m^5 g^2 c^4 |M_{if}^F|^2}{2\pi^3 \hbar^7} f(Z, E_T). \tag{1.20}$$

The constant factors and the dependence on the electron enegy can be grouped into a factor known as the *Fermi integral*:

$$f(Z, E_T) = \frac{1}{m^5 c^{10}} \int_0^{E_T} F(Z, E) E (E^2 - m^2 c^4)^{1/2} (E_T - E)^2 dE, \tag{1.21}$$

which is dimensionless and usually presented in curves which are function of the atomic number Z and of the electron maximum energy E_T.
If one converts the decay rate into the half-life $T_{1/2}$, one obtains a quantity called *comparative half-life*:

$$fT_{1/2} = ln(2) \frac{2\pi^3 \hbar^7}{g^2 m_e^5 c^4 |M_{if}^F|^2} \tag{1.22}$$

by using the relation $\lambda = \frac{ln(2)}{T_{1/2}}$. This quantity gives a measure of changes in the nuclear matrix elements M_{if}^F, and therefore in the nuclear wave functions. For example, transitions in which the value of M_{if}^F is near unity are associated to the lowest ft values and are called *superallowed*. As β -decay ft values are subject to large variations, ranging between 10^3 and 10^{20} s, a preferred quantity used to classify the decay is the $log_{10}(ft)$, generally called logft. Most allowed decays have logft values in the range 3.5 to 7.5, while first-forbidden decays range between 6 and 9. The experimental distribution of logft values is shown in Fig. 1.6.

The use of $\log ft$ allows a separation of the transitions that one measures by their degree of forbiddenness, permitting, for example, to assign the spin and parity of the final state, if the initial one is know.

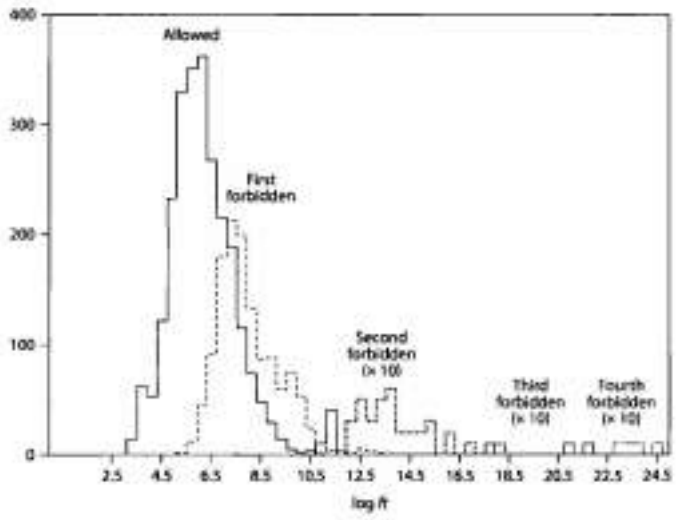

Figure 1.6: Systematics of experimentally measured $\log ft$ values (adapted from Ref. [1].

1.4.5 Beta-delayed neutron or proton emission

When excited states of a nucleus are populated via β decay, γ decay is not the only form of transition that it can use to reach stability. In specific cases, the states can be unstable against the emission of one or more nucleons. Being the nucleon emission fast (competing with γ emission), it occurs with a half-life characteristic of β decay.
The β -decaying parent (or *precursor*) decays towards the daughter nucleus, also called *emitter*. As the Q_β window gets large, part of the precursor nuclei does not end in low-lying states of the daughter nucleus, but feeds unbound states, which primarily decay by nucleon emission.
In the case of neutron-rich nuclei, for example, β -delayed neutron emission process is energetically permitted when the β -decay energy is greater than the neutron separation energy $Q_\beta > S_n$. In some cases the Q_β window is large enough that the emission of more than one neutron can occur. Being the decay a two-body process, the neutron emerges with an energy which corresponds to the energy difference between the initial and final states. Moreover, from the relative probability of nucleon emission by different states in the emitter, we can deduce the relative population of these states in the β decay of the precursor. This provides information on the β -decay matrix elements.

1.5 β-decay data as an input to r-process models

1.5.1 Introduction: overview on nucleosynthesis processes

The early universe represents the ultimate particle accelerator in which energies and densities of particles are beyond what we can achieve with artificially constructed acceler-

ators. By studying the end products, it is possible to understand many reaction processes that were responsible for their formation, as displayed in Fig. 1.7.

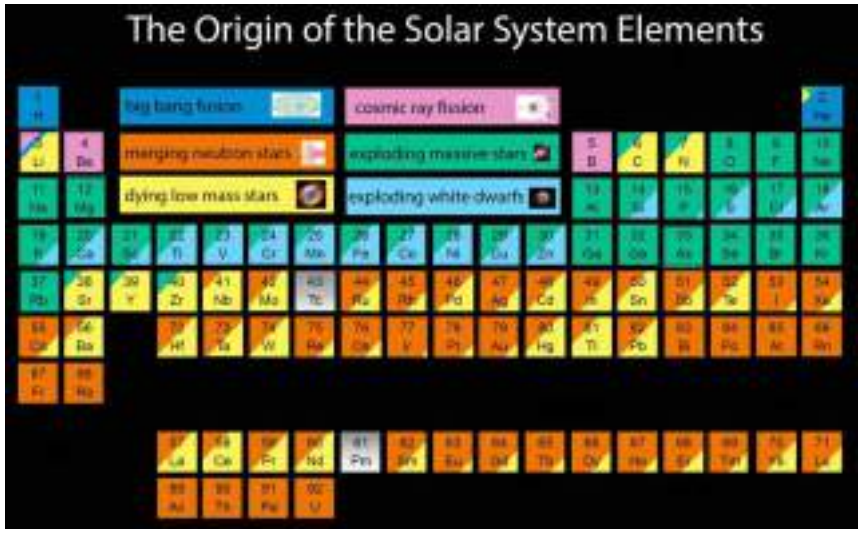

Figure 1.7: The periodic table of the chemical elements divided in groups based on their different astrophysical origin. Graphic created by Jennifer Johnson. Astronomical Image Credits: ESA/NASA/AASNova

The standard model of the hot Big Bang cosmology is based on an overall framework based on the General Theory of Relativity, nuclear and particle properties directly measured, inferences from the standard model of elementary particles and some extrapolations based on reasonable hypotheses. The observed relative amounts of light isotopes, which were formed in the earliest times of element formation, set constraints on the fundamental process that occurred in their formation epoch [2].

The understanding of the formation processes of the heavy elements is a much more difficult task, as the physics is more complicated, the reactions are more difficult to reproduce, and the mechanics and thermodynamics of the processes are less understood. The experimental evidences of these processes rely mainly on astrophysical observations not only with conventional optical telescopes, but, more recently, using particle and γ -ray spectrometers carried by orbiting spacecraft. Also nuclear decays and reactions observed in laboratories around the world can determine fundamental limits on the nature and, especially, the duration of nuclear reactions in stars [2].

An interaction between astrophysics and nuclear physics is necessary to understand the nucleosynthesis phenomena. To the nuclear physicist many phenomena in the Universe represent nuclear experiments on a grand scale, usually under conditions that cannot be reached in Earth-bound laboratories. To the astrophysicist, nuclear structure represents experimental and theoretical data inputs which are needed to describe possible astrophysical scenarios. Within this dichotomy, modeling the explosive nucleosynthesis of the rapid neutron-capture process (the *r process*) has represented a particularly fascinating challenge for the past six decades [14]. This process is responsible for about half of the abundances of heavy elements beyond Fe in our Solar System, as well as for the long-lived actinides like Th and U [15].

The processes that lead to the formation of the elements in our Solar System can be

understood via the study of the so-called universal or cosmic abundance curve, as shown in Figure 1.8 [16]. The relative abundance decreases exponentially from Hydrogen to Iron, and it decays with a small slope for $A > 100$. The abundance is very low for Li, Be, B, which are rare elements as compared to their neighbours H, He, C, N, O. Alpha particle nuclei such as ^{16}O, ^{20}Ne, ^{40}Ca, ^{48}Ti have high abundances, and there is a strongly marked peak corresponding to ^{56}Fe. In the $A > 100$ region, double peaks are present in correspondence with the magic numbers $N = 50,\ 82,\ 126$. Proton-rich heavy nuclei show instead a low abundance.

The bulk material from which the Solar System was formed 4.6 billion years ago is composed by many nucleosynthesis agents which have contributed to its composition over the 10 Gy that have elapsed between the formation of the Galaxy and the formation of the Solar System itself. The analysis of the Solar System composition is largely based on the analysis of a special class of rare meteorites, the CI1 carbonaceous chondrites, which are considered the least-altered samples of primitive solar matter available. Time-dependent 3D hydrodynamical atmosphere models were used successfully to explain the solar spectroscopic data for some elements up to iron.

The Solar System abundance distribution show a high *iron peak* centred around ^{56}Fe followed by a broad peak in the mass number $A \simeq 80 - 90$ region, with double peaks showing up at $A = 130 \sim 138$ and $195 \sim 208$. These peaks lie on top of a background which decreases rapidly with increasing A. These peaks provide a clear demonstration that a tight correlation exists between Solar System abundances and the neutron shell closures of atomic nuclei [17].

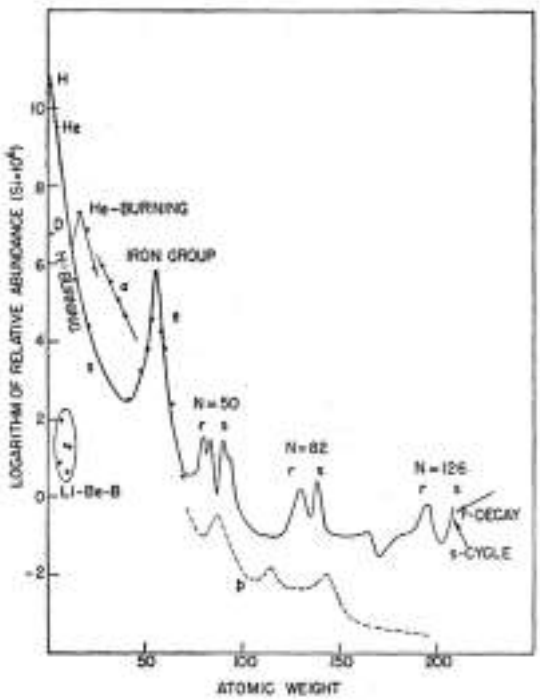

Figure 1.8: Schematic curve of atomic abundances as a function of the atomic weight, based on the data of Suess and Urey [18] (adapted from [16]).

The origin of heavy elements (A>100) has been one of the most important and long-standing issues in astrophysics. Since the 1950s it is known that the solar system abundances of nuclei heavier than iron can be divided in half based on the nucleosynthesis processes that are responsible for their production [14]. These heavy nuclei can be produced via slow neutron capture (s process), rapid neutron capture (r process) or proton capture (p process) as shown in Figure 1.9.

Several astrophysical results point to the existence of at least two different kinds of neutron capture nucleosynthesis, which also show a different kind of origin sites. Evidences of this are based on several observations from different fields, such as the study of extinct radionuclides in the early Solar System and isotope abundance anomalies found in presolar diamonds. The strongest evidence lies in the oservation of heavy neutron-capture element abundances in metal-poor halo stars and in the globular cluster M15[1] [20].

The so-called s process corresponds to the process of neutron capture with the emission of γ radiation (n, γ) over a long time-scale, from 100 years to 10^5 years. For this reason, this neutron capture process is known as *slow*, as it occurs at timescales as comparable to β decay timescales ($\tau_\beta < \tau_{n,\gamma}$) [21]. The s-process is responsible for the production of nuclei lying along the valley of stability, in particular in the range $23 \leq A \leq 46$ and $63 \leq A \leq 209$, producing abundance peaks at $A = 90$, 138 and 208 [16].

The r process is instead the process of neutron capture at a very short time scale ($\sim 0.01 - 10$ s) as compared to β decay ($\tau_{n,\gamma}, \tau_{\gamma,n} < \tau_\beta$). This mode of nucleosynthesis is responsible for the production of nuclei in the neutron-rich side in the range $70 \leq A \leq 209$ and of the synthesis of uranium and thorium. The r-process produces abundance peaks at $A = 80$, 130 and 194.

One additional mode of synthesis is needed to explain the production of proton-rich nuclei. The so-called p process concerns nuclei on the proton-rich side of the valley of stability, and corresponds to proton capture followed by the emission of γ radiation (p, γ) or the emission of a neutron following a γ -ray absorption (γ, n). The nuclei formed via this mode of nucleosynthesis show low abundances as compared to stable and neutron-rich isotopes.

1.5.2 The r process

Among the various nucleosynthesis processes, the rapid neutron capture process is believed to be one of the main synthesis mode of approximately half of the heavy elements present in nature. The r process can happen only if a sufficient neutron source is present to synthesise elements up to $A \sim 200$, therefore finding the astrophysical site of this mode of nucleosynthesis is a central issue of physics.

The r-process pattern can be deduced from the solar system abundances by subtracting the s-process and p-process contributions [22]. This creates a pattern which shows three main abundance peaks at $A \leq 80$, 130 and 195 associated with the $N = 50$, 82 and 126 shell closures [14].

While the basic mechanisms and astrophysical sites of s process and p process are well known, the astrophysical nature of the dominant site of the r process is still debated, although the physical requirements for the occurrence of r-process nucleosynthesis are well understood [21]. For this reason, this remains one of the greatest open problems in physics, and knowledge of nuclear physics properties are some critical inputs in the

[1] M15 is a globular cluster discovered in 1746 by Jean-Dominique Maraldi, and it is located in the constellation Pegasus, 33,600 light-years from Earth. M15 was the first globular cluster known to host a planetary nebula and it has also been found to host an intermediate-mass black hole at its center [19].

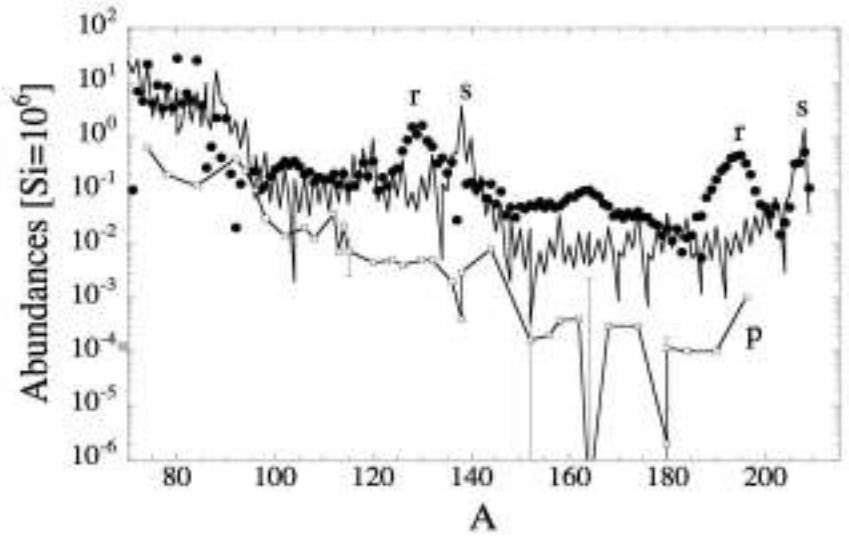

Figure 1.9: Solar abundances of heavy nuclides originated from s-process (solid line), r-process (dots) and p-process (squares) contributions. The uncertainties on the abundances of some p-nuclides that come from a possible s-process contamination are represented by vertical bars [17]

calculation of r-process nucleosynthesis [14]. Recent publications (Ref. [23]) point at neutron-star mergers as the preferred site for r-process, after its experimental observation in 2017. Nevertheless, an open question remains regarding the contribution of other astrophysical sites over the history of the galaxy to the current solar-system r-process abundances.

1.5.3 r process physical requirements

The synthesis of the heaviest r-process elements requires environments with such high neutron densities that neutron captures are faster than β decays, up to neutron-rich unstable nuclei $15 - 30$ units from stability. Starting from a seed distribution around $A = 50 - 80$ before r process develops, the operation of rapid neutron capture requires on the order of 10-150 neutrons per seed nucleons to form all heavier r-nuclei [22]. This observation points to two different modes of the rapid neutron capture process, which are the so-called *weak* and *main* r process, the former responsible for the synthesis of the light nuclei ($A < 120$) and the latter correspondent to the heavy ($A > 120$) ones. The pattern of the main r-process elements is similar among r-process enhanced halo stars and it is a match to the solar residuals [14].

Since early studies of the r process, nuclear masses and β -decay rates are known to be key ingredients in r-process abundance predictions. These models assume that the r process would proceed via rapid neutron captures on seed nuclei in a hot environment, establishing an equilibrium between neutron captures and photodissociations: $(n, \gamma) \rightleftharpoons (\gamma, n)$. The abundances along an isotopic chain in equilibrium depend on temperature, neutron abundance and neutron separation energies $S_n(Z, A) = E_B(Z, A) - E_B(Z, A-1)$, where $E_B(Z, A)$ is the binding energy of a nucleus [14].

The system of differential equations that form the r-process network includes terms for neutron capture, neutron-induced fission, photodissociations, β -decays, β -delayed

neutron emission and fission [22]. Among the several approximations, two are the most frequently used in r-process abundance calculations: the waiting point approximation and the steady-flow approximation. Depending on the specific conditions of the site, β -decays will be faster than neutron capture and photodissociation (s process) or vice versa when the condition $(n,\gamma) \rightleftharpoons (\gamma,n)$ is fulfilled. If the β -flow from Z to $(Z+1)$ is equal to the flow from $(Z+1)$ to $(Z+2)$, then we are in β -flow equilibrium.

The *waiting-point* approximation is valid when the $(n,\gamma) \rightleftharpoons (\gamma,n)$ equilibrium occurs, where the nucleus with maximum abundance in each isotopic chain depends on the chemical equilibrium $\mu_n + \mu_{Z,A} = \mu_{Z,A+1}$ in a Boltzmann gas. The abundance ratios of the neighbouring isotopes depends therefore only on the neutron density n_n, the temperature T and the neutron separation energy S_n:

$$\frac{Y(Z,A+1)}{Y(Z,A)} = f(n_n, T, S_n), \tag{1.23}$$

where the abundances $Y(Z,A)$ are normalised via the sum of mass fractions $\sum_{Z,A} A \cdot Y(Z,A) = 1$ and the neutron separation energy S_n introduces the dependence on nuclear masses [22].
The waiting-point approximation is valid for high temperatures ($T \simeq 10^9 K$) and neutron densities of the order $n_n \simeq 10^{20}\ cm^{-3}$ [22].

As the abundance flow from one isotopic chain to the next is governed by β decays, the total abundance in an isotopic chain is written as $Y(Z) = \sum_A Y(Z,A)$ where $Y(Z,A) = P(Z,A)Y(Z)$, being $P(Z,A)$ the individual population coefficients. If the process' time scale is greater than β -decay half-lives, it reaches a steady-flow equilibrium in addition to $(n,\gamma) \rightleftharpoons (\gamma,n)$ equilibrium (*steady flow* approximation):

$$Y(Z)\sum_A P(Z,A)\lambda_\beta^{Z,A} = Y(Z)\lambda_\beta(Z) = const. \tag{1.24}$$

In this steady-flow equilibrium, the assumption of an abundance for $Y(Z_{min})$ at a minimum Z-value is sufficient to predict the r-process curve and $\lambda_\beta^{Z,A}$ is related to the half-life of very neutron-rich nuclei: $\lambda_\beta = \frac{\ln 2}{T_{1/2}}$. In the conditions in which we have steady-flow equilibrium together with $(n,\gamma) \rightleftharpoons (\gamma,n)$ equilibrium the abundances prediction can be based only on the neutron separation energies and the half-life, and are responsible for the low-mass wings of the $A \simeq 80$ and $A \simeq 130$ peak regions of the Solar System r-process abundances.
The steady-flow approximation is valid before the freeze-out of neutron abundances and temperature and for small β -decay half lives.

The freeze-out from equilibrium can take place in two main modes: as an instantaneous process or as a slow process. In the former case, β -decay properties such as neutron emission and fission are needed, while in the latter individual neutron cross sections are required.
When neutron-rich nuclei are produced beyond their fission barriers, fission can occur during an r-process. In such an environment, β -delayed fission would be the dominant process, as for nuclei with neutron separation energies of the order of 2 MeV, neutron capture will produce compound nuclei with lower excitation energies than β decay. This results in the production of the heaviest nuclei by r process, while fission yields fed back to lighter nuclei. The neutrons emitted in the fission process also contribute to sustain further neutron captures.

In some astrophysical environments such as supernovae, high neutrino flux of different flavours is available. This gives rise to several interactions with nucleons and nuclei

such as elastic/inelastic scattering or electron neutrino or antineutrino capture on nuclei, giving results similar to β transformations. In the scattering processes, neutrinos act towards spallation of the target, rising it to excited states which then decay by photon or particle emission. Neutron capture, instead, leads to the transformation into neighboring elements, with a similar effect as β decay:

$$\nu_e + (Z, A) \rightarrow (Z + 1, A) + e^- \tag{1.25}$$

For these reasons, high neutrino fluxes could mimic fast β^- decays, accelerating the r process to heavy elements.

1.5.4 Nuclear properties

One of the most widely used approaches to determine which of the nuclear properties influences the most the astrophysical models is to directly measure their influence on r-process abundance predictions through sensitivity studies [14].
As a matter of fact, the nucleosynthesis calculations need nuclear properties and reaction rates for thousands of nuclei, from the stability region to the neutron drip line, where the key quantities are nuclear masses, β -decay properties and neutron capture rates.
Theoretical models show comparable predictions for nuclei close to stability, but their results deviate, or even diverge, when we get close to the neutron drip line [14].
In the past, the studies of the classical r process were based mainly on the input of just a few nuclear properties, namely the nuclear mass (from which neutron separation energies S_n and Q_β values can easily be calculated) and the two gross β -decay quantities half-life $T_{1/2}$ and delayed neutron emission probability P_n.
More elaborate dynamical r-process studies require additional nuclear quantities, such as reaction rates, fission barriers, fission fragment yields, and the temperature dependencies of various parameters during the freeze-out phase [15].
To better understand the astrophysical origins of the elements, it is necessary to measure the nuclear properties of a vast area of the nuclear chart. The experimental input data is increasing in recent years thanks to the construction and development of new facilities and techniques to access nuclei far from stability.
Two techniques are mainly employed nowadays to produce very neutron rich nuclei:

- the ISOL (Isotope Separation On-Line) method used at TRIUMF (Canada), ISOLDE at CERN (Switzerland), Jyväskylä (Finland) and SPIRAL1 at GANIL (France),
- the in-flight projectile fragmentation approach employed at NSCL (USA), GSI-FAIR (Germany), RIBLL (China), RIBF at RIKEN (Japan), FRIB (USA).

New facilities are being built all over the world, egs. FAIR at GSI, SPES at LNL. The ISOL approach is based on the use of light projectiles on a heavy target (U) to produce radioisotopes, the latter on the collision of heavy nuclei at relativistic energy on light targets (Be) to produce radioactive unstable fragments [14].

While the ISOL technique provides relative high-intensity and high-purity beams, it is limited to the less exotic species, owing to the slow mechanism used to extract the ions from the thick target. Moreover ISOL techniques do not allow access to all nuclear species, some of which cannot be extracted efficiently from the target. On the contrary, in-flight production allows to produce nuclei over the whole nuclide chart, even if with widely varying cross sections. The relativistic energies usually employed also help reaching the most exotic, and thus shortest living, species. Many nuclei are produced at the same time, which can be both an advantage and a limitation, in terms of count rates.

Nuclear masses

In r-process models, nuclear masses are used in the calculations of the nuclear quantities of interest, mainly in the form of mass differences. They enter in the evaluation of neutron separation energies $S_n(Z,N) = M(Z,N-1) - M(Z,N) + M_n$ and β -decay Q-values $Q_\beta = M(Z,N) - M(Z+1,N-1)$, where $M(Z,N)$ is the atomic mass of the nuclide (Z,N) and M_n is the mass of the neutron. The largest dependence on masses is shown by the photodissociation rates, that are usually calculated from neutron capture rates and masses using a detailed balance:

$$\lambda_\gamma(Z,N) \propto T^{3/2} exp\left[-\frac{S_n(Z,N)}{kT}\right] < \sigma\nu >_{(Z,N-1)} \tag{1.26}$$

where T is the temperature, $< \sigma\nu >_{(Z,N-1)}$ is the neutron capture rate of the neighbouring nucleus and k is the Boltzmann's constant. As the neutron separation energy is in the exponential, a great precision is needed for reliable r-process predictions.
Most of the masses relevant for r process have not been measured yet, only very few of the masses present in the latest Atomic Mass Evaluation (AME2020 [24]), directly impacting on r-process calculations [14].
Nuclear masses are measured experimentally using Penning traps and ion storage rings, which contributed extensively to the AME2020 [24] evaluation.

β decay properties

The β -decay properties that are more relevant to r process are β -decay lifetimes and β -delayed neutron emission probabilities. At present, not all half-lives of nuclei most relevant to the r-process have been measured, in particular around the N=50 and N=82 closed shells. Moreover, no information for half-lives is available approaching the second and third r-process peaks, in the rare-earth region and N>126. Beta-delayed neutron emission probabilities have been measured for neutron-rich Hg and Tl nuclei and isotopes of Au, Hg, Tl, Pb, and Bi in the region of neutron number N $>$ 126 [25]. The recent BRIKEN campaign [26] has further extended the knowledge on the region.
Developing a global model applicable over the entire neutron-rich side of the chart of nuclides is very challenging. At the moment, calculations of β -decay half-lives require a knowledge of the ground-state properties for both parent and daughter nuclei, but the shell model calculations cannot provide details on medium-to-heavy r-process species. Alternative approaches are based on gross theory and a microscopic-macroscopic application of the Quasiparticle Random Phase Approximation (QRPA).
The formula for β -decay halflives can be written as:

$$\frac{1}{T_{1/2}} = \sum_{0 \le E_i \le Q_\beta} S_\beta(E_i) f(Z, Q_\beta - E_i) \tag{1.27}$$

where $S_\beta(E_i)$ is the β strength function, Q_β is the maximum β decay energy and $f(Z, Q_\beta - E_i)$ is the Fermi function.
The probabilities for β -delayed neutron emission can be written as:

$$P_n = \frac{\sum_{S_n \le E_i \le Q_\beta} S_\beta(E_i) f(Z, Q_\beta - E_i)}{\sum_{0 \le E_i \le Q_\beta} S_\beta(E_i) f(Z, Q_\beta - E_i)} \tag{1.28}$$

In these formulae, the β -strength function contains the nuclear matrix elements for the Fermi, Gamow-Teller and first-forbidden or higher order β -decay operators. In gross

theory the discrete energy levels are approximated by statistical functions normalised to the sum rules, while in QRPA models $S_\beta(E_i)$ can be calculated using a folded-Yukawa single-particle potential with pairing and Gamow-Teller residual interactions, as done by [17]. In both models, first-forbidden contributions are estimated using gross theory.
In Figure 1.10 a comparison between experimental halflives from NNDC [27] and theo-

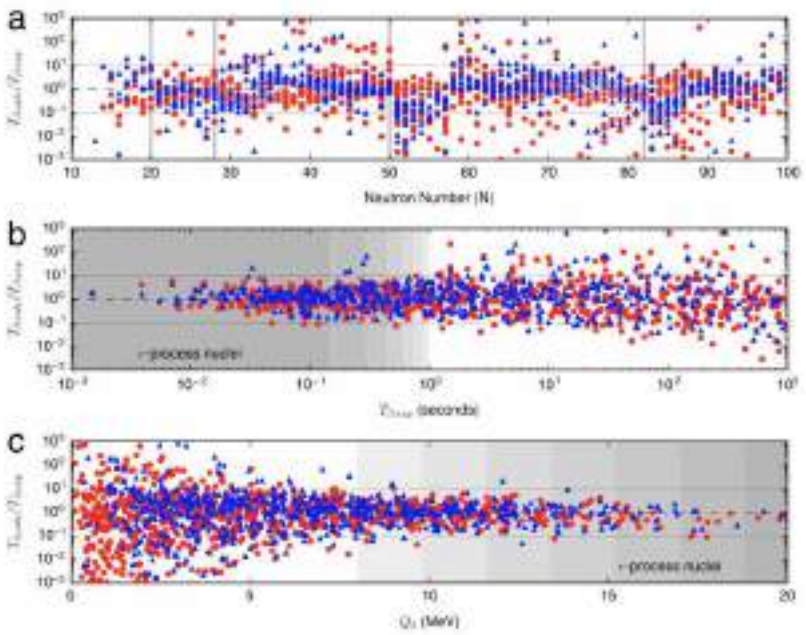

Figure 1.10: Comparison of theoretical β -decay half-lives to measured values from the NNDC database versus (a) neutron number, (b) measured half-life and (c) calculated β -decay Q-values. FRDM1995 + QRPA data points denoted by red circles and KTUY05 + gross theory data points denoted by blue triangles [14].

retical values obtained from global QRPA calculations or with gross theory calculations is shown. From this plot it is evident that extreme discrepancies with theory are reached for the longest halflives and smallest Q_β-values.
Experimental measurements of β -delayed neutron emission probabilities are challenging due to the fact that it is complicated to detect both neutrons and β with high efficiency and resolutions. This will be performed, for example, with the BELEN (Beta deLayEd Neutron detector) detector at GSI-FAIR, or other setups that measure the recoil of the neutron, such as the Hybrid 3HEN, MONSTER (Modular Neutron time-of-flight SpectromeTER), NERO (Neutron Emission Ratio Observer) in coincidence with the BCS (β counting station) at the NSCL.

Neutron capture rates

While an increasing number of experimental measurements is getting available for nuclear masses and β -decay rates, direct measurements of neutron capture on unstable nuclei are not feasible yet. The calculations for capture rates are presently performed using the Hauser-Feshbach (HF) statistical model. This model for (n, γ) reactions is based on the assumption that the captured neutron and target nucleus form a compound system

that exists long enough to come into thermodynamic equilibrium an then decay via γ emission.
The cross section for the (n,γ) reaction $I^{\mu}+n\rightarrow L+\gamma$ where the target nucleus I is in the initial state μ:

$$\sigma^{\mu}_{n,\gamma}(E)=\frac{\pi}{k^2(2J^{\mu}_{I}+1)(2J_n+1)}\sum_{J^{\pi}}(2J+1)\frac{T^{\mu}_{n}(J^{\pi})T_{\gamma}(J^{\pi})}{T_{tot}(J^{\pi})} \tag{1.29}$$

where k is the neutron wave number $k=\frac{\sqrt{2M_{In}E_{cm}}}{\hbar}$, being M_{In} the reduced mass and E_{cm} the centre-of-mass energy, J^{μ}_{I} and J_n are the spins of the target nucleus and neutron, T_{tot} is the total transmission function for the decay of the compound nucleus, T^{mu}_{n} and T_{γ} are the transmission functions for the formation and decay channel respectively, and the sum is over all possible states J^{π}. The transmission rates used in this formula for r-process nuclei are unfortunately not available from experimental data, and are, therefore, extracted from models of nuclear level densities. The model variations become very wide when moving away from the stability valley.
The measurement of neutron capture rates is exceptionally difficult because it requires significantly intense beams on very rare and short-lived radioactive targets. This quantity is now measured mainly through indirect approaches such as surrogate reaction techniques or the β -Oslo method. The former is based on the determination of cross sections for nuclear reactions that proceed thorough a compound nucleus via a surrogate reaction (usually (d,p) reactions) which is easier to measure. This can be done because the compound nucleus does not have a memory of its formation process. In the latter method the high-lying levels in the nucleus of interest are populated via β decay and a total absorption spectrometer is used to measure γ rays and therefore to determine the level density and the γ -ray strength function.

1.6 *Dataset1* and *Dataset2*

Two datasets are presented in this work. Both experiments were performed at the GSI-FAIR facility using the FRS+DESPEC setup, whose setups and data taking techniques are discussed in Chap.2. The two experiments were part of the same experimental campaign that took part in spring 2021.

The primary aim of the experiment we refer to as *Dataset1* was to find evidence of octupole deformation in the A $\simeq$ 222 region and to provide new β decay information beyond N = 126 (Fig. 1.11). This was the main topic of the PhD project this work aims at presenting.

The second experiment, referred to as *Dataset2*, was focused on the p-rich ^{100}Sn region (Fig. 1.12). The main goals of this experiment were to study core-breaking effects in the region by extending the knowledge on the $B(M1)$ trend in odd-A tin isotopes and on the $B(E2)$ trend in even-even tin isotopes. The aim was to do this by populating ^{103}Sn via α decay of ^{107}Te and to measure the lifetime of its $(7/2+)$ isomer, and to populate ^{102}Sn directly and measure the lifetime of its first $4+$ state. Many nuclear species were also populated via β decay. This thesis is focused, in particular, on the ^{100,101,102}Cd isotopes, which is an intermediate result. Further analysis is being performed in order to reach the primary goals of the experiment.

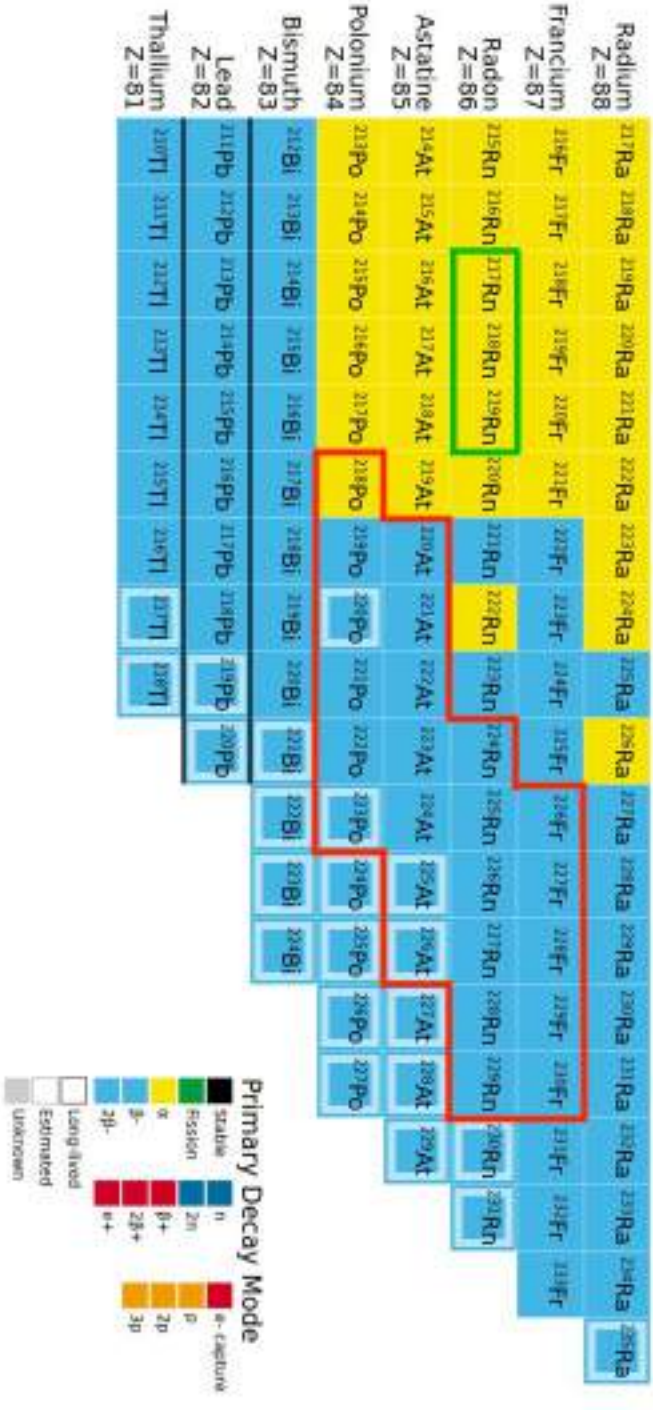

Figure 1.11: Region of the nuclear chart where *Dataset1* was focused, i.e. the heavy n-rich region beyond N = 126. The nuclei of interest are highlighted with a red line, while the nuclei populated for intermediate settings are highlighted with a green line.

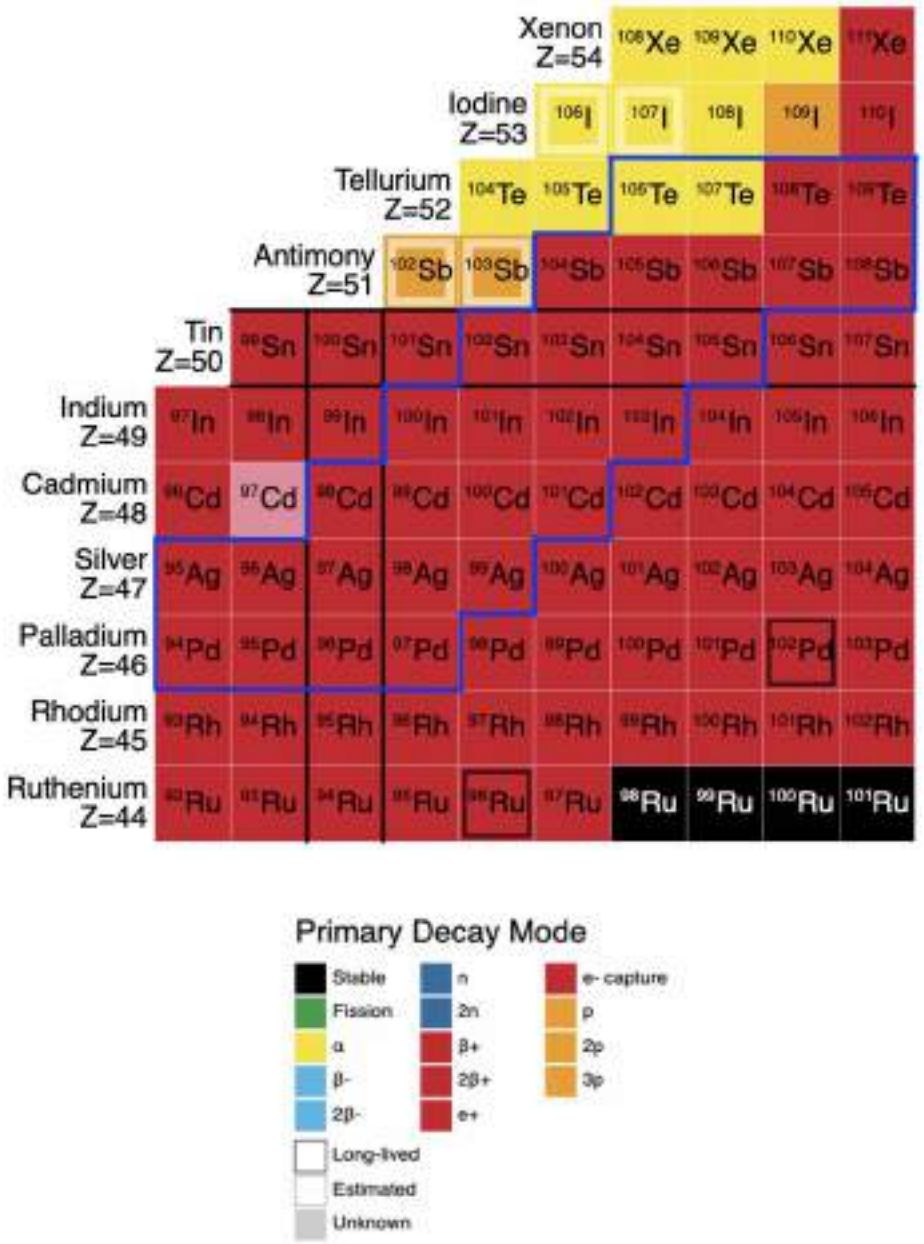

Figure 1.12: Region of the nuclear chart where *Dataset2* was focused, i.e. the p-rich region around ^{100}Sn. The nuclei of interest are highlighted with a blue line.

CHAPTER 2

Experimental Setup

The GSI laboratories are one of the main facilities in the world for nuclear physics studies, where stable beams of species up to uranium can be produced and accelerated to relativistic energies. This allows to perform frontier studies both in nuclear physics, particle physics, medical and material applications.

2.1 The GSI acceleration system

A schematic of the GSI facility is displayed in Fig.2.1, where the accelerators as well as the main experimental halls are indicated.
The accelerator system is composed of an ion source, a linear accelerator and a synchrotron, which will be described in this chapter.

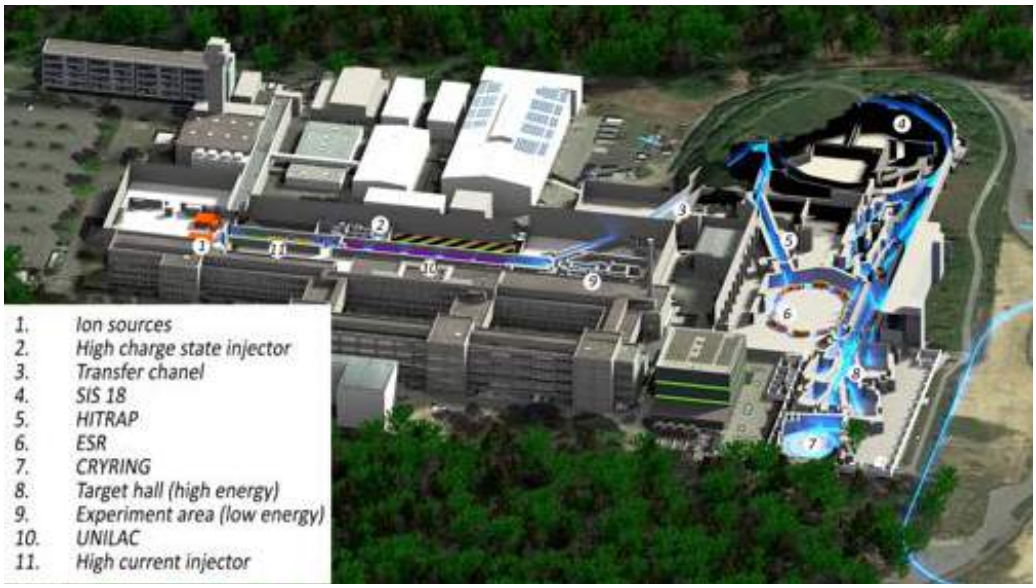

Figure 2.1: The GSI accelerator facility (adapted from the GSI website)

2.1.1 The UNIversal Linear Accelerator (UNILAC)

The UNIversal Linear Accelerator (UNILAC), displayed in Fig. 2.2, is the first stage of the GSI accelerator system, and it can accelerate all ion species from protons to uranium to 16% of the velocity of light (11.4 MeV/u).
Positively-charged ions can be produced using three different ion sources. Highly charged ions at low intensity are provided by the Electron Cyclotron Resonance (ECR) source. The Penning Ionization Gauge (PIG) source delivers low and intermediate charged ions at low intensities. High intensity beams of low charged ions are provided by the third terminal which can be equipped with a MEtal Vapor VAcuum Arc (MEVVA) source, VARIS (Vacuum ARc Ion Source), MUlti-Cusp Ion Source (MUCIS), or Cold or HOt Reflex Discharge ion Source (CHORDIS). The uranium beam used for this work was delivered by the VARIS source, which is optimized for operation with heavy elements. It provides the best charge-state distribution for uranium ions (67% of $^{238}U^{4+}$) [28].
Ions in the UNILAC are accelerated in two subsequent steps. In the first stage, the beam is electrostatically extracted from the source, it is bunched ad pre-accelerated in Radio-Frequency-Quadrupole (RFQ) cavities and accelerated using Inter-Digital (IH) cavities to $5\ \%$ of the velocity of light (1.4 MeV/u). At the end of the first stage, the ions pass through a gaseous medium to strip off the outer electrons in order to increase the ion charge state and, therefore, to enhance the efficiency of further acceleration of low-charged beams.
The second stage comprises five Alvarez-type cavities that bring the ion beam to the final energy. A final section, composed of several single-gap resonators (ERs), allows to set the ion energy between 3.4 and 11.6 MeV/u. Afterwards the beams may be passed through the Transfer Channel (TK) towards the synchrotron SIS18 for further acceleration or to various experimental branches.

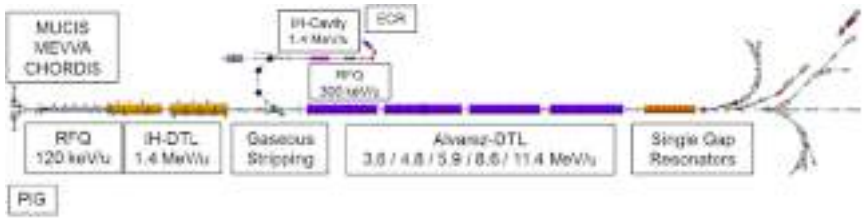

Figure 2.2: The UNILAC accelerator (adapted from the GSI website)

2.1.2 The SIS-18 synchrotron

The beam, accelerated from the UNILAC, is then injected in the SIS-18 synchrotron, shown in Fig.2.3. The SIS18 can accelerate ions of all natural chemical elements of the periodic table, from protons to uranium, to a maximum energy of 4.5 GeV in the case of proton and 1 GeV per nucleon in the case of $^{238}U^{73+}$.

The accelerated primary beam from SIS-18 is transported to the production target at the entrance of the Fragment Separator (FRS) [29]. This synchrotron has a radius of 34.5 m and its 24 dipoles can provide a maximal bending power of 18 Tm. The accelerating potential is achieved through two radiofrequency cavities at 16 kV. In *Dataset 1*, the SIS-18 energy output for ^{238}U ions was set to 1 GeV/u, producing a beam with $\sim 10^9$ pps intensity and spill length of 4 s. In *Dataset 2*, instead, a ^{124}Xe beam was accelerated to 839.35 MeV/u with an intensity of $2 \sim 10^9$ pps intensity and a spill length of 1 s.

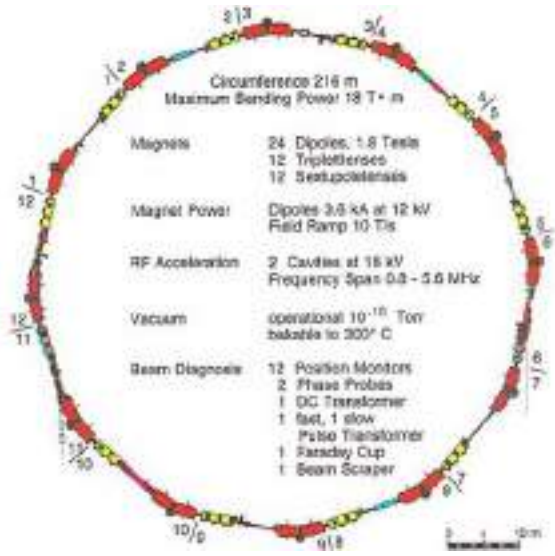

Figure 2.3: The SIS-18 accelerator (adapted from the GSI website)

2.2 The FRagment Separator (FRS)

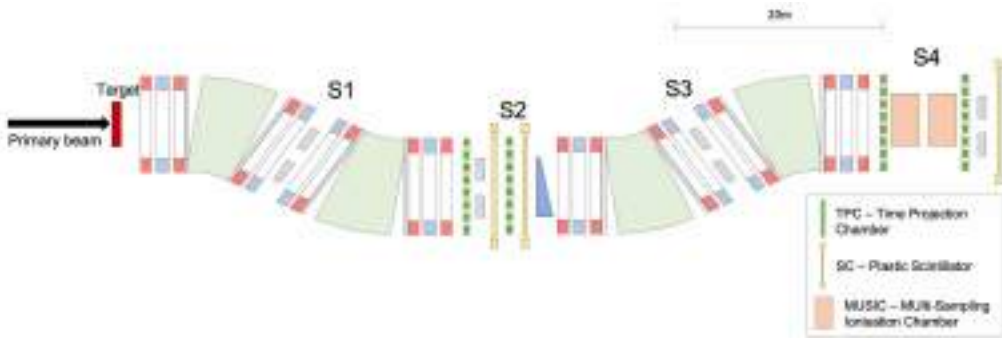

Figure 2.4: The FRagment Separator (FRS). The bending and focusing magnets and the detectors along the spectrometer are shown.

The ions of interest were produced exploiting fragmentation reactions of a relativistic beam impinging on a ^{9}Be target. Fragmentation reactions produce a vast number of different fragments which form a so-called cocktail beam. Therefore, there is a need to select and identify each different ion species to perform focused studies on their properties and decays. In order to do this, at GSI the FRagment Separator (FRS) is employed in research studies using relativistic heavy ions [29], and it has a momentum resolving power of 1500 for an emittance of 20π mm mrad. Heavy-ion beams with magnetic rigidities ranging from 5 to 18 Tm can be analyzed using this spectrometer.
The FRS is divided in four independent stages (S1-S4 in Fig.2.4) each comprising a 30° dipole to bend the secondary beam. First-order focussing and second order aberrations are achieved by a set of quadrupole and sextupole magnets placed before and after the

dipole. The quadrupole placed before the dipole magnet can be adjusted in order to properly illuminate its field volume and, therefore, to achieve the best resolving power and minimize the vertical gap width. The quadrupole following the dipole determines the ion-optical conditions at the four focal planes [29]. Second order aberrations of the beam optics are corrected by using sextupole magnets placed before and after each dipole magnet.

Along the FRS, five sets of copper slits are placed, allowing to cut the acceptance of the spectrometer. These instruments can be used to remove ions with a certain magnetic rigidity, stopping unwanted ion species from reaching the final focal plane (S4) where our decay station is placed.

The first two dipole stages (S1 and S2) of the FRS perform an A/Z selection of the projectile fragments. A wedge-shaped degrader, placed in the intermediate focal plane, allows a second filter on the basis of different atomic energy loss of the ion. The separation is then completed with the remaining two dipole stages (S3 and S4). This separation method is known as the Bρ - ΔE - Bρ method [29].

The identification of the ion species is achieved by employing a series of detectors along the FRS, that provide a measurement of the time of flight, the energy loss and the trajectory of each ion. This identification method is known as the ToF - ΔE - Bρ identification method [30].

2.2.1 The Bρ - ΔE - Bρ separation method

Being a magnetic spectrometer, the FRS system separates the secondary fragments according to the ratio of mass number over ionic charge and velocity according to the magnetic rigidity. A picture of the FRS magnets before the intermediate focal plane is shown in Fig. 2.5.

Dipoles

The four dipole magnets of the FRS bend the trajectoriy of ions at different angles according to their magnetic rigidities.

They have a nominal radius of 11.5 m and a deflection angle of 30°.

The motion of an ion in a homogeneous magnetic field is given by the Lorentz force:

$$\vec{F}_{Lorentz} = \frac{d}{dt}(m \cdot \vec{v}) = q\vec{v} \times \vec{B}. \tag{2.1}$$

When the magnetic field is perpendicular to the ions momenta, the Lorentz force compensates the centrifugal force:

$$F_{Lorentz} = \frac{mv^2}{\rho} \tag{2.2}$$

where ρ is the radius of the ion trajectory.

Therefore, the motion of fragments in the dipole field will be given by:

$$B\rho = \beta\gamma\frac{A}{q}uc \tag{2.3}$$

where B is the magnetic field, β and γ are the relativistic kinematics parameters, A is the mass number and q is the ionic charge.

Figure 2.5: Magnetic elements in the FRS: a dipole (green) and a series of quadrupoles (yellow) before and after.

Slits

FRS slits are pairs of thick copper blocks placed along the beamline. Their high thickness can stop all fragments impinging on them and allows only ions between them to pass, both in X and Y direction. Therefore, the slits can cut the acceptance of the spectrometer, removing ions with a certain magnetic rigidity. This can be used to to reject unwanted species, thus preventing too high counting rates on the detectors.

Degraders

The degrader in the middle focal plane consists of three main components, as shown in Fig. 2.6: a homogeneous variable degrader (double wedge), a ladder where different degrader thicknesses can be selected and two wedge-shaped disks. All these components are made of aluminum. The degrader system can reach an overall thickness between 270 and 6570 mg/cm^2. The double wedge and the ladder are homogeneous with respect to the X position, so that their thickness does not vary with X. The degrader disk instead can be rotated along the beam axis thus changing its slope. By varying this angle, different ion optical modes can be achieved, known as monochromatic and achromatic modes. In the monochromatic mode, the degrader is shaped so that the energy loss of the ions can compensate their initial momentum spread. This is often used in implantation experiments, where the requirement is for all fragments of the species of interest to implant in the same layer thickness. The achromatic mode, instead, preserves the ion-optical achromatism in the final focal plane. To achieve this, the optimum angle is the one that does not change relative momenta, but rather maintains the same energy ratio between nuclei before and after the degrader.

The FRS was set in achromatic mode for *Dataset 1*, as the implantation detector used was narrow. An intermediate mode, not fully achromatic nor monochromatic, was used for *Dataset 2* as the implantation detector was wider, thus allowing for a larger spread in X direction.
Another homogeneous degrader is placed at the final focal plane, before the decay sta-

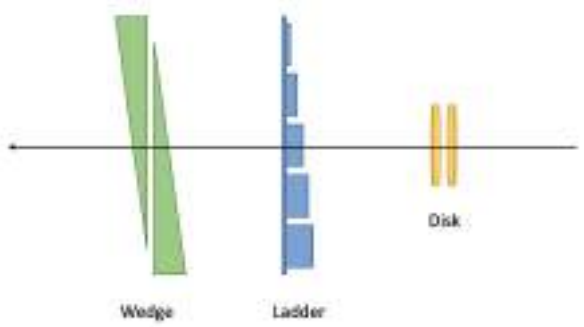

Figure 2.6: The degrader system at S2, consisting of a wedge-shaped degrader, a homogeneous ladder and wedge-shaped disks

tion, in order to slow down the ions exiting the FRS and implant at the correct thickness in the implantation detectors. In this case a homogeneous aluminum degrader is used.

The first stage of the separator selects bands of isotopes having a constant A/Q ratio, i.e. ions with the same magnetic rigidity are focused at the same position at S2 [30]. The spatial distance in horizontal direction between two ions with different magnetic rigidity $B\rho$ is proportional to their relative difference in magnetic rigidity:

$$\Delta X = D \cdot \frac{\Delta(B\rho)}{B\rho} \tag{2.4}$$

where D is the ion-optical dispersion parameter.
After this first separation, the degrader wedge at the intermediate focal plane operates a selection on the basis of the atomic number Z of the ions. Ions deposit an energy proportional to Z^2 according to the Bethe-Bloch formula:

$$\Delta E = \frac{4\pi e^4 Z^2}{m_e v^2} \cdot Nz \cdot \left[\ln\left(\frac{2m_e v^2}{I}\right) - \ln(1-\beta^2) - \beta^2 \right] \tag{2.5}$$

being Z the ions' atomic number, e the electronic charge, m_e the rest mass of an electron, N the number of the absorber atoms, z the atomic number of the absorber atoms and I the excitation and ionisation of the absorber atoms [31].
As a consequence, their $B\rho$ is also affected. The third and fourth magnets operate a selection on the new $B\rho$ of the fragments, implying now a selection in Z.

2.2.2 The ToF - ΔE - Bρ identification method

The selected ions are identified with the TOF - Bρ - ΔE method [30] in the FRS thanks to several detectors collecting, on an event basis, the ions' time of flight, position in the focal planes, and atomic number Z (see Fig. 2.4). A closer look on the detectors present at the S2 and S4 focal planes is shown in Fig. 2.7 and 2.8.

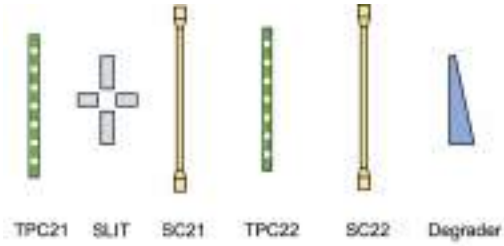

Figure 2.7: The FRS detector system at the middle focal plane (S2)

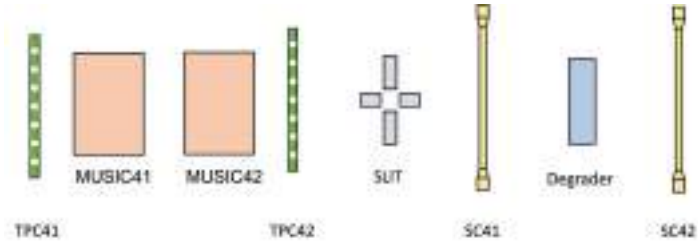

Figure 2.8: The FRS detector system at the final focal plane (S4)

Plastic scintillators

Two plastic scintillators are placed in the middle (SC21, SC22) and final (SC41, SC42) focal planes with the purpose of measuring the time of flight (TOF) of fragments passing along the FRS.
The FRS scintillators are made of BC-420 plastic, which is characterized by a high efficiency in light production and by a fast time response (1.5 ns). The active area of the detector is of 200×80 mm^2, with thickness varying between $0.5 - 3.5$ mm.
The light emitted by the scintillator is read out by two PhotoMultiplier Tubes (PMTs) glued on the left and right side. The average between the left and right signals is proportional to the time the ion has crossed the detector, the difference between the signals provides a measurement of the position of interaction with the detector, while the intensity of the signal is proportional to the energy released by the ion.
The time resolution is 40 ps, while the space resolution is 4 mm.
The scintillators' signal is readout using three acquisition systems: the traditionally used analog electronics (TAC - Time to Amplitude Converter), a multi-hit digital one (MHTDC - Multi-Hit Time to Digital Converter), and a digital FPGA-based electronics (VFTX - VME FPGA TDC). A discussion on the selection of the most suitable electronics for *Dataset1* and *Dataset2* is given in Sec. .

The maximum count rates that scintillator detectors can handle is of the order of 10^6 pps. As higher rates are foreseen for future developments of Super-FRS [32], a segmented plastic detector, the *Finger* detector, is currently under development. The Finger is composed of several plastic scintillator strips, each one read individually and capable of high rate handling. In addition, this detector will give enhanced position resolution.

Figure 2.9: Picture of a scintillator detector out of the beamline

Time Projection Chambers (TPC)

Time Projection Chambers are detectors used for the measurement of the position in the FRS (see picture in Fig. 2.11). The detector has a vertical drift direction with respect to the beam direction. As shown in the schematic in Fig. 2.10, the drift space is placed inside a field cage terminated by a gating grid on the lower side. Four proportional counters with C-pad cathodes are placed underneath the grid.

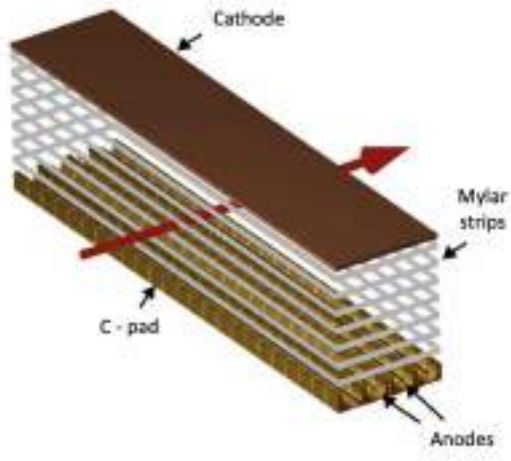

Figure 2.10: Schematic of a TPC (Time Projection Chamber) detector.

Figure 2.11: Picture a TPC (Time Projection Chamber) detector out of the beamline.

The drift volume is filled with Ar + 10% CH_4 gas, also known as P10, at atmospheric pressure and room temperature. The drift space is surrounded on both sides by mylar strips (3 mm wide and 20 μm thick), connected to high-resistance divider, to which a voltage up to 400 V/cm is applied. The high voltage forms an uniform electric field inside the cage, that affects the drift velocity of the electrons. Underneath the drift space, a proportional (sensitive) counter, consisting of four anodes wires inside C-shaped cathodes, is present. The C-pads are connected to an integrated passive delay line [33].

The y position of the ions is obtained by measuring the electrons drift time:

$$y = w_d \cdot t_d + y_{off} \tag{2.6}$$

where t_d is the anode signal, w_d and y_{off} are calibration parameters. The x position is determined by measuring the time difference between the arrival of the induced signal from the left and right side of the delay lines:

$$x = w \cdot (t_l - t_r) + x_{off} \tag{2.7}$$

where w and x_{off} are calibration parameters. Each TPC detector provides two independent measurements of the x position and four of the y position. Being its position resolution of 1 mm for the x and 0.5 mm for the y position, the TPC detector is the preferred device for position measurement in the FRS. As a consequence, position information from the scintillators is generally not used, unless unusual conditions are present, such as very high rates which might lead to pile up effects in the TPC.

MUlti Sampling Ionisation Chambers (MUSIC)

At the final focal plane of FRS, two MUlti Sampling Ionisation Chambers (MUSIC) detectors provide a measurement of the atomic number Z of the fragments reaching it. As

shown in the schematic in Fig. 2.12, the MUSIC detector is an ionisation chamber filled with pure CF_4 gas at atmospheric pressure and room temperature. The chamber has a homogeneous entrance window made of thin float glass with integrated field homogenization, consisting of aluminium strips (1 μm) deposited on the float glass and a voltage divider. Each anode strip is read out with a charge sensitive preamplifier and shaper optimised for rates up to 200 kHz [34].

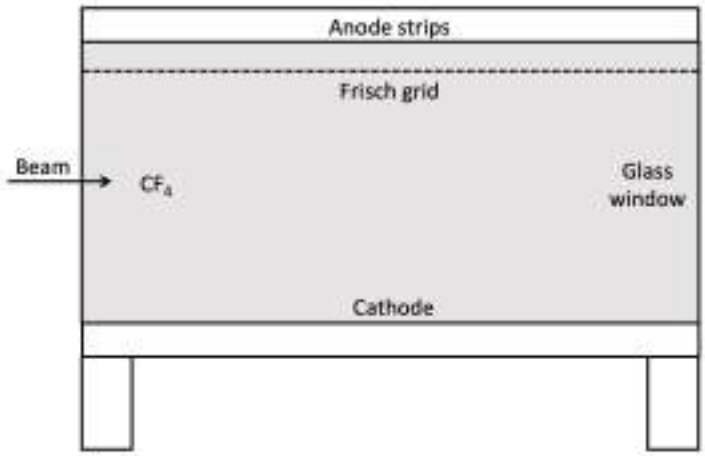

Figure 2.12: Schematic of a MUSIC detector

Charged particles passing through the active volume ionise the gas, creating clouds of ions and free electrons. When an electric field is present, the free electrons will drift towards the 8-fold segmented anode. This allows to obtain a measurement of the energy loss of each fragment in the MUSIC detector as the geometrical average of the 8 anodes:

$$\Delta E = \sqrt[8]{\prod_{i=1}^{8} \Delta E_i} \tag{2.8}$$

The energy loss of the fragments is, at first order approximation, proportional to the square of its atomic number according to the Bethe-Bloch formula 2.5. As the MUSIC chambers are not sealed, the gas contained is subject to variations in volume, caused by external temperature and pressure variations.

2.3 The DEcay SPECtroscopy (DESPEC) station

The DEcay SPECtroscopy station [35] was commissioned in 2019 and used in the following campaigns (Fig. 2.14). It comprises several detector systems used for decay experiments. The ions are implanted in a stack of 2-3 layers of Double-Sided Silicon-strip Detectors (DSSD) highly segmented, the AIDA (Advanced Implantation Detector Array) [36]. This active stopper is also used to detect α and β particles emitted by the ion after its decay. The silicon detectors are sandwiched between two plastic scintillators, the βPlastic detector, which are made of tiles of scintillator material, used for timing measurements of the β particle emitted in the decay.

The γ rays emitted in the de-excitation of the daughter nuclei are detected using a hybrid array for γ -ray detection. The FATIMA (FAst TIMing Array), comprising 36 $LaBr_3$(Ce) detectors, having a full-energy peak efficiency of 2.9% at $\sim$1 MeV. Precise γ -ray energy measurements are performed with four 7-fold HPGe clusters, in forward position as depicted in Fig. 2.13. This germanium array has an efficiency of 2% at $\sim$1 MeV.

Figure 2.13: Schematic of the DESPEC decay station.

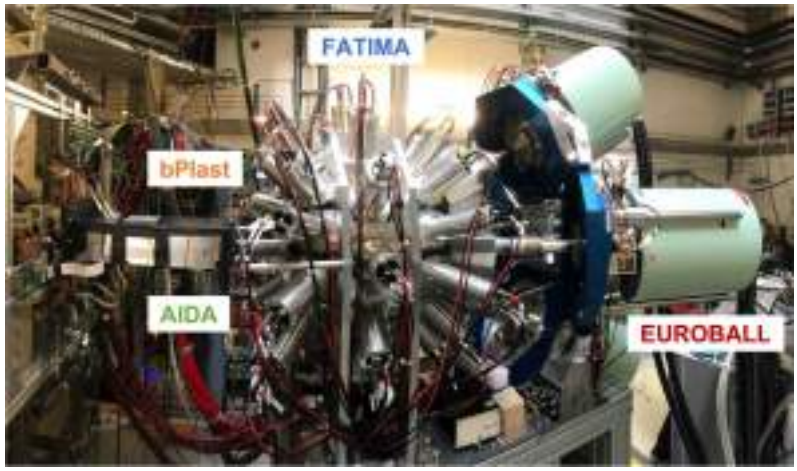

Figure 2.14: Picture of the DESPEC decay station at GSI.

All the subsystems involved have independent data acquisition systems that are synchronised using a time sorter, schematically shown in Fig. 2.15. Time stamping correlations are established between the systems using a distributed clock, the so-called White Rabbit, and a 2 Hz pulser. The GSI White Rabbit ([37]) has an absolute start time, corresponding to midnight on January 1^{st}, 1970, is driven by a 125 MHz clock, and distributed to the DESPEC subsystems via Ethernet. The timestamp accuracy can be up to $\sim$ 1 ns and depends on the type of the receiving board.

A data unpacker called *ucesb* (unpack and check every single bit) is used to build AIDA events and to time-stitch the data for subsequent analysis. The time-stitching process combines near events from different subsystems into a single event, such that all the different subsystem data may be accessed at once in subsequent analysis or for ROOT

trees generation. A DESPEC event is thus formed from all the subsystems sub-events occurring in a 2 μs interval. This procedure is schematically depicted in Fig. 2.16.

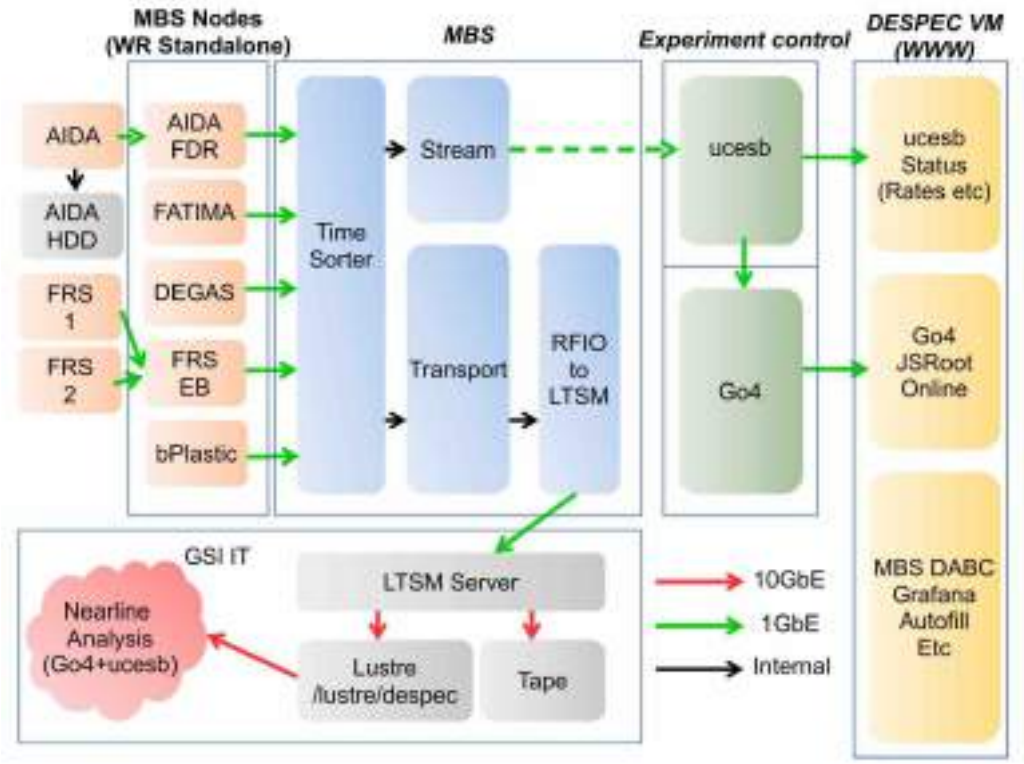

Figure 2.15: Schematic of the DESPEC DAQ architecture. Data from individual subsystems are fed into the timesorter for event building. They are then sent to the *ucesb* for time-stitching. The data is then both stored and streamed to online analysis. Adapted from Ref. [35].

This setup allows to perform β decay measurements by correlating the implanted ion and the β particle in the silicon detectors, using position and timing conditions. The γ rays detected in the FATIMA and HPGe detectors can then be correlated to the ion and/or β to probe the inner structure of the daughter nuclei, establishing β -γ -γ correlations. Alpha decay studies can be performed in a similar fashion by correlating the implanted ion with an α particle detected in the silicon detectors.

2.3.1 Advanced Implantation Detector Array (AIDA)

The highly energetic heavy fragments selected and trasported by the FRS, are slowed down within a degrader in the final focal plane and stopped in an implantation detector. The AIDA (Advanced Implantation Detector Array) is a device for implantation and decay detection composed of a stack of Double-sided Silicon Strip (DSSD) layers [36]. AIDA tiles are 8 cm $\times$ 8 cm, with ~ 1 mm thickness and 0.560 mm inter-strip pitch and they can be arranged in a single tile (*narrow*) or three tiles (*wide*) arrangements. Each tile is segmented into 128 vertical and horizontal strips in the *narrow* configuration, for a total of 16384 pixels per detector in the narrow and 384×128 pixels in the *wide* configuration,

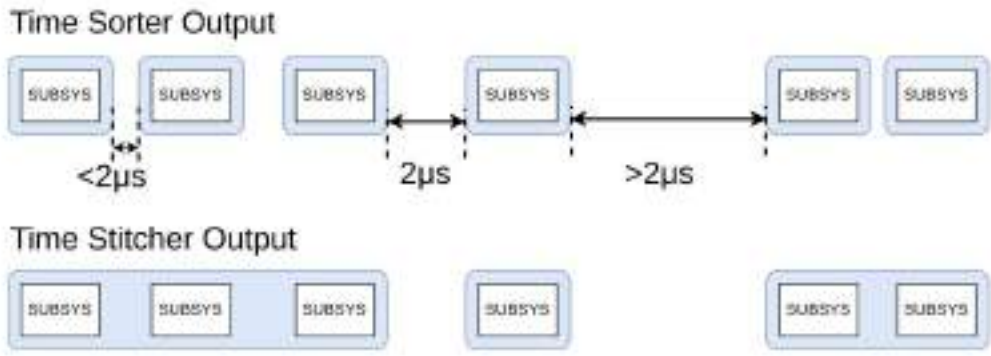

Figure 2.16: Schematic of the *ucesb* time-stitching algorithm. Events from subsystems occurring in less than 2 μs from the previous are grouped together. Adapted from Ref. [35].

where y strips have a common read outfor the three tiles. For *Dataset 1* three layers of the *narrow* configuration were used, while for *Dataset 2* two layers of the *wide* were employed. A picture of the detector array as it is used in the *narrow* configuration is displayed in Fig. 2.17, where the three DSSD layers are sandwiched between the two βPlastic detectors, described in Sec. 2.3.2. This arrangement is placed in an aluminium case, known as the AIDA *snout*.

The signal amplification, shaping and multiplexing is performed using a custom ASIC (Application Specific Integrated Circuit) chip, each of which has 16 channels. Each 16 channel ASIC has 16 digital ADCs (50 MSPS, 12-bit) and one analogue ADC (500 kSPS, 16-bit). The system also has a fast recovery time of ≤ 40 μs. Simultaneous events within the same ASIC are read 2 μs apart from each other. The AIDA hardware consists of 64-channel FEE64 (Front End Electronics) modules which control and process the data from four AIDA ASICs. Each FEE64 operates as an independent DAQ (Data Acquisition System) and can handle data rates of up to 500 k data items/s.

The acquisition system works in trigger-less mode, i.e. each channel triggers itself, is read out by an FPGA (Field-Programmable Gate Arrays) and is time-stamped using White Rabbit. The time-stamping allows for each FEE64 module to synchronise with the others and also for the AIDA to be synchronised with the other subsystems in the DESPEC setup.

The heavy ions implanting in the AIDA can undergo radioactive decay, emitting β , α particles, neutrons and γ rays. The charged particles are also detected in the DSSD. While the implanted ions carry an energy in the GeV range, decay events have an energy of ~ 10 keV to ~ 10 MeV. In order to be able to measure both categories of events, a very wide dynamic range is required. This is achieved by two different acquisition modes: a high gain branch ($0 - 20$ MeV) for decay events, and a low gain branch ($0 - 20$ GeV) for implantation events. Both ranges have a linear output, ensuring good resolution and intuitive analysis.

The pixelation of the detectors allows for the measurement of the position of the implanted ions and the subsequent decays.

Figure 2.17: Picture of the AIDA detectors on the test bench. The three DSSD layers are sandwiched between the two βplastic detectors.

2.3.2 Beta plastic detectors (βPlastic)

The βPlastic (Beta Plastic) detector is a fast-timing plastic scintillator that is designed for the timing measurement of β particle with an energy of ~ 80 keV to ~ 8 MeV. This detector consists of a tile of rectangular 3 mm thick sheet of scintillating plastic material (type BC-404), coupled to a series of 3×3 cm^2 silicon photomultipliers (SiPM) attached to each side with an optical coupling pad (Fig. 2.18). The SiPM signals are read out by custom-made, shielded flat cables and then pass through *booster boards*, which provide an amplification factor of ~ 10. The amplified signals are fed to FPGA-based TAMEX cards with TwinPeaks front-ends, developed in-house by the Experimental Electronics Department at GSI [38]. The TAMEX architecture will be further explained in Sec. 2.3.3. Two βPlastic detectors cover the same area as the AIDA detectors, and are placed in the same snout, upstream and downstream from the DSSD.

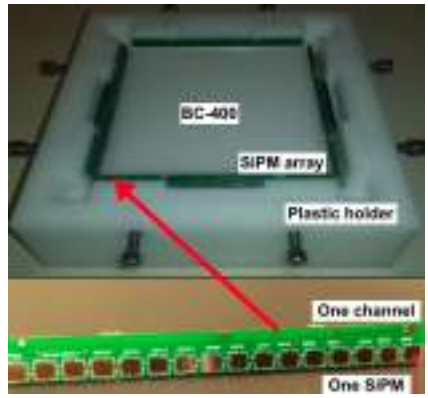

Figure 2.18: Picture of a βPlastic detector out of the beamline. The scintillator material and the SiPM readout are highlighted by labels.

To measure short nuclear lifetimes associated with the time difference between β particles and the γ rays, given the limited time resolution of the AIDA detectors ($\sim$ ns), faster timing detectors are needed. Time difference between a γ ray and the β particle is crucial to determine the lifetime of the excited states of the daughter nuclei. If the β particle leaves the DSSD and hits one of the plastic detectors, a fast signal is obtained. A time resolution of ~ 450 ps FWHM for 511 keV γ rays was measured using a ^{22}Na source, where the 511 keV photon emitted in the opposite direction was detected by a LaBr3(Ce) (FATIMA) detector.
The βplastic detector can also be used as an implantation device, to increase the active depth for heavy ions. It can as well serve as a high-efficiency veto of unwanted light ions that may pass through the AIDA stack without being stopped. Moreover, one can establish $\beta - \gamma$ correlations and study the decay scheme of the daughter nuclei by correlating γ rays with β particles detected in βPlastic off spill (i.e. when the beam spill is not present).

2.3.3 FAst TIMing Array (FATIMA)

The FATIMA (FAst TIMing Array) at GSI ([39] [40]) comprises 36 $LaBr_3$(Ce) detectors, arranged in three concentric rings around the AIDA detector (Fig. 2.19). Each detector consists of a $LaBr_3$(Ce) (5% Ce doping) crystal of 1.5" diameter and 2" length, optically coupled to a fast R9779 photomultiplier tube (PMT) with 8 dynode stages. Each detector is equipped with a removable lead cap of 4 mm thickness around the crystal to provide passive shielding and minimise scattering among neighbouring detectors.

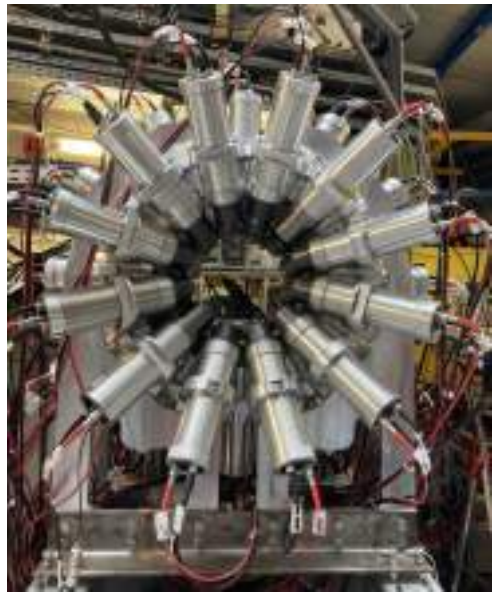

Figure 2.19: Picture of a the FATIMA array.

The front face of each detector is tangent to a sphere around the focus point, at 16 cm from the centre of AIDA. Each ring accommodates 12 detectors, positioned at $44°$, -$6°$, and -$44°$ with respect to a plane orthogonal to the beam direction. The middle ring is offset from $0°$ to avoid the shadow of the AIDA frame in the centre of the ring. For *Dataset 2* the

FATIMA detectors were retracted from their original position of ~ 2 cm to accommodate the wide AIDA+βPlastic configuration. During the experimental campaign, FATIMA data were handled with two independent acquisition system: the largely used VME-DAQ, and the custom-made TAMEX electronics [38].

For the VME-DAQ, the energy information is derived from the dynode signal, while the anode signal carries the time information. Each dynode signal is processed by V1751 CAEN digitisers, operated using the Digital Pulse Processing-Pulse Shape Discrimination (DPP-PSD) firmware provided by CAEN. The digitisers offer a sampling rate of 1 GS/s, which allows several samples on the signal rise time of the detectors. The energy information is obtained via signal integration above a dynamically determined base line level (charge to digital conversion, QDC). CAEN V812 constant fraction discriminator (CFD) modules are used for time pick-off of the anode signals. All CFD signals are fed into V1290 time to digital converters (TDC) modules, having 32 channels each. The TDC modules have a time resolution of ~ 25 ps and 21 bit range. The time resolution for the individual final TDC measurement is of ~ 35 ps.

The TAMEX-DAQ is an in-house developed pulse-processing technology [38] comprising electronic cards with a TwinPeaks front-end, customised to FATIMA PMTs signal pulses. TwinPeaks uses two discrete amplifiers to process PMT signals, a logarithmic and a linear amplifier. A high bandwidth amplifier is sensitive to small amplitude pulses generated by the PMT, and the time-over-threshold (ToT) has a logarithmic dependence on the detector pulse charge/deposited energy. A linear amplifier, instead, offers a linear relation between deposited energy (pulse charge) and pulse width (ToT). The timing information is extracted using the time difference between leading edges of pulses generated by consecutive γ rays, provided by the logarithmic branch. The energy information is extracted from the time-over-threshold spectrum. TAMEX offers an optimal time resolution of 11 ps, a very low dead time (~ 20 μs), a high data throughput $\sim 85\%$ with a long collection window (~ 320 μs).

2.3.4 EUROBALL HPGe detectors

In the DESPEC setup, an array of four EUROBALL 7-fold clusters was used [41], forming a cross in the forward direction as shown in Fig. 2.14 and Fig. 2.20. Each cluster contains seven tapered, hexagonal HPGe crystals, with a central crystal and the other six surrounding it, thus forming an array of 28 germanium capsules in total. The clusters are positioned in a cross configuration in forward position, forming an hemisphere at a distance of ~ 29 cm.

The germanium detectors were read out by 14 bit 100 MHz FEBEX digitisers developed at GSI, FEBEX [42]. An on-board FPGA is used to apply a trapezoidal filter algorithm to obtain energy information, while time information is determined from the on-board constant-fraction discriminator. Synchronisation with the other subsystems is achieved by White Rabbit timestamps. The energy resolution obtained varied between 2.3 keV and 3.1 keV at 1.3 MeV in different crystals.

2.4 Setup used for *Dataset1* and *Dataset2*

Both experiments presented in this thesis work were performed at GSI-FAIR with the FRS+DESPEC setup. Nevertheless, for each dataset specific settings were needed for the FRS, in order to optimise the implantation of the various ions of interest. The details of the two settings are presented in Tab. 2.1.

Figure 2.20: Picture of a the euroball array from the upstream point of view. The clusters are positioned in a cross configuration in forward position, after the FATIMA array.

	Dataset1	*Dataset2*
Primary Beam	^{238}U (1 GeV/u, 10^9 pps)	^{124}Xe (839.35 MeV/u, 2×10^9 pps)
Target	^{9}Be 1600 mg/cm^2	^{9}Be 6333 mg/cm^2
Central fragment	^{225}At	^{102}Sn
Stripper	Nb 223 mg/cm^2	Nb 857 mg/cm^2
D1 magnet	$B\rho$ 13.7127 Tm	$B\rho$ 7.5566 Tm
D2 magnet	$B\rho$ 13.7127 Tm	$B\rho$ 7.5566 Tm
S2 Degrader	Al 2470 mg/cm^2 3,36 mrad	Al 1500 mg/cm^2 -2.78 mrad
D3 magnet	$B\rho$ 11.5023 Tm	$B\rho$ 6.3827 Tm
D4 magnet	$B\rho$ 11.5023 Tm	$B\rho$ 6.3827 Tm
S4 Degrader	Al 5073 mg/cm^2	Al 2500 mg/cm^2

Table 2.1: FRS settings used for *Dataset1* and *Dataset2*.

Moreover, slight changes were made in the DESPEC station in the two cases, as explained before in the chapter. In particular, in *Dataset1* experiment, AIDA+bPlast in the *narrow* configuration were used, while the *wide* configuration was installed for *Dataset2* experiment.

2.5 The transport of ions: LISE++ simulation

In order to verify the feasibility of the experiment and to perform a simulation of the transport of ions through the separator to the decay station, a software tool called LISE++ is used [43]. The simulation is also used directly to set the FRS spectrometer during the experiment.

The LISE++ code is based on a Gaussian-convolution technique and a general polynomial on log scale to determine the overall position, angle and energy distribution of the fragment ions at the various focal planes. This code can also be used to simulate the production rate of fragments in different reactions between different primary beams and targets and predict the energy deposited by each fragment in any material.

LISE++ uses only 1^{st} order optics for its calculations and it has the convenient feature of a high simulation speed for fragments production and transmission calculations. This feature also allows to assess the total rates in the focal planes, used to not exceed detector rate capabilities at the S2 and S4 focal planes.

In the simulation program, values of target thickness and stripper thickness as well as the slit aperture values were set to fulfill the following criteria: the transmission of fragments of interest should be maximized (retaining sensitivity and selectivity). They are also set following the minimum energy constraints of certain detectors (for example the MUSICs require a minimum energy for the incoming fragment to be measured properly), as well as the fragment energy required by the AIDA to measured correctly the ions implantation [44].

The parametrisations used for LISE++ are summarised in Tab. 2.2.

Quantity	LISE++	Ref.
Energy loss and angular straggling	ATIMA 1.2	[45], [46], [47]
Momentum distribution	Goldhaber	[9]
Mean fragment velocity	Morrissey	[48]
Empirical parametrization of cross section	EPAX3	[49]
Calculation of charge states	GLOBAL	[50], [51]
Masses	AME2016	[52], [53]

Table 2.2: Parametrisations used for LISE++ simulations (adapted from Ref. [44]).

CHAPTER 3

First steps of the analysis

This section is devoted to the first step of the analysis performed on the data.
At first, this procedure consists in the calibration of the signals recorded from each detector systems, both in the FRS and DESPEC.

Similar procedures were applied for the two datasets, *Dataset1* and *Dataset2*, the former focused on neutron-rich Po-Fr ions, the latter on the ^{100}Sn region. In this section only the procedures for the former are described in details, highlighting where different steps were applied to the latter, due to the different characteristics of the two datasets.

3.1 FRS detectors

Being the FRagment Separator a complex ensemble of various kinds of detectors, the identification of the ions can be achieved only after a careful calibration of each subsystem.

3.1.1 MUSICs

As the energy deposited in the ionisation chambers has a dependence not only on the atomic number Z but also on the ions' velocity, as described in section 2.2.2, there is a need to perform a velocity calibration. The two chambers were calibrated using the primary beam (^{238}U) at well-known energies, corresponding to specific magnetic rigidities, providing five different velocities, as displayed in Tab.3.1. This is achieved by inserting a number of matter layers along the beam line.

β	dE MUSIC1 (MeV)	dE MUSIC2 (MeV)
0.867169	2675.56	2663.88
0.847235	2766.69	2760.99
0.804596	2989.58	2998.15
0.823405	2888.42	2888.83
0.781494	3124.37	3144.58

Table 3.1: Five-points calibration: evergy loss in MUSIC1 (left) and MUSIC2 (right) as a function of magnetic rigidity.

The resulting calibration points, where the energy loss measured in the MUSIC detectors is plotted as a function of β are shown in Fig. 3.1. The data points are fitted with a second-order polynomial function. This procedure allows to correct the velocity dependence of the energy loss. The atomic number is obtained by adding the absolute reference point of the Z of the primary beam as an offset.
According to the Bethe-Block formula, the energy loss has also a dependence on the

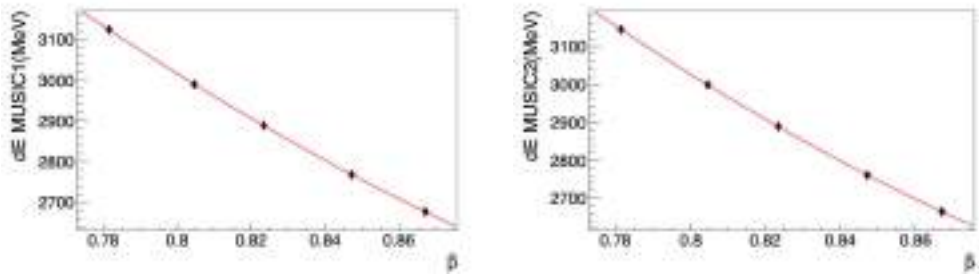

Figure 3.1: Five-points calibration: evergy loss in MUSIC1 (left) and MUSIC2 (right) as a function of magnetic rigidity.

path length inside the ionisation chamber, which can be corrected by eliminating the spatial dependence. This further correction need not be applied to *Dataset1*, as no position dependence was observed, as shown in Fig. 3.2. This correction is important when using the *wide* AIDA configuration, as in *Dataset2*.

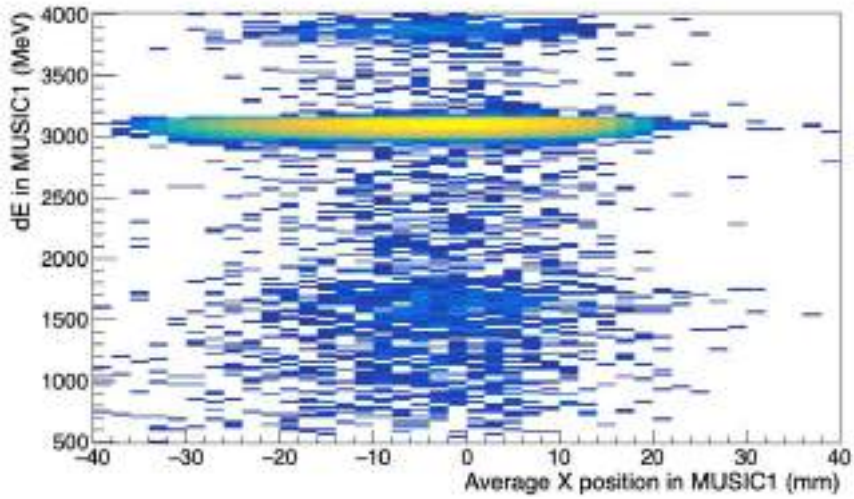

Figure 3.2: Dependence of the energy loss in MUSIC detector with respect to the x position reconstructed at S4.

As described in Sec. 2.2.2, the volume gas is not sealed, therefore the gas is subject to variations according to temperature and pressure changes, causing gain drifts in the energy loss. This effect is shown as a function of time in the left plot of Fig.3.3. This drift was corrected for the whole duration of the experiment by dividing the data in slices of approximately one hour each and aligning the distributions found in each sector.

Several tests were performed in order to obtain the optimum correction to this gain drift:

- **Offset**: for each section, the offset between the strongest Z peak and the correspondent atomic number ($Z = 89$, Ac) was calculated and the measured value was corrected by this value.

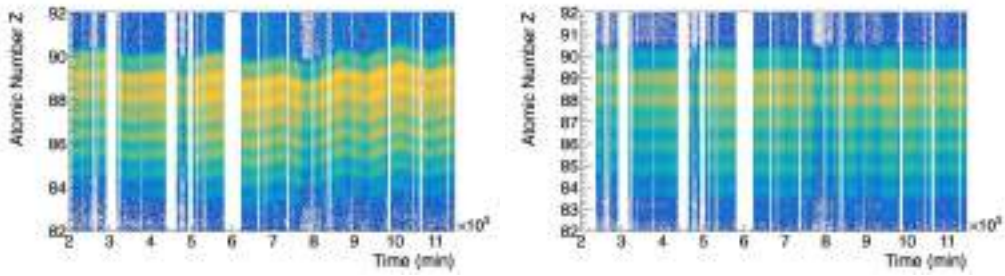

Figure 3.3: Atomic number Z from the MUSIC detectors as a function of time, before (left) and after (right) correction.

- **3 Peaks**: for each section, the centroids of the $Z = 87, 88, 89$ peaks were determined, and their distribution, as compared to their true Z value, was fitted with a linear function.

The best between these two methods was selected by comparing the Z resolution obtained in the different cases, as shown in Tab. 3.2.

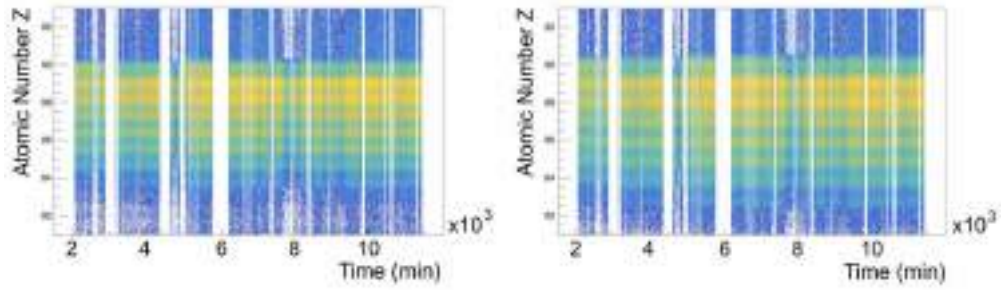

Figure 3.4: Atomic number Z from the MUSIC detectors as a function of time, after the application of the offset (left) and 3 peaks (right) correction method.

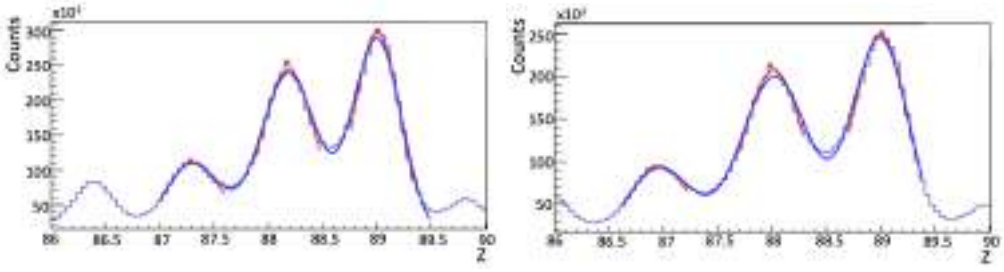

Figure 3.5: Atomic number Z from the MUSIC detectors, after the application of the offset (left) and 3 peaks (right) correction method.

Despite the highest resolution being obtained with the offset method, the 3 peaks method is the one that allows the best separation between the elements, as the peaks correspondent to different Z values are more spaced, as shown in Fig. 3.4, 3.5.

Method	Z	R
Offset	87.30444	6.5×10^{-3}
	88.18786	3.8×10^{-3}
	89.00296	2.0×10^{-3}
3 peaks	86.96721	7.8×10^{-3}
	88.02756	4.8×10^{-3}
	88.99802	3.1×10^{-3}

Table 3.2: Resolution obtained for different Z values with the offset and 3 peaks methods.

With the application of the drift correction, the Z resolution was improved by 20-35$\%$.

3.1.2 Scintillators and Time of Flight

The time of flight information can be obtained using the single left or right signals of each scintillator, or extracting the average between the two (see Sec. 2.2.2). The latter option was chosen, giving the best resolution. The comparison of the resolution obtained for SC21-SC41 or SC22-SC41 combinations are presented in Tab. 3.3, using only left-left, right-right or the average option.

	Resolution (%)		
	Left-Left	Right-Right	Average
SC21-41	0.17	0.15	0.12
SC22-41	0.14	0.15	0.09

Table 3.3: Resolution comparison for the left-left, right-right or left-right average option.

All possible options for the scintillators detectors and electronics were analysed, in order to obtain the optimal time of flight resolution, and thus the best A/Q resolution. This is described in section 2.2.2. The time of flight of the ions can be calculated using different combination of detectors at the mid and last focal planes. At the mid focal plane, called S2, two scintillators are positioned after the degrader wedge. The first one (SC21) is subject to highest radiation damages, being the first to be hit by the secondary beam in the FRS beamline. For this reason, the second scintillator (SC22) displays a better resolution and efficiency.

In *Dataset 1* the option giving the best performance was set to use SC22 at S2, which had the best efficiency, with the analog electronics, as shown in Tab.3.4 . The digital multi-hit logic was not needed, given the low rates at the mid focal plane. On the contrary, for *Dataset 2*, the multi-hit electronics was used, as the ions' rate reached very high values ($\sim 10^6$), allowing to avoid pile-up effects.

	SC21-SC41		SC22-SC41	
	TAC	MHTDC	TAC	MHTDC
ToF ($\times 10^2$ ps)	1.47344(8)	1.48066(8)	1.41479(7)	1.44328(6)
FWHM	0.1	0.1	0.08	0.1
Resolution (%)	6.8	6.5	5.9	7.8

Table 3.4: Comparison of time-of-flight resolution obtained for SC21 and SC22 at S2, using analog and digital electronics.

The calibration procedure was performed on the time of flight, shown in Fig. 3.6 and Table 3.5.

A drift was observed in the time of flight throughout the experiment, thus requiring gain-matching. As the time of flight assumes different values for specific ion species, the correction is to be done independently for each ion. Ions picking up electrons in between the middle and final focal planes of the FRS change their velocity, thus creating larger TOF peaks which are more difficult to correct. Therefore, the correction must be done gating on a specific charge state. In the following paragraphs, the correction applied for Rn isotopes is shown.

The charge states distribution for radon isotopes is shown in Fig. 3.7 and the result of the gates on the two regions on the time of flight is also reported in Fig. 3.8. The time of flight for the fully stripped ($\Delta Q = 0$) was chosen for the drift correction, as the spectrum

$1/\beta$	TOF SC21-41 (ps)	TOF SC22-41 (ps)	TOF SC21-41 MHTDC (ps)	TOF SC22-41 MHTDC (ps)
1.15	3.44×10^4	3.62×10^4	-3.31×10^1	-1.28×10^2
1.18	3.08×10^4	3.28×10^4	-2.96×10^1	-1.24×10^2
1.24	2.30×10^4	2.51×10^4	-2.17×10^1	-1.16×10^2
1.21	2.65×10^4	2.86×10^4	-2.53×10^1	-1.20×10^2
1.28	1.82×10^4	2.06×10^4	-1.68×10^1	-1.12×10^2

Table 3.5: Five-points calibration: TOF measured by SC21-41 and SC22-41 using analog electronics (first two columns) and SC21-41 and SC22-41 using digital electronics (third and fourth columns) as a function of the inverse of the magnetic rigidity.

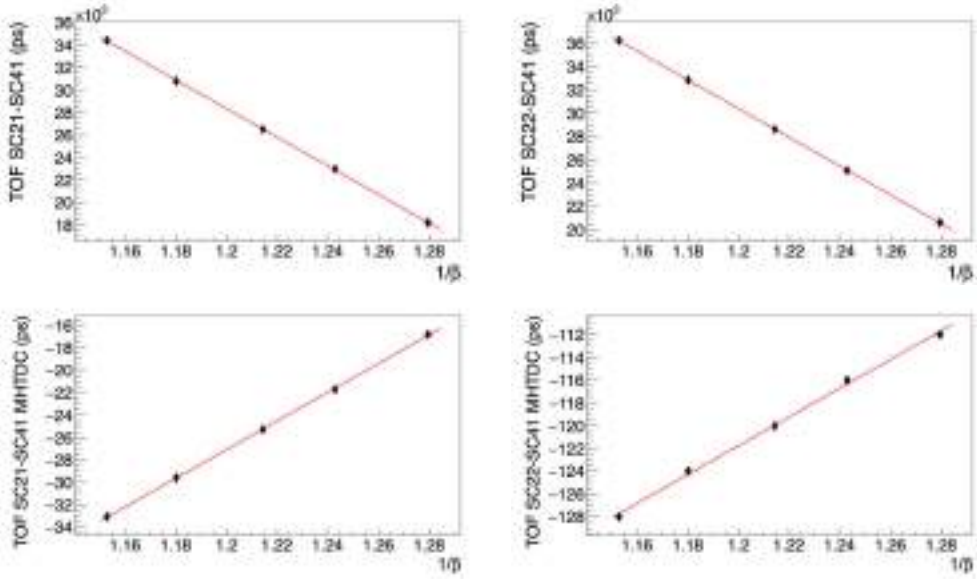

Figure 3.6: Time of Flight five-points calibration. Top row: time of flight measured in SC21-SC41 (left) and SC22-SC41 (right) with analog electronics (top) and with multi-hit digital electronics (bottom) as a function of the inverse of magnetic rigidity.

is closer to a Gaussian distribution. The result of the correction applied for fully stripped Rn isotopes is shown in Fig. 3.9.

The application of the drift correction to the time of flight has an impact on the A/Q ratio, removing the effect of drifts, as shown in Fig.3.10.

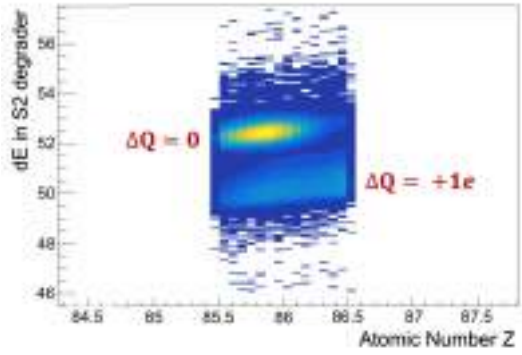

Figure 3.7: Energy loss in the S2 degrader as a function of the atomic number Z for radon isotopes

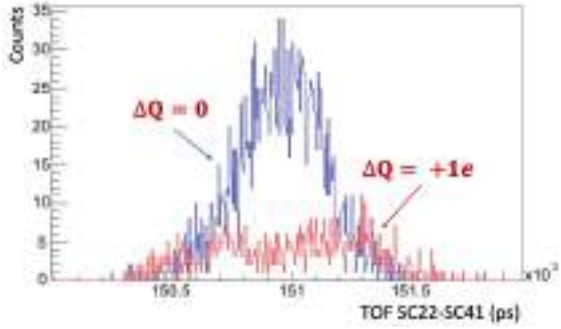

Figure 3.8: Time of flight for radon isotopes in a time window of $\sim$ 1 hour for fully stripped ($\Delta Q = 0$) in blue and hydrogen-like ($\Delta Q = 1$) ions in red.

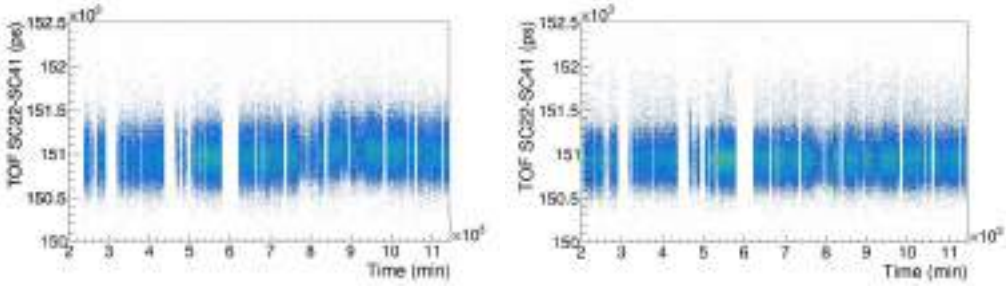

Figure 3.9: Time-of-Flight from SC22-SC41 detectors as a function of time for Rn isotopes, before (left) and after (right) correction.

3.1.3 X Position at S2

The X and Y position of the ions can be calculated using several detectors at the mid and final focal planes. The best position resolution is given by the TPC detectors, whose functioning principle is explained in Sec. 2.2.2. The scintillators, instead, are characterised by a better efficiency associated to a poorer position resolution.

Fig. 3.11 displays the X position at S2 and S4 as measured from the time projection

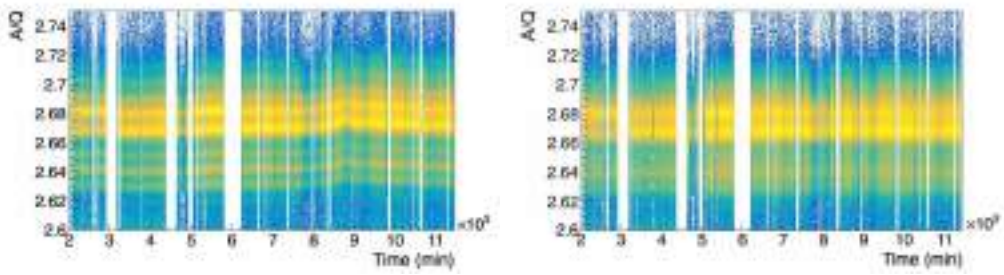

Figure 3.10: A/Q ratio as a function of time, before (left) and after (right) correction.

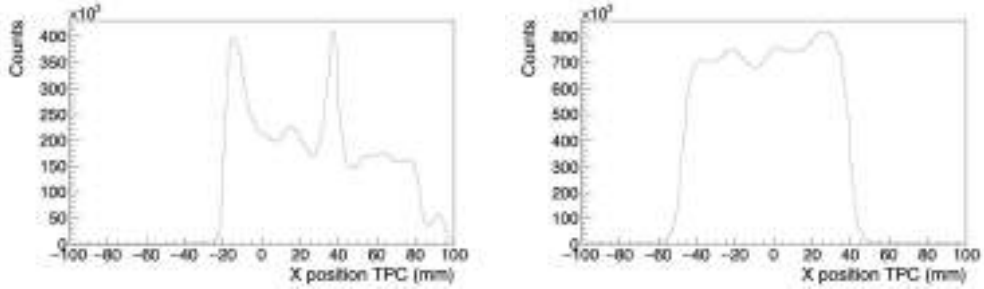

Figure 3.11: X position at S2 (left) and S4 (right) measured by the TPC detectors

chambers. The spectra display a structure containing several peaks. This is caused by the overlapping distributions of several ion species, which develop different trajectories inside the FRS and are produced with different intensities. There is a sharp cut for positions $X \leq -20$ caused by the presence of slits, to reject strong contaminants. In Fig. 3.12, the X position obtained from scintillator 21, 22 and 41 is plotted, as well as the TPC position as a function of position in the scintillator. This was used to perform position calibration for SC21 and SC22 using TPC position as a reference by fitting the distribution in the right panel of Fig. 3.12, with a fifth order polynomial function. All the three scintillators show an inefficiency effect in the central part due to radiation damage. This effect is more evident in the SC21 scintillator.

In order to select which reference would optimise the separation of our ions of interest, a plot of the A/Q ratio obtained using the different detectors is shown in Fig. 3.13. In all the three cases, the time of flight was measured using the SC22-SC41 combination with analog electronics, as explained in Sec. 2.2.2, and the position at S4 was extracted using the TPC detectors.

The relative efficiency obtained with the three detectors, using SC22 as a reference, being the detector with the highest efficiency value, is listed in Tab. 3.6.

The left panel of Fig. 3.13 shows the overall A/Q distribution from all nuclei produced in the reaction, the left part of the spectrum being dominated by fission fragments, which are not easily resolved. The peaks at the right are highlighted in the right panel, where one can see that only TPC detectors can resolve the individual components, while A/Q calculated using X positions extracted from the scintillators do not have enough resolving power to distinguish peaks. The A/Q ratio efficiency obtained using the TPC detectors corresponds to approximately 70% of the one observed using the scintillators at S2. The

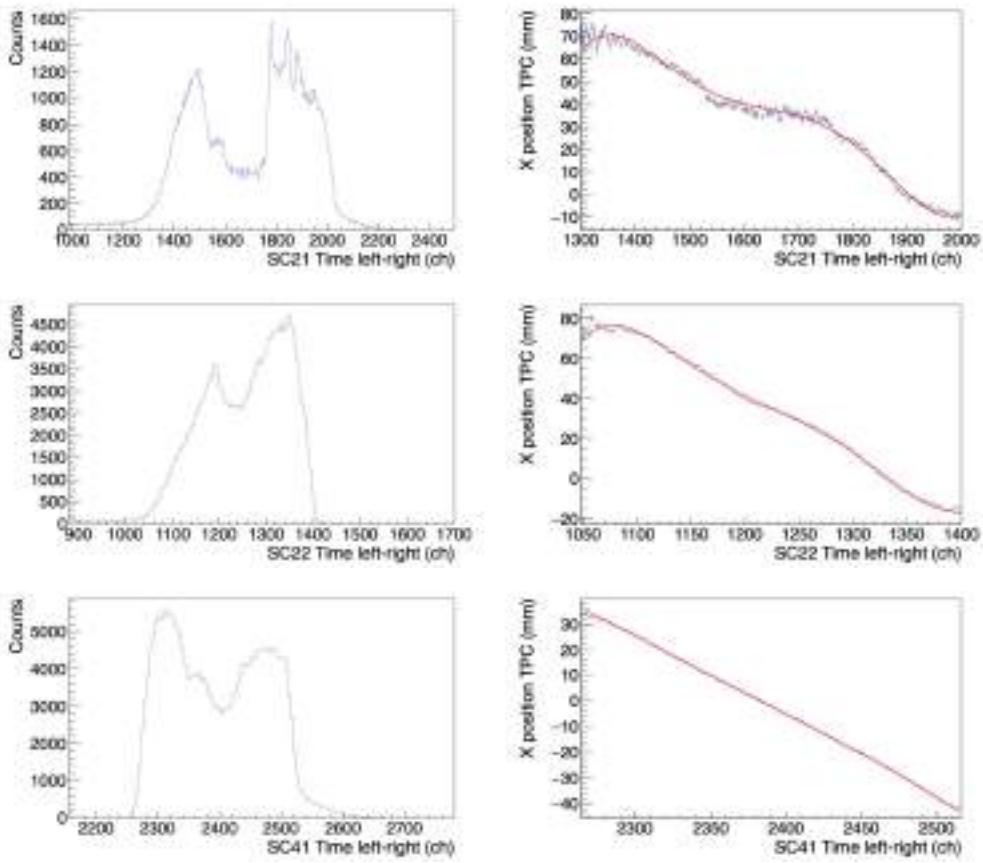

Figure 3.12: X position at S2 measured by SC21 (top-left) as a function of X position at S2 measured by the TPC (top-right), by SC22 (middle-left and middle-right), and by SC41 (bottom-left and bottom-right)

.

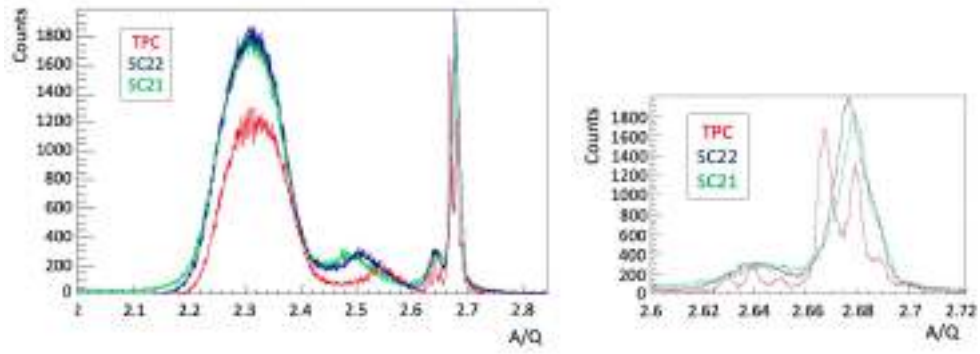

Figure 3.13: Comparison of A/Q spectra obtained from position measurement from SC22, SC21 and TPC, zoomed on the heavy region ($Z > 70$) (right panel).

Detector	Relative A/Q efficiency (%)
SC22	100
SC21	96.5
TPC	68.3

Table 3.6: Comparison of A/Q efficiency with position measurement obtained from SC22, SC21 and TPC, relative to SC22.

position resolution of the TPCs allows to obtain an A/Q separation of the different ions, while the resolution is so poor for the scintillators that we are not able to distinguish between different isotopes of the same element. Therefore, for this experiment, TPC detectors were chosen for the position measurement at S2.

3.2 AIDA

As explained in Sec. 2.3.1, the AIDA detector is a stack of DSSDs with two readout systems, a low gain branch, used for the high-energy implantation events, and the high gain one, used for low-energy decay events. The two readout systems work independently and generate two separate data streams.

Each AIDA event, after being unpacked, is characterised by:

- Event number
- DSSD layer number, (1 is upstream, 3 is downstream)
- Strip X,Y
- Position X,Y in mm, where (0,0) is the centre of the DSSD
- Energy (MeV for implants, keV for decays)
- Energy from front (X), and back (Y) strips
- Cluster size X,Y
- Time (10 ns precision for implants, 2 μs for decays)
- Time from front (X), and back (Y) strips
- Fast time (10 ns precision for implants and decays)
- Stopped (if the implant is stopped in the considered DSSD)

Typical energy spectra obtained from the implant and decay branches are shown in Fig. 3.14 (left and right panels respectively). Implanted ions deposit energy in the GeV range, while decay events span between few keV to tens of MeV. The decay branch detects all sorts of low energy charged particles such as α and β particles, protons and light ions, that generate different energy and position distributions.

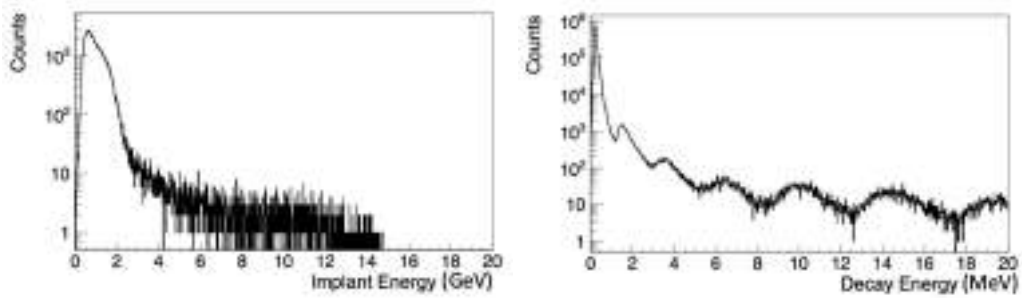

Figure 3.14: Energy spectra from the implant (left) and decay (right) branch

During the experimental campaign in 2021, AIDA was characterised by an unusually high background level that was generating many spurious events. In order to overcome this, a few conditions are set on the raw data.

First of all, a time condition requiring that, for the same event, the front (X) and back (Y) strip are collected at the same time. This is done for both the implantation and

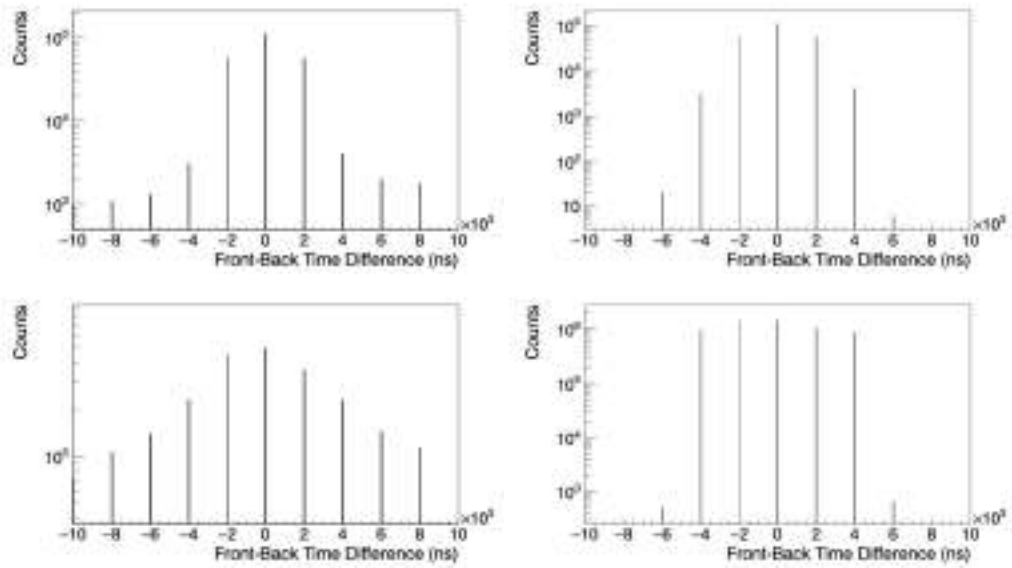

Figure 3.15: Implantation (top) and decay (bottom): time difference between the front (X) and back (Y) strips, before (left panel) and after (right panel) the condition

decay branch (Fig. 3.15). The condition includes events showing a time difference within ± 4000 ns, to consider the uncoupling of the AIDA multiplexer or clock rounding issues.

Secondly, for decay events, an energy condition is also applied on the front and back energies, taking into account only events in which the energy difference between front and back is approximately the same. In particular, we consider a range of ± 350 keV. As shown in Fig. 3.16, in fact, we observe a strong component of events registered by X or Y strips only, that are caused by background noise. A different behaviour is registered for implant events where we see that events mainly lie on the diagonal.

Finally, a multiplicity condition is set, disregarding all the events where a single strip is firing more than once and is therefore considered a noisy strip.

The result of this last condition is shown in Fig. 3.16 in the right panels. In particular, for the decay events, the number of events on the diagonal line increases after applying the conditions because more events survive the multiplicity cut.

While ions deposit their high energy in one single pixel, β particles instead deposit their energy in multiple adjacent pixels. This happens because the range of a β electron in silicon is generally larger than the strip pitch of the detector. For example, a 1 MeV electron has a range of ~ 2.3 mm in silicon. Therefore, adjacent strips that fire in the same event window are summed together to form a cluster. This effect is visible in the plots at Fig. 3.17: β decay events generally form clusters that comprise a larger number of adjacent pixels (right panel) than ions (left panel), for which the cluster size is confined to 2. Approximately 85% of decay events produce clusters of a single pixel, while a small fraction consists of 2-pixels clusters.

The β intensity and the energy deposited in 1 mm silicon, i.e. an AIDA layer and 2 pixels, was calculated for the specific case of β decay from ^{227}Rn to ^{227}Fr. The result is shown in Fig. 3.18, where lower energy β tend to deposit a higher fraction of their energy in the first pixel they encounter.

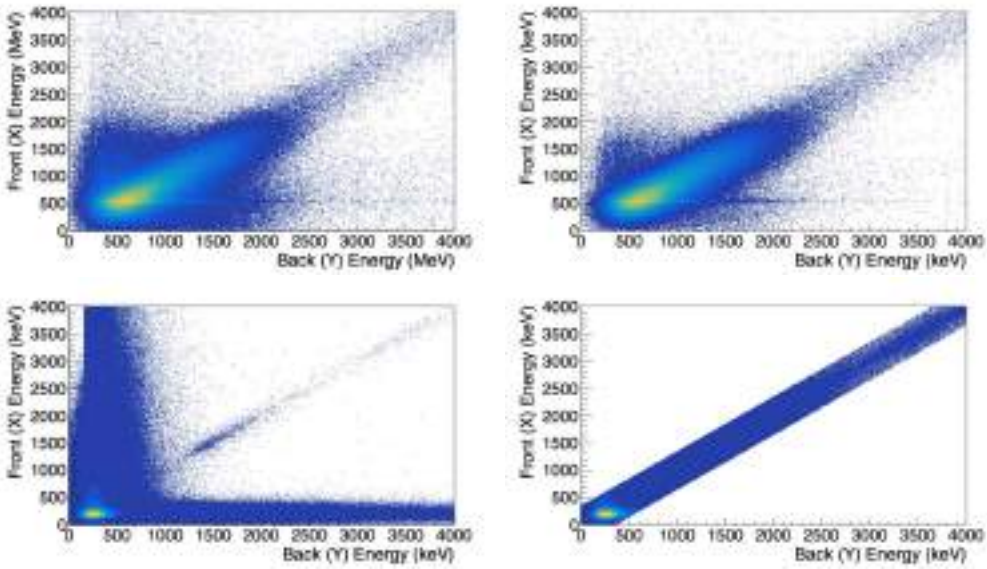

Figure 3.16: Implantation (top) and decay (bottom): front (X) energy versus back (Y) energy before (left panel) and after (right panel) the application of the aforementioned conditions

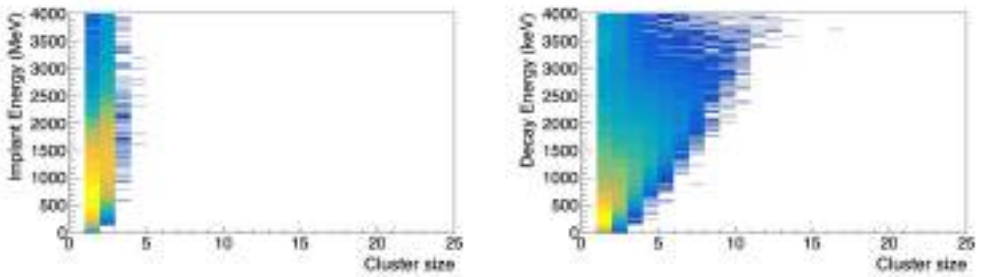

Figure 3.17: Cluster generated by an implantation (left panel) and decay (right panel) event.

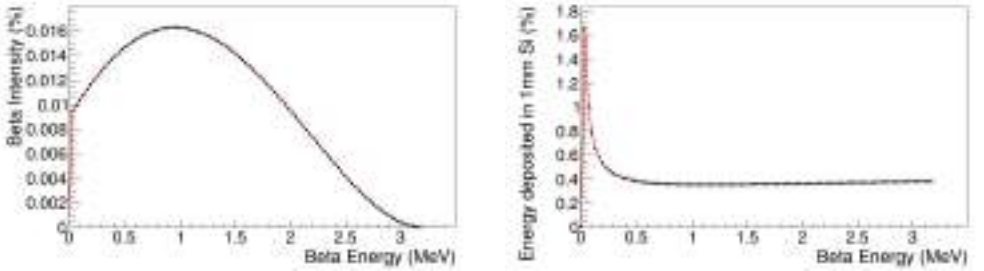

Figure 3.18: β intensity function (left panel) and the energy deposited in 1 mm silicon for that energy (right panel) for ^{227}Rn

Due to the high degree of pixellation level of the AIDA detector, additional sources of background were studied and taken into account to study decay events.

First of all, it's been observed that high multiplicity events in the high-gain branch were detected in the first tenths of milliseconds following the implantation of an ion, as shown in Fig. 3.19. This was caused by the mechanical shock generated by the incoming highly-energetic ion that starts the decay branch on the pixels surrounding the ion pixel, combined with the activation of surrounding pixels in the decay branch due to charge pick-up. In order to overcome this, the β events occurring in the first ~ 100 ms after the implantation were neglected. This value was optimised to account for the different response of each AIDA detector.

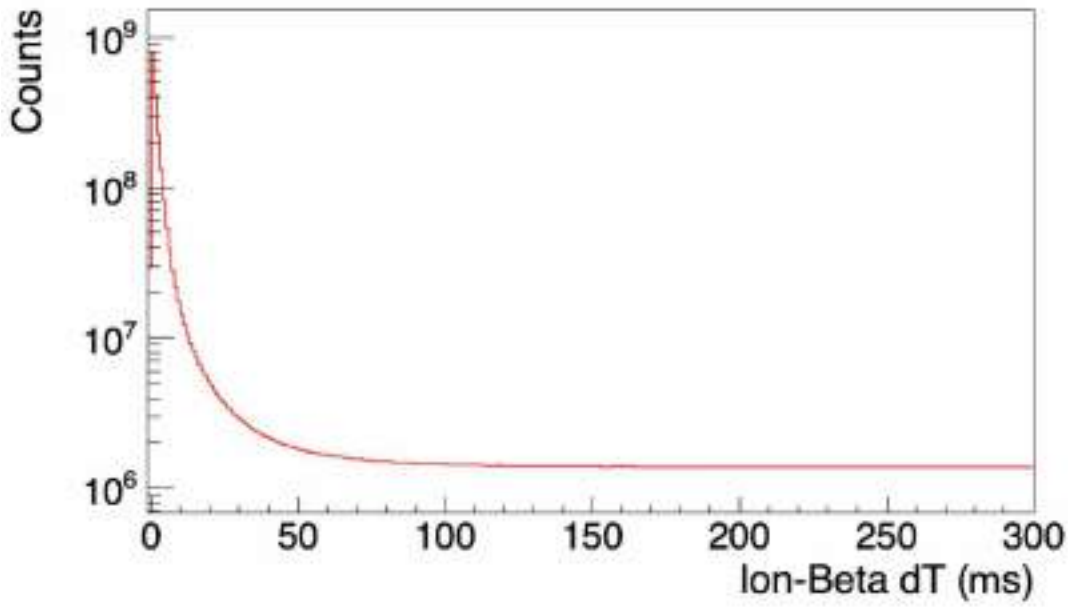

Figure 3.19: β -ion time difference spectrum in the first microseconds after the implantation. High multiplicity events are detected in the high-gain (decay) branch.

3.3 βPlastic

The working principles of the βplastic detector are explained in Sec. 2.3.2. The energy information is conveyed by the βPlastic electronics in the form of a time over threshold spectrum, with a logarithmic dependence on the energy [38]. The time over threshold (ToT) spectrum for one of the channels of βPlastic is shown in the left panel of Fig. 3.20.

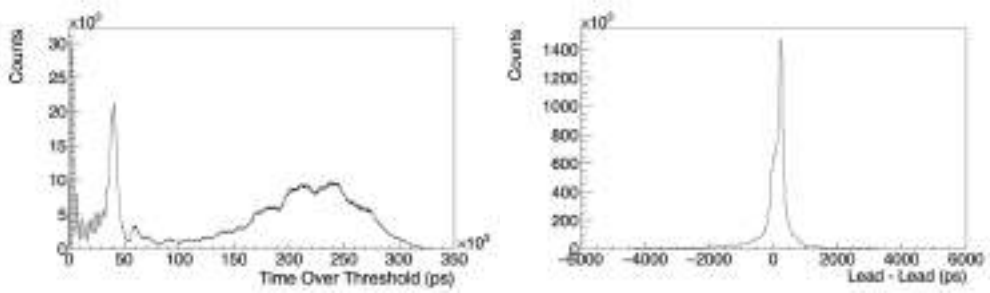

Figure 3.20: Time over threshold spectrum for one channel (left panel) and lead-lead (timing) spectrum from two channels (right panel) of the βPlastic detector

The timing information instead can be extracted as the difference between the leading edge of the signals of two different βPlastic channels. A typical time (lead-lead) spectrum is shown in the right panel of Fig. 3.20.

The time over threshold spectrum from βPlastic is difficult to understand, owing to the logarithmic dependence on the energy. In addition these detectors can be triggered by several particles, such as high-energy γ rays, β electrons, α particles, light and heavy nuclei.

In order to disentangle the main contributions to the βPlastic ToT spectrum, we have set different conditions, producing the spectra shown in Fig. 3.21. The black spectrum is derived requiring a coincidence with FRS events (i.e. a signal from scintillator 41), and is therefore reporting mainly the response to heavy ions, showing, in fact, saturated signals above 100×10^3 ps. The red spectrum is, instead, associated to off spill events (i.e. the pause between two spills from SIS18), which is therefore formed by β and γ contributions only. The signals produced by β particles are therefore highlighted in the region above 50×10^3 ps. The nature of the peak around 30×10^3 ps will be discussed in more details in section 4.3.

Due to the multiple contributions, the complexity of the spectrum,and the peculiar response of each channel, the time over threshold spectra could not be calibrated.

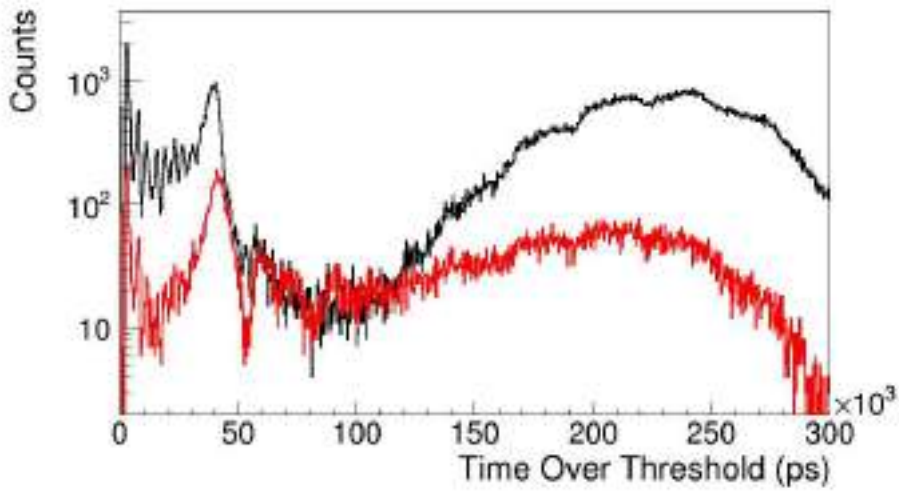

Figure 3.21: Time over threshold spectrum associated to off-spill events (red) and to heavy ion (black).

3.4 γ detection array

γ -ray detectors need to be calibrated to convey the correct time and energy information. The FATIMA and HPGe arrays both suffer from gain-drifts that needed to be corrected in order to improve the energy and time resolution. The same procedure was performed for both detector systems.

3.4.1 Calibration

Energy calibration was performed using a ^{152}Eu source, in an energy range between 121-1408 keV, whose result is shown in Fig 3.22. For each crystal the strongest ^{152}Eu peaks were fitted in the raw spectrum, and a 3^{rd} order polynomial fit made to convert into energy. The calibration coefficients applied for the FATIMA and HPGe array are listed in App. B.

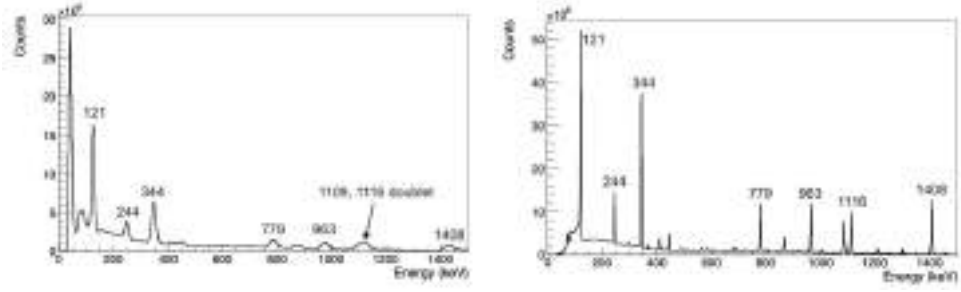

Figure 3.22: Energy spectrum measured from FATIMA (left panel) and germanium (right panel) for a ^{152}Eu source, after calibration.

Time-alignment was performed using a ^{60}Co source. The procedure consists in aligning time differences between all detectors with respect to a reference one. A drift in the time difference between detectors read by different TDC modules was observed and corrected, as shown in Fig. 3.23.

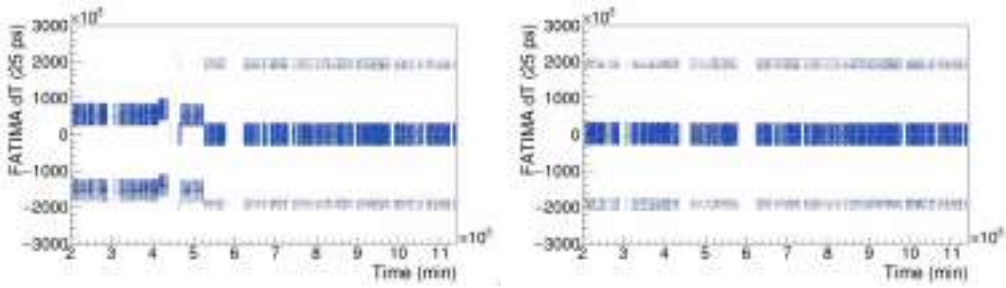

Figure 3.23: FATIMA time difference between two detectors as a function of time, before (left) and after (right) correction.

3.4.2 Gain-matching

A gain-drift was observed in FATIMA detectors energy spectra, caused by the temperature variations and the prolonged high rate exposure. This was corrected individually for each detector. An example of the correction is shown in Fig. 3.24.

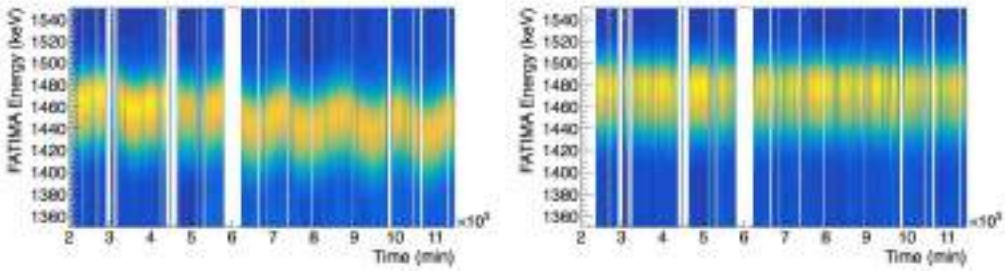

Figure 3.24: FATIMA detector energy as a function of time, before (left) and after (right) correction.

The germanium detectors were also showing a gain-drift during the experiment, but this effect was less evident, thanks to the baseline compensation performed by the FEBEX digital boards. Nevertheless, the gain-drifts were corrected in germanium detector for which the drift in time was more marked. An example is shown in Fig. 3.25.

3.4.3 Addback

The closed-packed configuration of the HPGe detectors used in the two experiments allows to improve the signal-to-background ratio and the photopeak efficiency by means of the application of the add-back algorithm.

When a γ ray reaches the detector material, it can undergo three different processes, depending on its energy: photoelectric effect, Compton scattering and e^- - e^+ pair production. In the energy range of the typical γ rays of our interest, the most probable interaction is via Compton scattering.

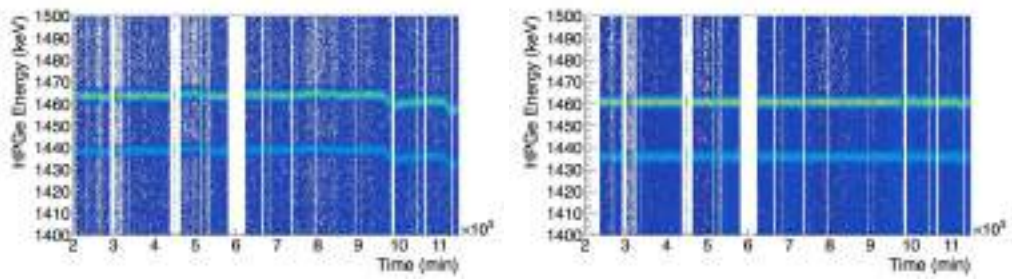

Figure 3.25: Germanium detector energy as a function of time, before (left) and after (right) correction.

When a γ ray interacts with a detector through Compton scattering, it does not deposit its whole energy in one single interaction. A second interaction can occur in another crystal close to the first one. In a cluster configuration, the energy released in adjacent capsules can then be added-up, to reconstruct the real energy of the incident γ ray. The reconstructed energy of the event will be the sum of the energy deposited by the γ ray in the adjacent segments $E_\gamma = E_{\gamma 1} + E_{\gamma 2} + E_{\gamma 3}$, while the time will be the one recorded by the first, more energetic, interaction.

A few conditions need to be fulfilled by the sub-events for the algorithm to be applied. First of all, the γ -ray energy needs to be higher than a certain threshold (40 keV) and all the sub-events need to be registered within a time-window of 100 ns. Moreover, the sub-events must be registered in neighbouring crystals, of the same or neighbouring cluster, as shown in Fig.3.26.

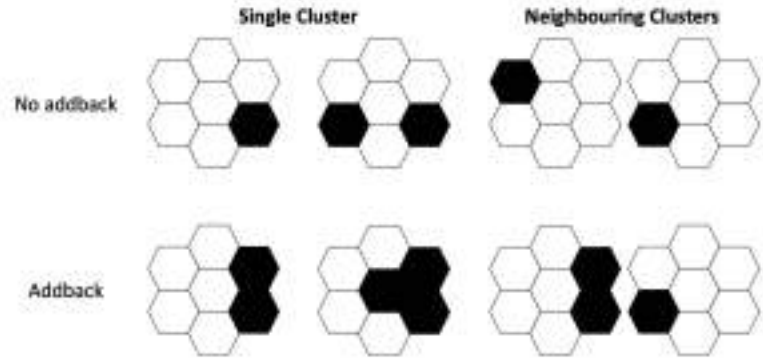

Figure 3.26: Addback procedure for single (first two columns) and neighbouring (third column) clusters

The result of the application of the add-back procedure is shown in Fig. 3.27. One can note a reduction of the Compton background at low energies, together with an increase of counts in the peaks at high energies.

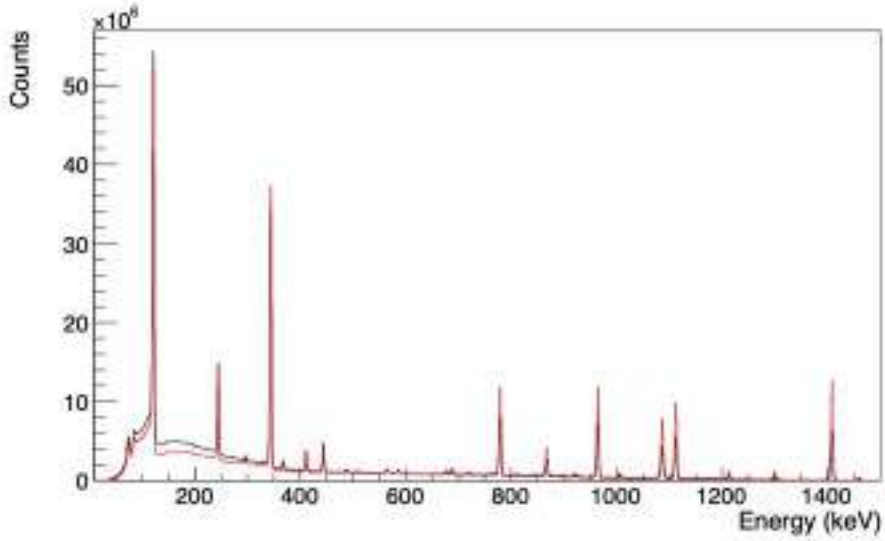

Figure 3.27: Comparison of the energy spectrum obtained measuring a ^{152}Eu source, without (black) and with (red) addback.

3.4.4 Resolution

The characterisation of the array efficiency plays an essential role in the reconstruction of nuclear level schemes from β decay or after isomeric deexcitations. A ^{152}Eu source with an activity of 370 kBq was employed in the measurement, placed in a central position on the AIDA detectors.

The resolution is calculated as follows:

$$R = \frac{FWHM}{E}, \tag{3.1}$$

where the $FWHM$ is the Full Width Half Maximum of the photopeak and E is the centroid of the peak.

A value for the resolution was calculated for each energy peak considered for the energy calibration. The result is shown in Fig. 3.28, where the resolution points for the FATIMA array are presented in the plot on the left panel and for the germanium array on the right panel.

3.4.5 Efficiency

The ^{152}Eu source data was employed for the extraction of the efficiency for the germanium and $LaBr_3$(Ce) array.

The absolute efficiency for each data point is calculated as:

$$\epsilon = \frac{A_\gamma}{T_{acq} \cdot A \cdot I_\gamma} \tag{3.2}$$

where A_γ is the peak area, N_{acq} is the total number of events acquired, T_{acq} is the acquisition time, A the activity of the source and I_γ the absolute intensity of the transition considered.

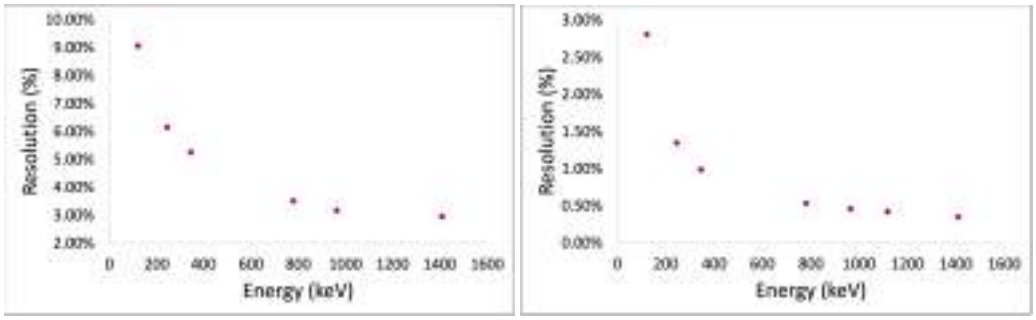

Figure 3.28: Resolution obtained for the FATIMA (left panel) and germanium (right panel) arrays.

The function used to fit the efficiency curve is taken from Ref. [54]:

$$\epsilon = exp[(A + Bx + Cx^2)^{-G} + (D + Ey + Fy^2)^{-G}]^{-1/G} \tag{3.3}$$

where $x = \ln E_\gamma/100$ keV and $y = \ln E_\gamma/1000$ keV. The coefficients A, B and C describe the efficiency at low energies ($E_\gamma < 100$ keV), D, E and F at high energies ($E_\gamma > 100$ keV), and G is an interaction parameter between the two regions defining the sharpness of the turnover region.

Being the activity of the used source too high for our electronics, it gave rise to pile-up effects, thus lowering the measured efficiency.

The efficiency of germanium detectors was calculated after the application of the add-back procedure, considering in-beam data from *Dataset*2. Here, a known γ-ray cascade from ^{98}Cd populated in the decay of an isomeric level was used to extract the γ intensity using the FATIMA data, re-scaling by its efficiency (Fig. 3.29. Once the γ intensity of the transitions was determined, the γ efficiency of germanium detectors was calculated with the inverse procedure.

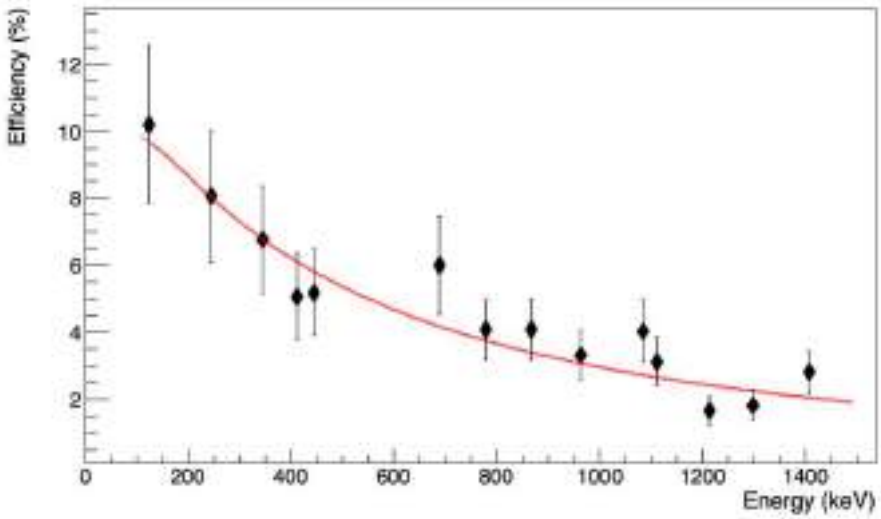

Figure 3.29: Absolute efficiency curve measured for the FATIMA array, rescaled using the value provided in Ref. [39]

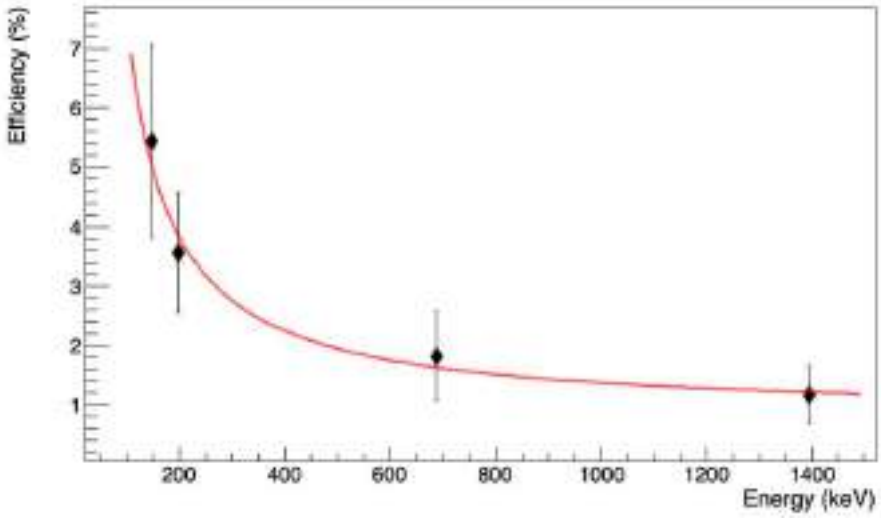

Figure 3.30: Absolute efficiency curve measured for the Germanium array. The curve is fitted to Eq.3.3.

CHAPTER 4

Analysis

4.1 PID plot reconstruction and optimisation

After the calibrations and drift corrections, the identification data from the FRS spectrometer needed further adjustments in order to optimise the identification plot, and ensure, therefore, the best selection of the ions of interest.

As explained in Chap. 2, the A/Q value has a dependence on the ions' Bρ and velocity (β):

$$\frac{A}{Q} = \frac{B\rho}{\beta\gamma}. \tag{4.1}$$

The magnetic rigidity itself depends on the ions position. For example, the magnetic rigidity of an ion at S4 is calculated as follows:

$$B\rho_4 = (B\rho_0)_4 \left(1 + \frac{x_4 - Mx_2}{D_4}\right), \tag{4.2}$$

where $(B\rho_0)_4$ is the magnetic rigidity of the central trajectory (known from the magnets settings), x_2 and x_4 are the ions' position at the middle and final focal planes, D_4 and M are the FRS dispersion and magnification parameters, respectively.
Moreover, the ions' velocity has a dependence on their time of flight:

$$\beta = \frac{\rho}{TOF_{(SC41-SC21)}}, \tag{4.3}$$

where ρ is the ions' path between S2 and S4.
As a result, the refinement of all these quantities contribute to an optimisation of the A/Q value obtained.

4.1.1 Angle Correction

The ions' trajectory is defined by their $B\rho$ value, which has a dependence on their A/Q ratio. Therefore, nuclei with the same A/Q ratio should follow the same trajectory and impinge on the TPC detectors with equal angles. However, aberrations of the beam optics and the finite resolution of the detectors can cause angular dispersion of the order of 10 mrad, due to the deterioration of the image. In order to correct for this effect, we have plotted the angle at S2 and S4 as a function of the A/Q ratio. It is important to note that this correction must be done for a specific ion species, in our case we selected radon isotopes (Z=86), as otherwise the plot would display a number of overlapping A/Q distributions.

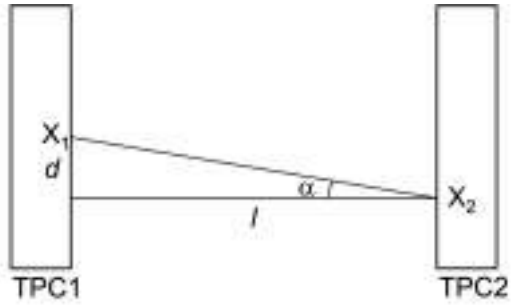

Figure 4.1: Schematic of the angle α between two x positions (X_1 and X_2) in two TPC detectors

As displayed in Fig. 4.1, the angle is defined here as the ratio between the distance d between the positions (X_1 and X_2) in the two TPCs and the distance l between the two detectors, in the small-angles approximation.

The angle distribution as a function of A/Q, as displayed in Fig. 4.3, 4.4, was divided in 10 vertical sections of 0.8 mrad each in order to ensure sufficient statistics for each portion. Every section was projected on the A/Q axis and the peak position of the strongest contribution was determined with a fit with multiple gaussian distributions. The peak position was plotted as a function of the angle (the bin center for each of the 10 angular sections) and fitted with a linear function, as displayed in Fig. 4.2.

	m	q
S2	$1.2793(15) \times 10^{-3}$	$2.63927(6)$
S4	$1.462(2) \times 10^{-3}$	$2.63641(8)$

Table 4.1: Slope and intercept resulting from the fit displayed in Fig. 4.2

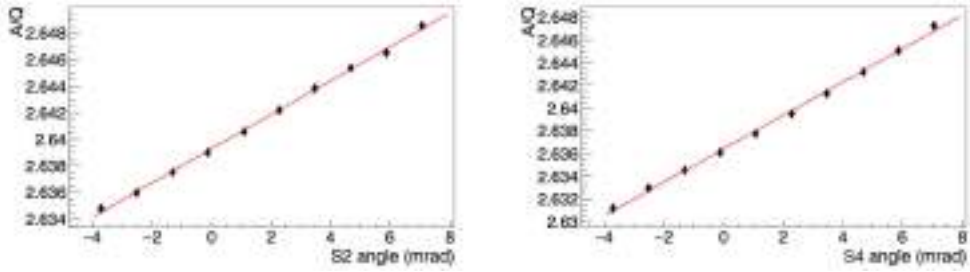

Figure 4.2: A/Q as a function of the S2 (left) and S4 (right) angle

In Tab. 4.1 the fit results for the angles at S2 and S4 are listed.

The application of the aforementioned corrections results in vertical distributions, where the dependence of A/Q on the angle is removed, as shown in Fig. 4.3, 4.4, on the right panels. Note that the intercept was not included in the correction, as it is not relevant in our case.

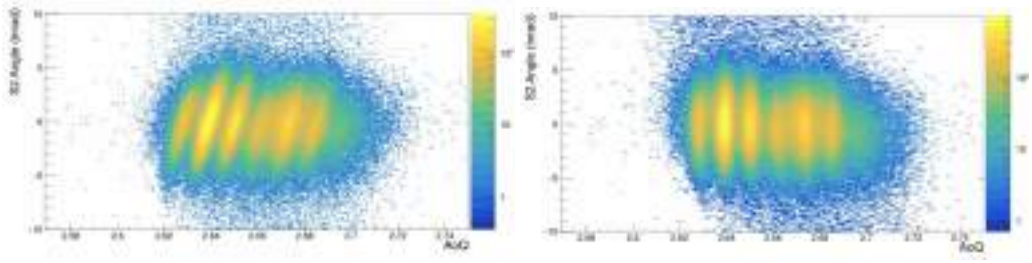

Figure 4.3: Angle at S2 before (left) and after (right) correction

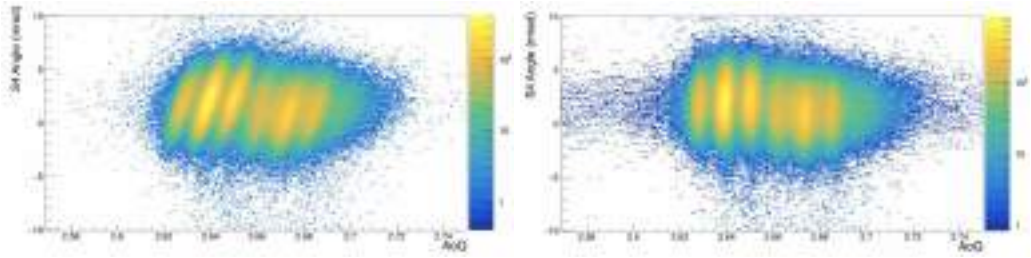

Figure 4.4: Angle at S4 before (left) and after (right) correction

4.1.2 Final ID plot

After the gain drift corrections shown in Sec. 3.1 and the angle corrections shown in Sec. 4.1, the separation between different elements and isotopes was optimised. In Fig. 4.5, the Z2 versus Z1 plot, obtained after the calibrations and drift corrections of the two MUSIC detectors is reported. L-shaped distributions suggest that a fraction of the ions has changed charge state between MUSIC1 and MUSIC2.

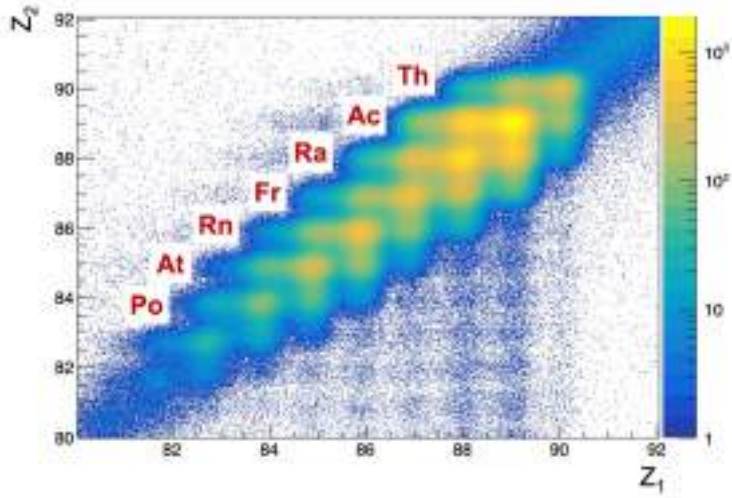

Figure 4.5: Final Z2 versus Z1 plot, the identified elements are highlighted with labels.

Fig. 4.6 shows the A/Q ratio for radon isotopes, before and after the drift corrections described in Chap. 3 and angle corrections applied. The improvement in resolution for the A/Q ratio is of approximately 30%.
Fig. 4.7 shows the identification plot of the atomic number Z versus the A/Q ratio before and after the calibrations and corrections mentioned in Chapters 3, Ch. 4. The separation of the *loci* corresponding to each nucleus is improved, and therefore a good resolution in both Z and A/Q is achieved. Nevertheless, some overlapping between *blobs* is still present. In particular for low values of A/Q, the distributions do not sit onto straight vertical lines, pointing to the presence of different charge states and/or to the necessity of a further correction of the spectra.

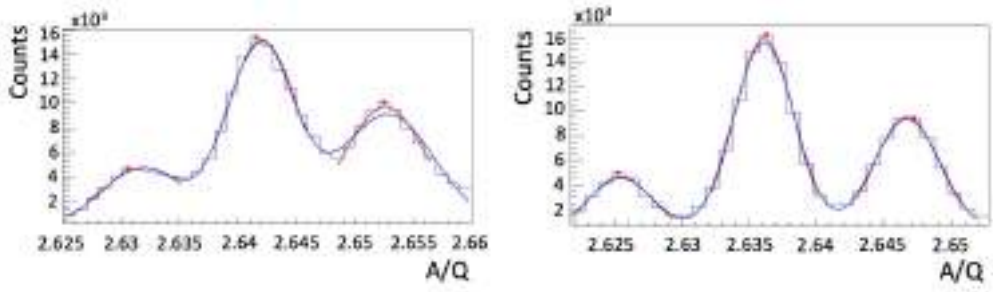

Figure 4.6: A/Q ratio of radon isotopes (Z=86) before (left) and after the corrections (right).

The same procedure was applied for *Dataset2*, and the final identification plot is shown in Fig. 4.8. The populated nuclei are highlighted with labels. Also this case, a good separation in Z and A/Q was achieved. Nevertheless, for low-Z ions, an overlapping structure is visible, which will be object of further investigation in the future.

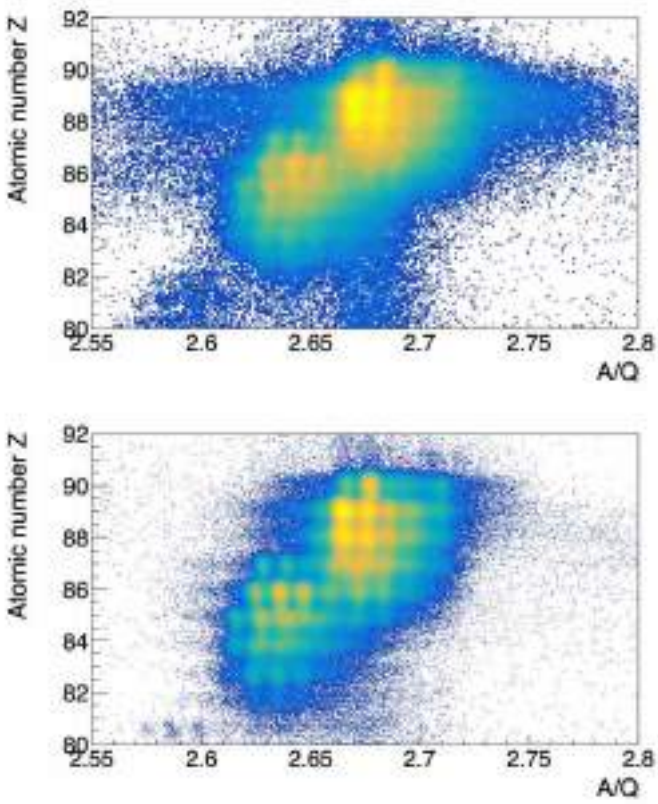

Figure 4.7: Identification plot of atomic number Z as a function of the A/Q ratio before (up) and after the corrections (bottom).

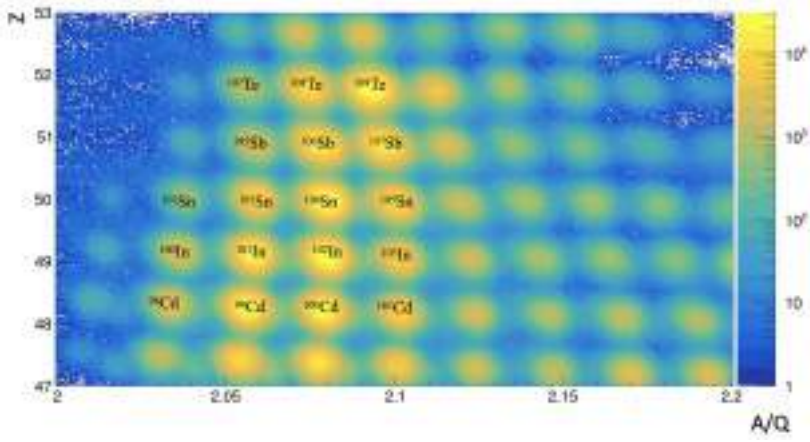

Figure 4.8: Identification plot of atomic number Z as a function of the A/Q ratio for *Dataset2*.

4.2 S4 degrader thickness calibration

The thickness of the final degrader at S4 is optimised in order to implant the species of interest in the AIDA detectors. This is tested beforehand with LISE++ simulations, and is one of the initial steps of the experimental run, providing millimetric precision.

The calibration is performed using a low intensity primary beam and varying the degrader thickness. The ratio between the rate measured in the different AIDA layers and in SC41, which is the last scintillator placed before the degrader, is measured for the different thicknesses, see Fig. 4.9. Blue points display the calibration data for DSSD1, orange for DSSD2 and yellow for DSSD3. The fit result is shown with continuous lines with the same colours. The fitting function used here was a *complementary error function*, as it displays a similar behavior to the data points. The curve poorly represents DSSD3 data points, as the ratio value of 3 was never reached in the calibration procedure, as this corresponds to smaller degrader thicknesses. Due to the high contribution of fission, the rate in the DSSDs was higher than expected, therefore it was not easy to define the proper thickness value. It is to note that this is a rough calibration performed quickly due to lack of time.

The distributions show a drop when the degrader thickness is increased, as the ions which pass through the degrader decrease in number, to the point that no ions are transmitted anymore. The optimised degrader thickness corresponds to the value at which the ratio between the number of counts in AIDA and in SC41 (before the degrader) is approximately equal to one, i.e. the largest fraction of ions is being implanted in the stack of DSSD. This procedure allows also to assess if the measured degrader thickness corresponds to the one obtained in the LISE++ calculations and, if they differ, an offset is applied in the final FRS settings.

During the *Dataset1* experiment, the background level in AIDA was of approximately $dE \sim 1$ GeV, which made the calibration procedure more difficult than usual. The calculated degrader offset was of ~ 165 mg/cm^2.

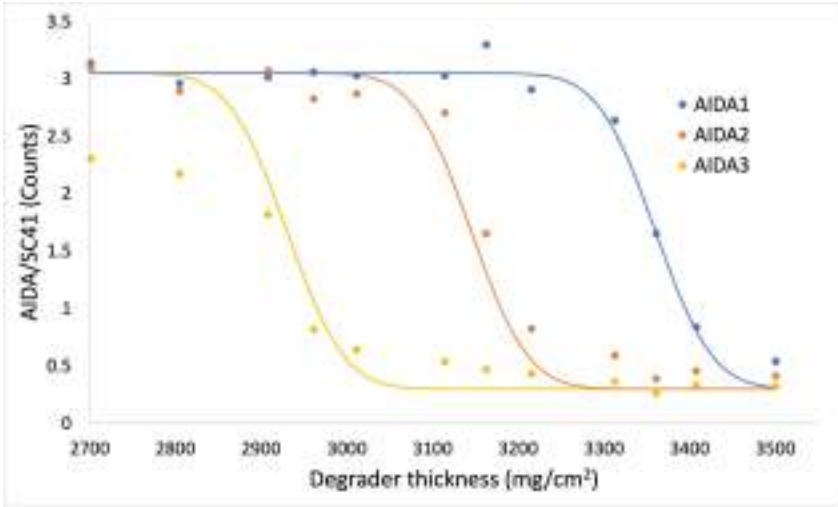

Figure 4.9: Calibration points for the degrader thickness for the three AIDA detectors (blue for DSSD1, orange for DSSD2 and yellow for DSSD3). The fitted curves are displayed as continuous lines of the same color.

4.3 Secondary Reactions in the S4 Degrader

The radioactive beam exiting the fragment separator is slowed down in the thick alluminium degrader as shown in Fig. 4.10 in order to optimise the implantation of the ions of interest in the active stopper. A scintillator (SC42) is placed right after the degrader, in order to account for secondary reactions. The incoming ions can undergo secondary reactions in the degrader material which generate lighter products, not implanted in the DSSD, but rather punching through. The reaction products will have a lower atomic number as compared to their parents, but they will be assigned to the parents' Z value as the identification is performed at an earlier stage. Fig. 4.11 shows the ions atomic number Z versus the energy loss in the degrader. The ions of interest will deposit a larger fraction of their energy in the scintillator, while the lighter, newly produced, ions will deposit a smaller fraction. As shown in the figure, the ions of interest and their reaction products generate distributions in different energy regions, creating horizontal lines extending towards the left of the graph. *Cut0* in Fig. 4.11 is associated to secondary reaction products, while *Cut1* corresponds to the incoming ions that do not react in the degrader. In *Cut1* additional regions corresponding to different charge states of the ions can be observed.

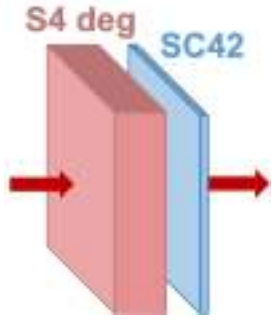

Figure 4.10: S4 degrdader and SC42 scintillator setup at the end of the FRS.

Fig. 4.12 shows the positions in an AIDA layer of Rn isotopes when imposing the additional condition of *Cut0* (left) and *Cut1* (right). As one can see, the ions belonging to the first condition show a defocused distribution, while the ones coming from *Cut1* are concentrated in a specific region of the DSSD, as expected for nuclei focused by the magnetic spectrometer. This is an additional proof that *Cut0* conditions selects ions which reacted in the degrader, while unreacted ions belong to *Cut1*.

The distribution measured by the βplastic detector also support the interpretation. The plot in Fig. 4.13 shows the hit pattern for the βPlastic detector associated to *Cut0* (red) and *Cut1* (black). Ions belonging to the *Cut0* condition, show an uniform pattern distribution in the two βPlastic detectors, corresponding to particles transversing both layers (punch through), while ions belonging to *Cut1* mainly release their energy in the upstream detector (channel 16-32), hardly reaching the downstream one (channels 0-15). This means that heavy ions are passing through the upstream βPlastic and implanting in AIDA, without reaching the downstream βPlastic detector.

The ToT spectrum, reported in Fig. 4.14 also shows the same behaviour. *Cut1* gives rise to the spectrum in red, with a wide peak in correspondence of the high energy region, while *Cut0* shows strong peaks in the low energy region and a smaller contribution in the higher energy part, again confirming the assumption of particles releasing small energies and punching through the detectors.

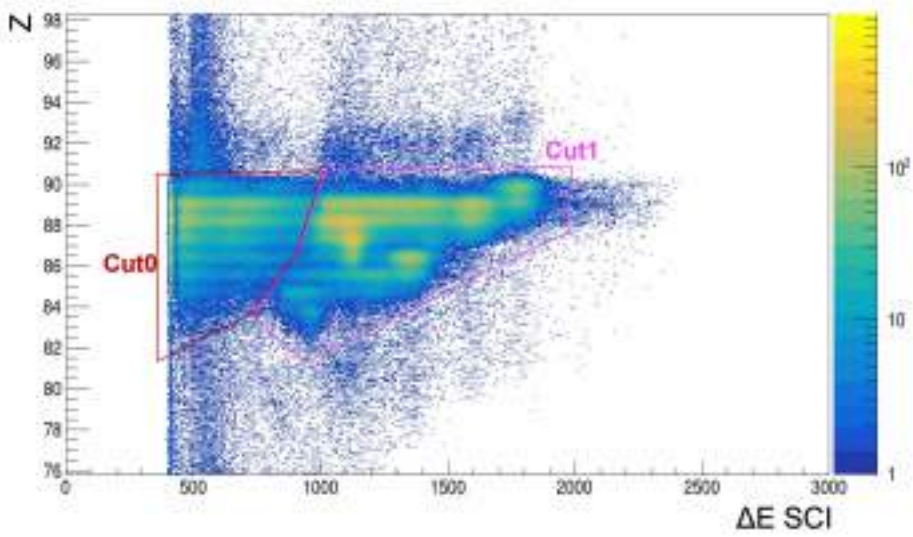

Figure 4.11: Atomic number Z measured in the MUSIC detector versus energy loss measured from SC42.

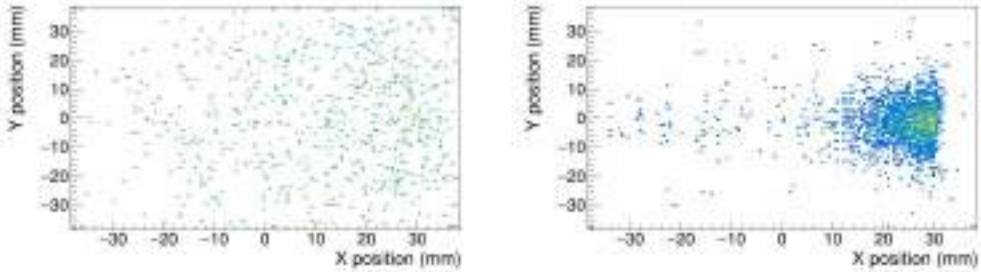

Figure 4.12: Position distribution in AIDA associated to $Cut0$ and $Cut1$, gated on Rn isotopes.

In conclusion, in order to reduce the source of background caused by secondary reactions in the S4 degrader, events belonging to *Cut0* were excluded. As shown in Tab. 4.2, this leads to an approximately 30% reduction in statistics.

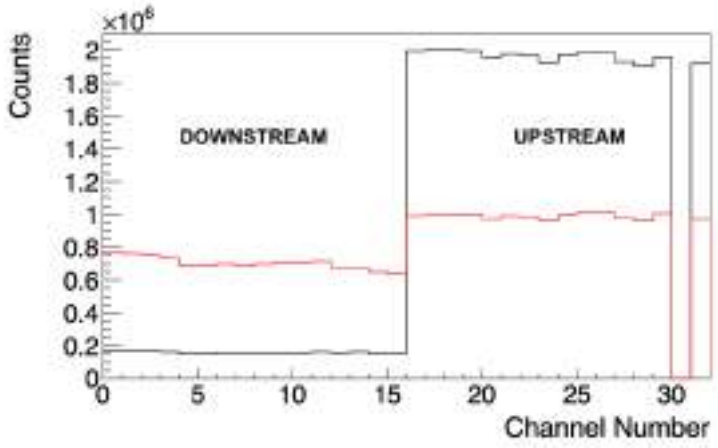

Figure 4.13: Hit pattern for the βPlastic detector associated to *Cut0* (red) and *Cut1* (black)

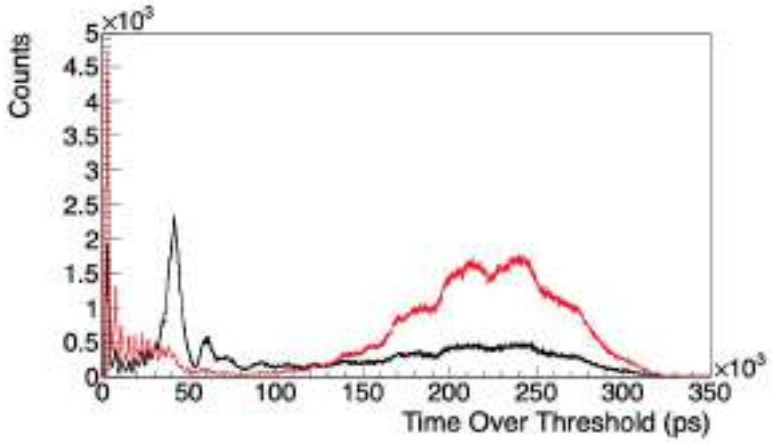

Figure 4.14: ToT spectrum from βPlastic linked to *Cut0* (black) and *Cut1* (red).

	Number of ions		
	Z1Z2 gate	Z1Z2+*Cut1*	%
Po	1.61×10^5	1.17×10^5	73%
At	4.50×10^5	3.40×10^5	76%
Rn	7.88×10^5	5.89×10^5	75%
Fr	8.95×10^5	6.20×10^5	69%
Ra	2.25×10^6	1.57×10^6	70%
Ac	3.88×10^6	2.70×10^6	70%
Th	7.80×10^5	5.23×10^5	67%

Table 4.2: Total number of ions per element of interest produced during the 6 days beamtime, fraction of ions remaining after the application of the condition on SC42 and corresponding percentage with respect to the total number of ions per each element.

4.4 Charge States Selection

Ions passing through the fragment separator can pick up or lose electrons from the several material blocks that are placed along their flying path. This effect is enhanced in the case of heavy ions and for thicker layers of materials (S1 and S2 wedges). The additional electron(s) will cause a change in the ions' $B\rho$ and therefore in the ions' trajectories along the FRS. Because of this, it is possible to detect a change in the charge state when passing through the S2 wedge by measuring the $B\rho$ before and after the wedge. The change in $B\rho$ can in turn be determined as the energy loss in the degrader as:

$$dE(S2) = (\gamma_{(Target-S2)} - \gamma_{(S2-S4)}) \cdot A/Q \tag{4.4}$$

where $\gamma_{(Target-S2)} = \sqrt{1 + \frac{uB\rho}{c \cdot A/Q}^2}$, hence the different charge states changes can be visualised by plotting the energy loss in MUSIC as a function of the energy loss through the S2 degrader, as shown in Fig 4.15.

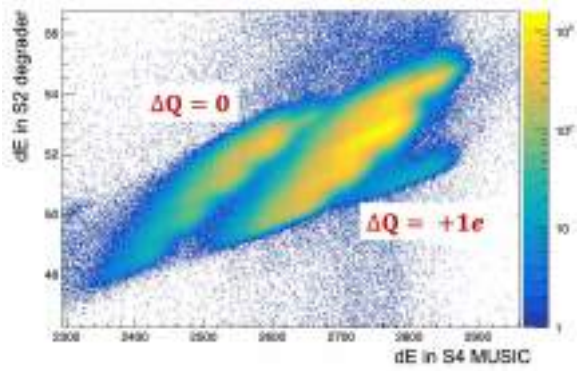

Figure 4.15: Calculated energy loss in S2 degrader versus energy loss measured in the MUSIC detectors.

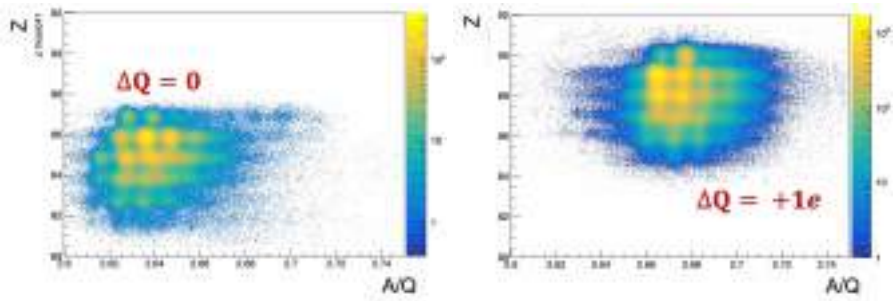

Figure 4.16: ID plot associated to the left region of Fig. 4.17, for ions that do not change their charge states (left) and to the right region, corresponding to ions that pick up an electron (right).

A condition on the two main regions in Fig. 4.15 results in the ID plots shown in Fig. 4.16, corresponding to ions that do not change charge state between S2 and S4 ($\Delta Q = 0$) and ions that pick up one electron between the two focal planes ($\Delta Q = 1$). Among the

ions of interest, radon and francium have a components in both regions, while polonium and astatine isotopes have a contribution only with $\Delta Q = 0$. Nevertheless, while radon and francium isotopes are well separated in the Z versus A/Q plot, polonium and astatine isotopes have overlapping contributions that make their identification unclear.

In order to understand the origin of this effect, the position at the final focal plane (S4) was plotted, with a condition on the atomic number Z for radon, francium (Fig. 4.17), polonium and astatine (Fig. 4.18) isotopes. The *loci* were identified here on the basis of the A/Q ratio value corresponding to their centre, and confirmed by a comparison with LISE++ simulations performed using the experimental conditions. In the case of radon and francium, two distinct regions can be seen in Fig. 4.17, the one on the top corresponding to fully stripped ions, and the one at the bottom corresponding to ions that pick up electrons in the S2 wedge. In the case of francium and radon, ions which start from S2 as H-like (1 electron), reach S4 He-like (2 electrons). In the case of polonium and astatine, instead, two different contributions, almost overlapping, are present. By comparing the position distributions with the ones obtained with LISE++ simulations, the *blobs* at the bottom correspond to fully stripped ions, while the ones at the top are hydrogen-like ions (+1 e). The reason why the two regions cannot be separated with the method used for radon and francium is that polonium and astatine isotopes do not change charge state between S2 and S4, but reach S2 already in their final charge state (fully stripped or hidrogen-like).

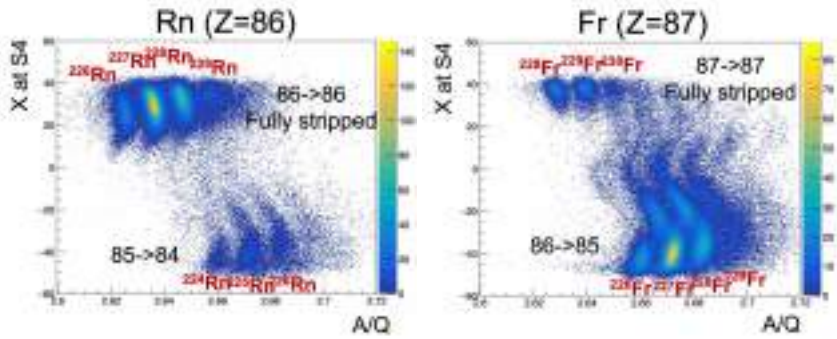

Figure 4.17: X position at S4 as a function of A/Q for Rn and Fr isotopes.

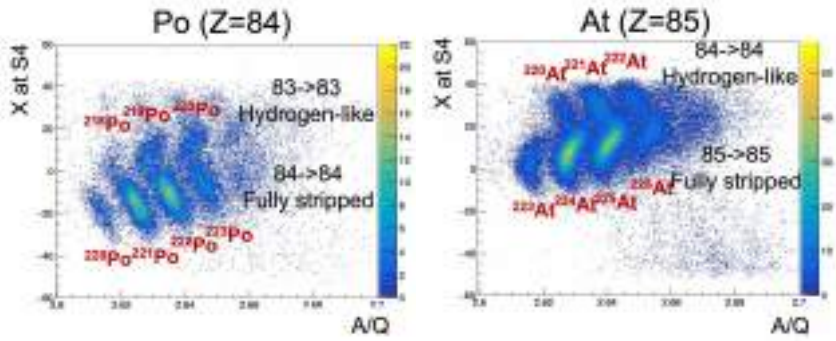

Figure 4.18: X position at S4 as a function of A/Q for Po and At isotopes.

The yields obtained for each isotope are reported in Tab. 4.3 and Tab. 4.4, considering the total number of ions detected during the whole experimental time (4.75×10^5 s, corresponding to $\sim$ 6 days of beamtime), the beam having an average intensity of 10^9 particles per spill, with a spill structure of 2 s on, 2 s off.

Charge state	Isotope	Total number	Yield (counts/s)
H-like	^{218}Po	991	4.17×10^{-3}
	^{219}Po	4065	1.71×10^{-2}
	^{220}Po	4019	1.69×10^{-2}
Fully stripped	^{220}Po	2031	8.55×10^{-3}
	^{221}Po	14074	5.92×10^{-2}
	^{222}Po	15923	6.70×10^{-2}
	^{223}Po	7171	3.02×10^{-2}

Charge state	Isotope	Total number	Yield (counts/s)
H-like	^{220}At	5752	2.42×10^{-2}
	^{221}At	16405	6.90×10^{-2}
	^{222}At	11661	4.91×10^{-2}
Fully stripped	^{223}At	9010	3.79×10^{-2}
	^{224}At	49605	2.09×10^{-1}
	^{225}At	49291	2.07×10^{-1}
	^{226}At	17205	7.24×10^{-2}

Table 4.3: Yields of fully stripped and H-like polonium and astatine isotopes

Charge state	Isotope	Total number	Yield (counts/s)
He-like	^{224}Rn	4410	1.86×10^{-2}
	^{225}Rn	14761	6.21×10^{-2}
	^{226}Rn	9016	3.79×10^{-2}
Fully stripped	^{226}Rn	35489	1.49×10^{-1}
	^{227}Rn	128464	5.41×10^{-1}
	^{228}Rn	81907	3.45×10^{-1}
	^{229}Rn	14043	5.91×10^{-2}

Charge state	Isotope	Total number	Yield (counts/s)
He-like	^{226}Fr	27448	1.16×10^{-1}
	^{227}Fr	80162	3.37×10^{-1}
	^{228}Fr	26789	1.13×10^{-1}
	^{229}Fr	9108	3.83×10^{-2}
Fully stripped	^{228}Fr	11872	5.00×10^{-2}
	^{229}Fr	11695	4.92×10^{-2}
	^{230}Fr	3508	1.48×10^{-2}

Table 4.4: Yields of fully stripped and He-like radon and francium isotopes

4.5 Analysis of the Implanted Ions

The ions reaching S4, being selected and identified by the FRS, are implanted in the AIDA detector, a scheme of which is shown in Fig. 4.19. In the following section, the implantation position and profile of the ions of interest is discussed.

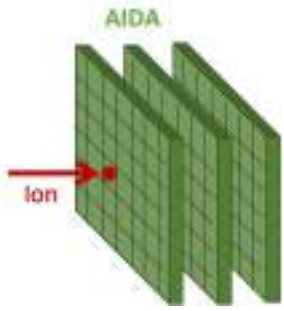

Figure 4.19: Sketch of the AIDA array

4.5.1 Implantation profile

The thickness of the final degrader at S4 was optimised in order to implant the ions of interest (Z=84-87) in the AIDA DSSDs. The implanted ions' position distribution in the three layers of AIDA is shown in Fig.4.20. Lighter ions, such as polonium, are mainly implanted in the second and third layer, while the heaviest element (francium) is mainly implanted in the first tile. The ion species also implant in different x positions according to their magnetic rigidities. As the *narrow* AIDA+βPlastic configuration was used for *Dataset1*, a portion of the ions are lost by the AIDA acceptance.

The number of ions implanted per element is given in Tab. 4.5, for each tile, and the percentage with respect to the total number of ions measured in the FRS is also reported. We define an ion as implanted when it releases energy in a layer of AIDA, disregarding the fact that it can be detected also by subsequent layers. Therefore, the total number of implants corresponds to the ions detected in the first DSSD. The percentage of ions implanted with respect to the total number of ions detected in the FRS hints that the thickness of the degrader at S4 was too high, as some ions of interest do not reach the DSSDs. Numbers for heavier species (radon, actinium and thorium) are also given here with the purpose of indicating that they are almost fully suppressed by the S4 degrader.

In Tab. 4.6, the number of ions which are stopped in the AIDA array are reported. The *stopped* flag in AIDA data, as explained in Sec. 3.2, indicates ions that are detected in an AIDA layer and not in the subsequent one(s). This definition is meaningless for the last AIDA layer (DSSD3) since it is not easy to define whether there had been a signal also in the βPlastic detector right after it.

The total number of implanted ions for each ion of interest in the charge states produced is reported in Tab.4.7.

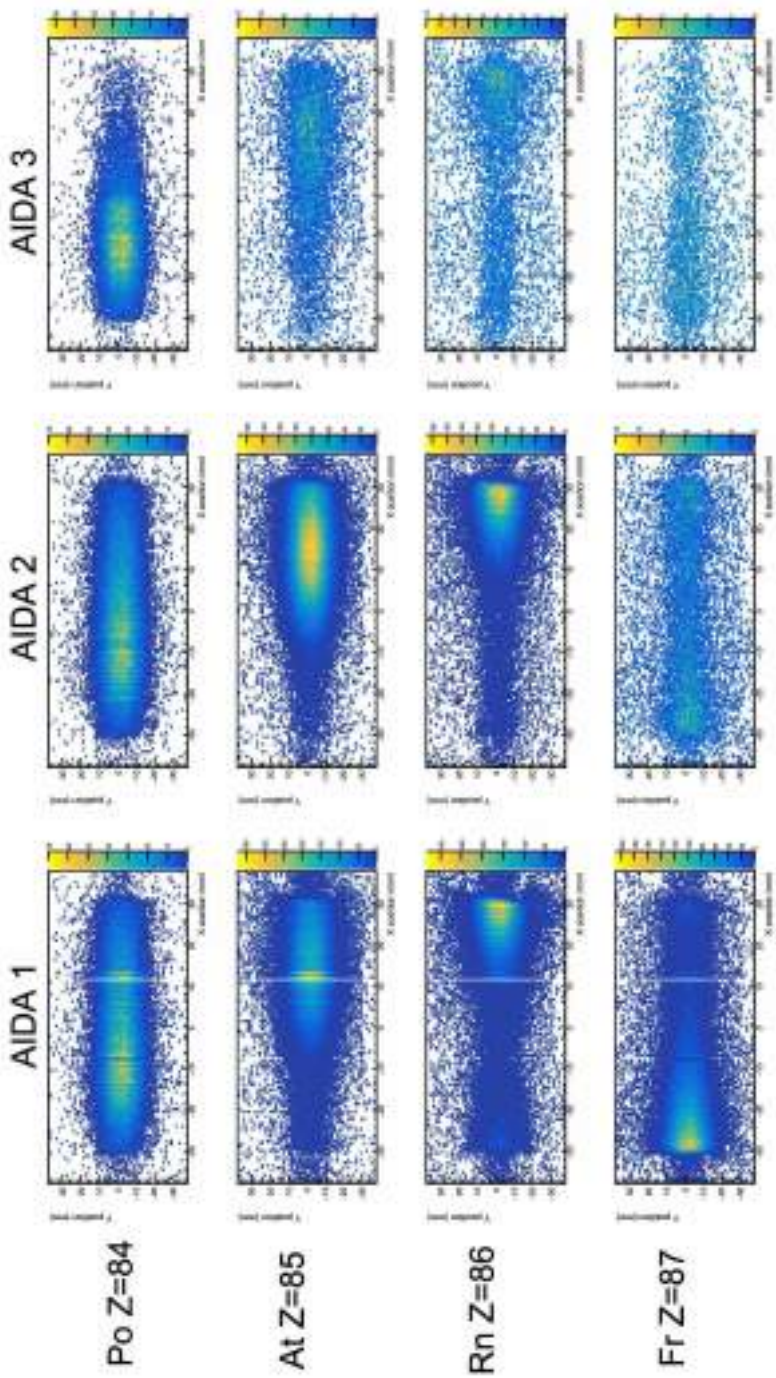

Figure 4.20: XY position of the implanted ions on the DSSD detectors.

Element	Number of ions	Implants DSSD1	DSSD2	DSSD3	%
Po	1.17×10^5	7.11×10^4	6.701×10^4	2.62×10^4	61%
At	3.40×10^5	1.96×10^5	1.696×10^5	8.79×10^3	58%
Rn	5.89×10^5	1.45×10^5	8.395×10^4	6.79×10^3	25%
Fr	6.20×10^5	1.08×10^5	1.108×10^4	3.96×10^3	17%
Ra	1.57×10^6	1.80×10^5	2.310×10^4	9.32×10^3	12%
Ac	2.70×10^6	6.56×10^4	2.896×10^4	1.41×10^4	2.4%
Th	5.23×10^5	8.06×10^3	5.646×10^3	2.93×10^3	1.5%

Table 4.5: Total number of ions per element of interest produced during the 6 days beamtime, fraction of ions implanted in the three AIDA detectors and percentage with respect to the ions produced.

Element	Number of ions	Stopped DSSD1	DSSD2	Total	%
Po	1.17×10^5	3.49×10^3	2.66×10^4	3.01×10^4	26%
At	3.40×10^5	1.82×10^4	1.14×10^5	1.33×10^5	39%
Rn	5.89×10^5	4.73×10^4	2.25×10^4	6.97×10^4	12%
Fr	6.20×10^5	5.00×10^4	1.35×10^3	5.13×10^4	8.3%
Ra	1.57×10^6	2.36×10^4	2.00×10^3	2.56×10^4	1.6%
Ac	2.70×10^6	8.58×10^3	2.05×10^3	1.06×10^4	0.39%
Th	5.23×10^5	9.79×10^2	3.58×10^2	1.34×10^3	0.26%

Table 4.6: Total number of ions per element of interest produced during the 6 days beamtime, fraction of ions stopped in the first two AIDA detectors, total of stopped ions and percentage with respect to the ions produced. The ions stopped in DSSD3 cannot be accounted for.

Charge States	Element	N. of ions	DSSD1	DSSD2	DSSD3	Total	%
H-like	^{218}Po	9.91×10^2	244	316	21	5.81×10^2	58.6%
	^{219}Po	4.07×10^3	1049	1201	51	2.30×10^3	56.6%
	^{220}Po	4.02×10^3	1028	1186	58	2.27×10^3	56.5%
Fully stripped	^{220}Po	2.03×10^3	478	525	367	1.37×10^3	67.5%
	^{221}Po	1.41×10^4	3407	3534	2276	9.22×10^3	65.5%
	^{222}Po	1.59×10^4	3790	4168	1763	9.72×10^3	61.1%
	^{223}Po	7.17×10^3	1655	1824	668	4.15×10^3	57.8%
H-like	^{220}At	5.75×10^3	700	703	20	1.42×10^3	24.7%
	^{221}At	1.64×10^4	1211	951	62	2.22×10^3	13.6%
	^{222}At	1.17×10^4	637	492	46	1.18×10^3	10.1%
Fully stripped	^{223}At	9.01×10^3	2219	2630	87	4.94×10^3	54.8%
	^{224}At	4.96×10^4	12232	14560	418	2.72×10^4	54.9%
	^{225}At	4.93×10^4	12279	13932	3512	2.66×10^4	53.9%
	^{226}At	1.72×10^4	4105	4600	137	8.84×10^3	51.4%
He-like	^{224}Rn	4.41×10^3	95	8	3	1.06×10^2	2.40%
	^{225}Rn	1.48×10^4	547	43	22	6.12×10^2	4.15%
	^{226}Rn	9.02×10^3	692	46	14	7.52×10^2	8.34%
Fully stripped	^{226}Rn	3.55×10^4	4619	5083	179	9.88×10^3	27.8%
	^{227}Rn	1.28×10^5	11963	9447	469	2.18×10^4	17%
	^{228}Rn	8.19×10^4	5245	3756	286	9.29×10^3	11.3%
	^{229}Rn	1.403×10^4	577	371	28	9.76×10^2	7%
He-like	^{226}Fr	2.74×10^4	538	72	34	6.44×10^2	2.35%
	^{227}Fr	8.02×10^4	2865	272	102	3.24×10^3	4.04%
	^{228}Fr	2.68×10^4	3210	241	81	3.53×10^3	13.18%
	^{229}Fr	9.11×10^3	952	65	22	1.04×10^3	11.41%
Fully stripped	^{226}Fr	1.19×10^4	223	65	19	3.07×10^2	2.59%
	^{227}Fr	1.17×10^4	185	82	35	3.02×10^2	2.58%
	^{228}Fr	3.51×10^3	67	22	8	97	2.77%

Table 4.7: Total number of ions of interest produced during the 6 days beamtime, fraction of ions implanted in the three AIDA detectors, total of implanted ions and percentage with respect to the ions produced.

The implantation profile and position distribution for *Dataset 2* is shown in Fig.4.21 for a few ion species, in the two AIDA layers. In the top row, the XY implantation position for ^{106,107}Sb in AIDA1 (top) and AIDA2 (bottom) is shown. The distribution of ^{102,103,104,105}Sn is shown in the second row, while in the third row the XY position of implanted ^{101,102}In and ^{98,100}Cd is given. A strong position overlap is observed for different isotopes, owing to the use of a partially monochromatic setting for the S2 degrader.

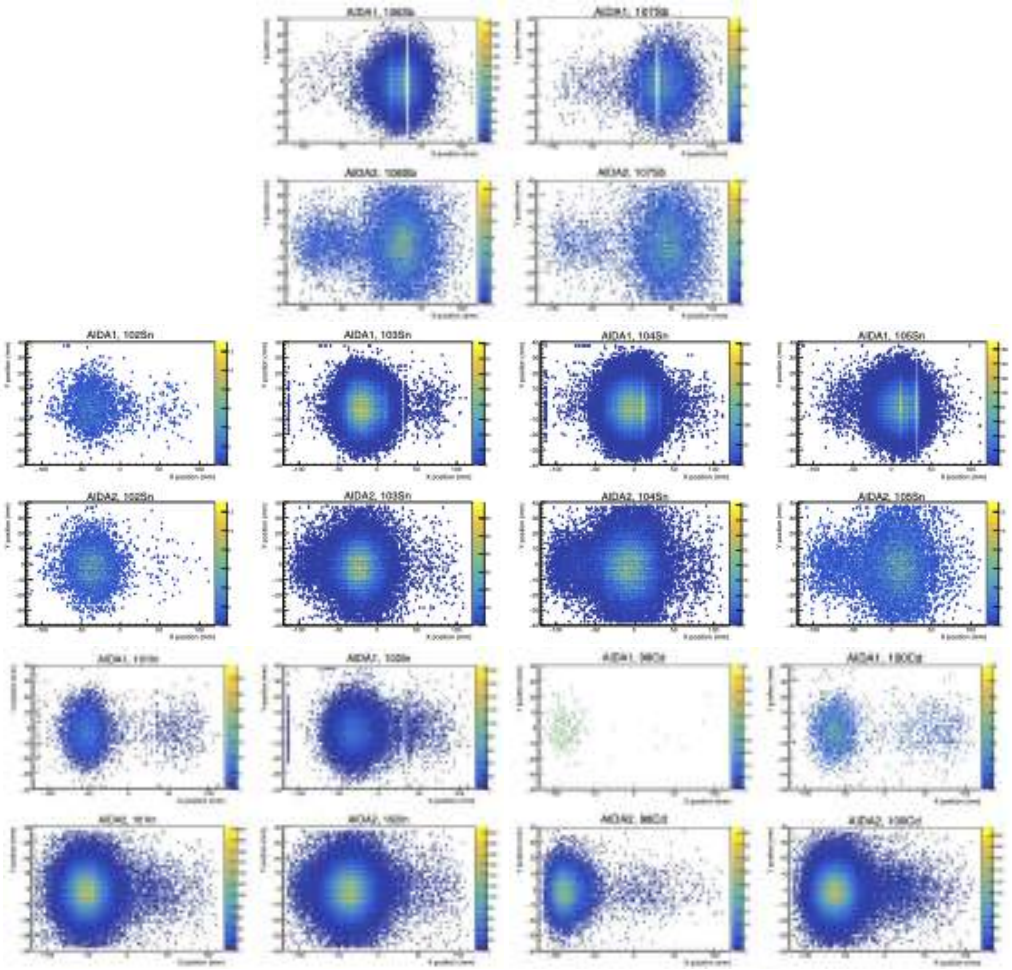

Figure 4.21: XY position of the implanted ions on the DSSD detectors: ^{106,107}Sb (first row), ^{102,103,104,105}Sn (second row), ^{101,102}In and ^{98,100}Cd (third row).

4.6 Fission fragments

In the experiment of *Dataset 1*, using the fissile ^{238}U primary beam, the data show a strong contribution of fission fragments. It was estimated that fission products account for approximately 90% of the rate on the DSSD detectors.
The complete ID plot from *Dataset 1*, shown in Fig. 4.22, indicates a strong contribution from ions with atomic number smaller than 70. The fission fragments are partially also implanted in the AIDA stack, as shown in Fig. 4.23, which displays that a large fractions is implanted and stopped in the DSSD detectors. Further analysis is being performed on the fission fragments' data to better account for the produced species and establish which isotopes have been implanted in the silicon detectors.

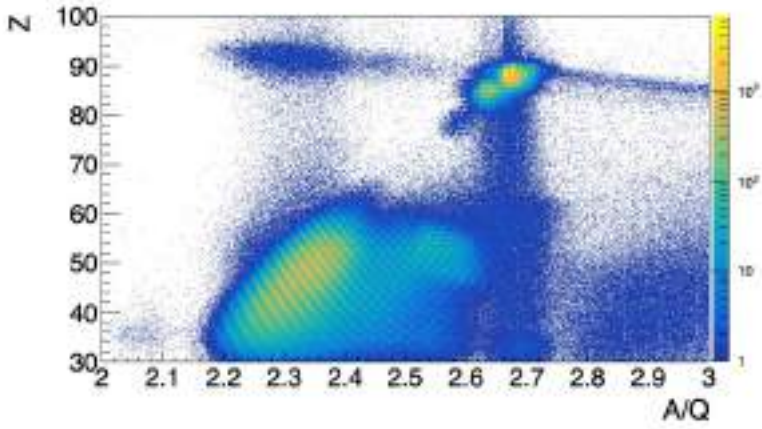

Figure 4.22: ID plot from *Dataset 1*, where the contribution on the top-right corner accounts for the heavy ions of interest, while the one on the bottom-left corner accounts for the fission fragments.

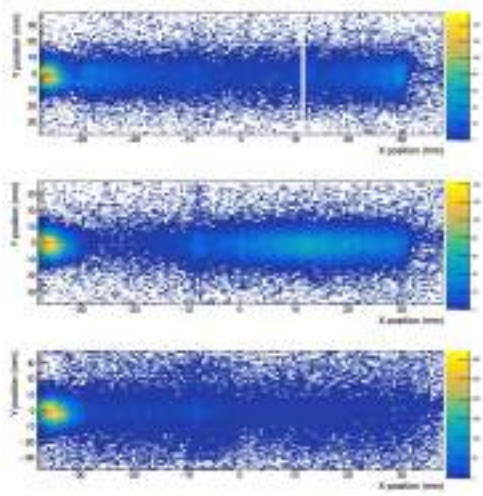

Figure 4.23: XY position distribution of fission fragments ($Z \leq 70$) from *Dataset 1*, which are stopped in the AIDA detectors.

4.7 Comparison of implantation profile with the LISE++ simulation

In order to confirm the hypothesis that the S4 degrader was thicker than expected, we compared our results with the values obtained with the LISE++ simulations (Sec.2.5). LISE++ gives as an output the implantation depth distributions for each given ion, and it calculates the area of each depth distribution. The result of our comparison are given in Tab. 4.8 and Fig. 4.24. The plots show a discrepancy of approximately one AIDA layer between the experiment and the simulation, i.e. the AIDA layer where an ion species is primarily implanted in the simulation is generally the one after the main implantation layer in the experimental data. Our hypothesis is that there was an error during the S4 degrader calibration, which should have been thinner of a value between 0.5 and 1 mm (the thickness of one AIDA layer, approximately).

To prove the real degrader thickness, several values of degrader thickness where set in the LISE++ simulations, and the best agreement between simulated and experimental values was obtained when increasing the thickness of 0.8 mm. The values are reported in Tab.4.9, where the implantation yields for each AIDA layer experimentally measured are compared with the values obtained in the LISE++ simulations for the different degrader thickness increasements, ranging from 0.5 to 1 mm.

Ion		DSSD1	DSSD2	DSSD3
Po	Exp	1.0×10^{-2}	1.1×10^{-1}	1.1×10^{-1}
	Sim	0	1.5×10^{-3}	3.7×10^{-1}
At	Exp	8.0×10^{-2}	4.8×10^{-1}	3.7×10^{-2}
	Sim	0	1.7×10^{-1}	1.5
Rn	Exp	2.0×10^{-1}	9.5×10^{-2}	2.9×10^{-2}
	Sim	1.4×10^{-3}	1.5	1.4×10^{-1}
Fr	Exp	2.1×10^{-1}	5.7×10^{-3}	1.7×10^{-2}
	Sim	2.0×10^{-2}	3.6×10^{-1}	0

Table 4.8: Implantation yield for polonium, astatine, radon and francium isotopes obtained with experimental data and LISE++ simulations. The experimental values correspond to stopped ions in the three AIDA detectors.

4.8 Ion-β and β -γ correlations

One of the primary goals of the experimental runs under analysis, is the measurements of the decay patterns starting from radioactive species produced by the primary fragmentation reaction. In order to study the decay, the ion and subsequently emitted radiation, both β particles and γ rays, need to be correctly correlated with the parent nucleus. This is achieved through a series of conditions on time and position, as described in the following.

4.8.1 Ion-β correlations

Traditionally, in implantation detectors, the correlation of the β particle with an implanted ion is made when the ion and beta events are detected is neighbouring pixels, as shown in Fig. 4.25 (left panel).
Due to the high number of pixels in the AIDA detectors, the ion-β correlation algorithm is modified as follows. On the basis of the assumption that clusters generated by the ion and the β will form overlapping contributions, as shown in Fig. 4.25 (right panel), the position conditions are set as follows:

- The ion and β are detected within the same DSSD,
- The ion and β clusters overlap or are adjacent.

Moreover, a time condition is applied, requiring the β to be detected less than five β decay lifetimes after the implantation of the ion.

While more than one β particle can be correlated to a single ion, each β particle cannot be correlated to more than one ion.

An example of the implantation and decay position distribution for a given ion (^{224}At) is given in Fig. 4.26, where the XY distribution of the implanted ions in the three DSSDs is given on the left panels, and the distribution of correlated β events is in the right panels. The total numbers of betas correlated to the implanted ions for each DSSD are given in Tab. 4.10. As shown both in Fig. 4.26 and Tab. 4.10, DSSD2 proved to be the detector where the lowest noise level was achieved.

In *Dataset1* and *Dataset2* we are dealing with rather long β decay lifetimes, ranging from tens of seconds to several minutes therefore covering several beam spills. If the implantation rate would ensure that a single ion is implanted per pixel, one has to take

Element	S4 deg increasement (mm)	DSSD1	DSSD2	DSSD3
Po	0	0	1.54×10^{-3}	3.66×10^{1}
	0.5	2.87×10^{-8}	5.98×10^{-2}	$\mathbf{3.03 \times 10^{-1}}$
	0.75	1.74×10^{-4}	$\mathbf{2.31 \times 10^{-1}}$	1.44×10^{-1}
	0.8	5.82×10^{-4}	$\mathbf{2.70 \times 10^{-1}}$	1.07×10^{-1}
	1	8.85×10^{-4}	$\mathbf{3.45 \times 10^{-1}}$	2.04×10^{-2}
	Exp	1.0×10^{-2}	$\mathbf{1.1 \times 10^{-1}}$	1.1×10^{-1}
At	0	0	1.65×10^{-1}	**1.48**
	0.5	2.06×10^{-2}	**1.23**	5.21×10^{-2}
	0.75	1.11×10^{-1}	**1.21**	5.04×10^{-4}
	0.8	1.20×10^{-1}	**1.16**	4.65×10^{-5}
	1	4.12×10^{-1}	$\mathbf{8.65 \times 10^{-1}}$	0
	Exp	8.0×10^{-2}	$\mathbf{4.8 \times 10^{-1}}$	3.7×10^{-2}
Rn	0	1.38×10^{-3}	**1.48**	1.37×10^{-1}
	0.5	2.25×10^{-1}	$\mathbf{9.96 \times 10^{-1}}$	0
	0.75	**1.02**	2.34×10^{-1}	0
	0.8	**1.12**	1.36×10^{-1}	0
	1	$\mathbf{1.20 \times 10^{-1}}$	6.21×10^{-3}	0
	Exp	$\mathbf{2.0 \times 10^{-1}}$	9.5×10^{-2}	2.9×10^{-2}
Fr	0	1.96×10^{-2}	$\mathbf{3.61 \times 10^{-1}}$	0
	0.5	$\mathbf{2.24 \times 10^{-1}}$	7.07×10^{-4}	0
	0.75	$\mathbf{2.12 \times 10^{-1}}$	2.52×10^{-8}	0
	0.8	$\mathbf{2.11 \times 10^{-1}}$	1.22×10^{-9}	0
	1	$\mathbf{1.43 \times 10^{-1}}$	0	0
	Exp	$\mathbf{2.1 \times 10^{-1}}$	5.7×10^{-3}	1.7×10^{-2}

Table 4.9: Relative comparison of implantation yields for each AIDA layer experimentally measured with the values obtained in the LISE++ simulations for the different degrader thickness increasements, ranging from 0.5 to 1 mm. The values in **bold** correspond to the highest yield obtained, therefore the corresponding layer is the one where the highest fraction of ions was implanted.

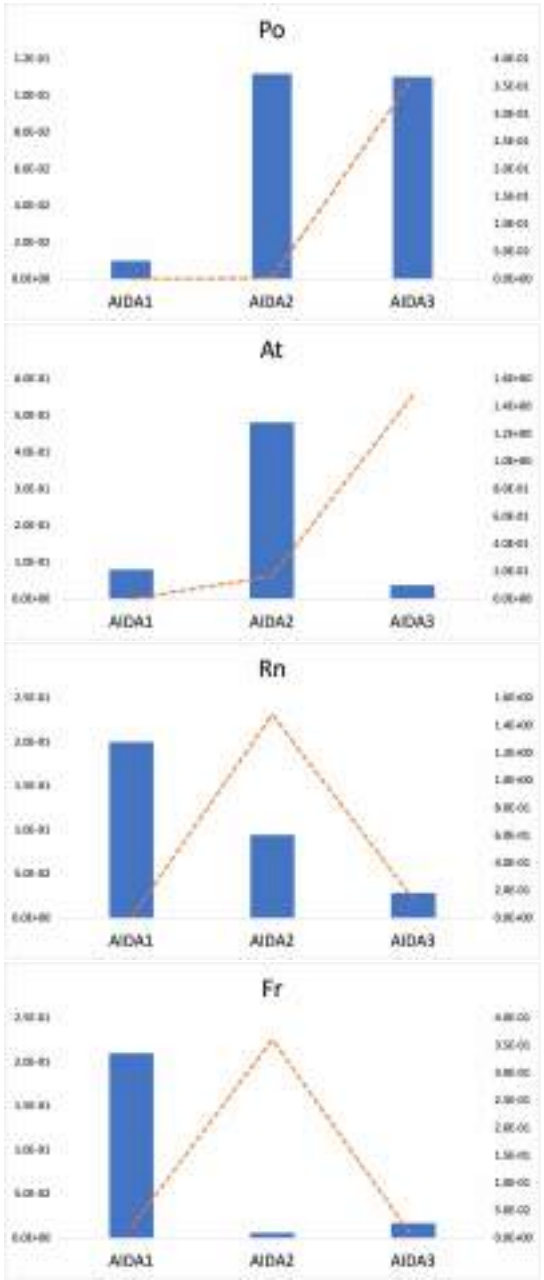

Figure 4.24: Implantation yield for polonium, astatine, radon and francium isotopes obtained with experimental data (blue columns) and LISE++ simulations (orange dashed lines). The experimental values correspond to stopped ions in the three AIDA detectors.

into account the chance that ions corresponding to subsequent events are implanted in the same position. In case this occurs, one needs to interrupt the correlation with β , since ion-β matching is not unique anymore, and we lose the implantation reference time.

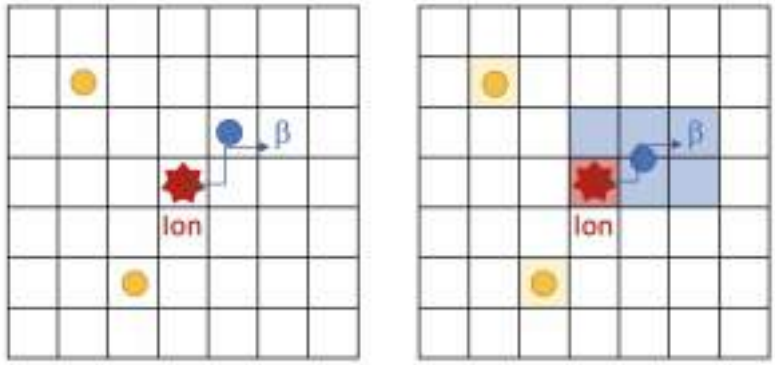

Figure 4.25: Ion and β position correlation as usually implemented (left panel) and the implementation in the case of higly-segmented detectors such as AIDA (right panel).

	Implant events	Correlated decay events
DSSD1	828	1.11×10^5
DSSD2	1.16×10^4	1.44×10^5
DSSD3	96	3.12×10^4

Table 4.10: Total number of implant events and correlated decay events for ^{224}At.

4.8.2 β -γ correlations

To study the deexcitation pattern in the daughter nuclei, β -γ correlations are established. The γ rays in prompt coincidence with a β particle previously associated to an implanted ion are considered as emitted following this ion's β decay. In order to do this, a time condition is set, so that the timestamp of the decay event in AIDA and the γ event in FATIMA or Germanium are within ~ 100 ns from each other.

The long ion-β correlation time gives rise to a higher-than-usual background level, caused by random correlations that occur even after the application of the above mentioned conditions. In order to characterise the background we are working on establishing *backwards* time correlations. This means correlating an ion with a previously detected β and coincident γ rays, to ensure the events are fully uncorrelated.

In *Dataset1*, due to the erroneous calibration of the degrader at S4 (Sec. 4.7), a smaller fraction of the ions of interest was implanted. This, together with the rather low γ efficiency and the high noise level in AIDA, makes the γ spectroscopy analysis of the daughter nuclei difficult. Figure 4.27 reports an example of the comparison between the β -γ correlation spectra obtained correlating to ^{224}At$\rightarrow^{224}$Rn (red) and ^{225}At$\rightarrow^{225}$Rn (black). These two spectra follow the decay of neighbouring nuclei in our identification plot, and the clear difference between the peaks visible in the red spectrum, compared to the black one, confirm that the correlation procedure works correctly, and that there are no cross contamination between the two isotopes. It also shows a high background level, therefore we have to further work in order to characterise it and remove it.

In *Dataset2*, the use of the *wide* AIDA configuration, and the not-fully achromatic settings of the FRS, cause the fraction of ions of interest which got implanted in the stack of DSSD to be much higher. Therefore, even if ion-β matches should be unique, we still see cross contamination from other decay processes. Nevertheless, it is not hard to

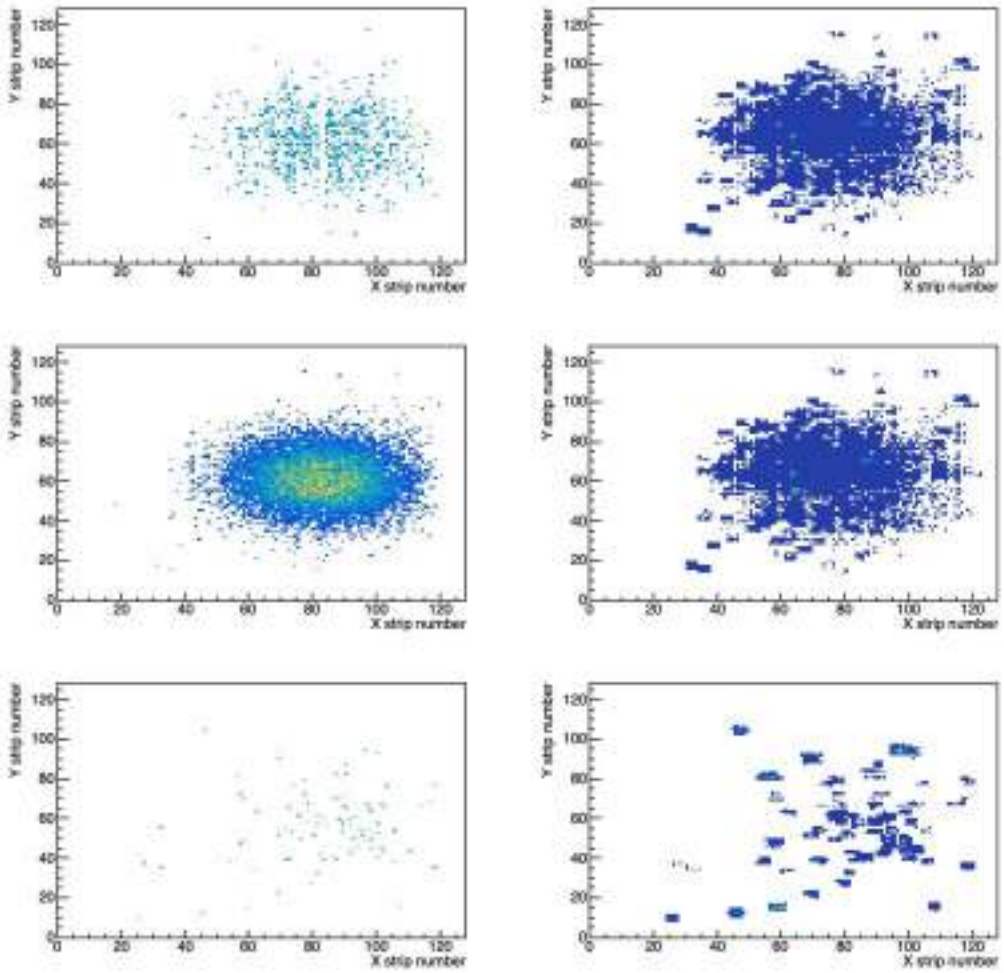

Figure 4.26: Example of XY position (given as XY strip number) of implanted ions (left panels) and correlated β particles (right panels) in the three AIDA layers.

disentangle the γ cascades belonging to different ions. The not-fully achromatic mode, though, generates a higher overlap in implanted nuclei, and therefore high chance of random correlations makes the β -γ correlations more ambiguous. Moreover, the high counting rate does not allow a precise reconstruction of the ID plot because of pile-up effects, which may cause contamination in our spectra. As an example, β -delayed γ -ray spectra for two neighbouring nuclei (^{101}Cd and ^{102}Cd) are reported in Fig. 4.28.

Figure 4.28 reports the comparison between the decay patterns ^{101}In$\rightarrow^{101}$Cd and ^{102}In$\rightarrow^{102}$Cd, obtained imposing ion-β -γ correlations. In the figure, γ transitions belonging to ^{102}Cd are seen in the spectrum of ^{101}Cd and *viceversa*, together with peaks belonging to other nuclei populated via β decay. This is an evidence of a non well resolved PID plot, with leaking contributions from neighbouring nuclei. Moreover the noise level in AIDA decay branch was, in this experiment, very high, enhancing the probability for

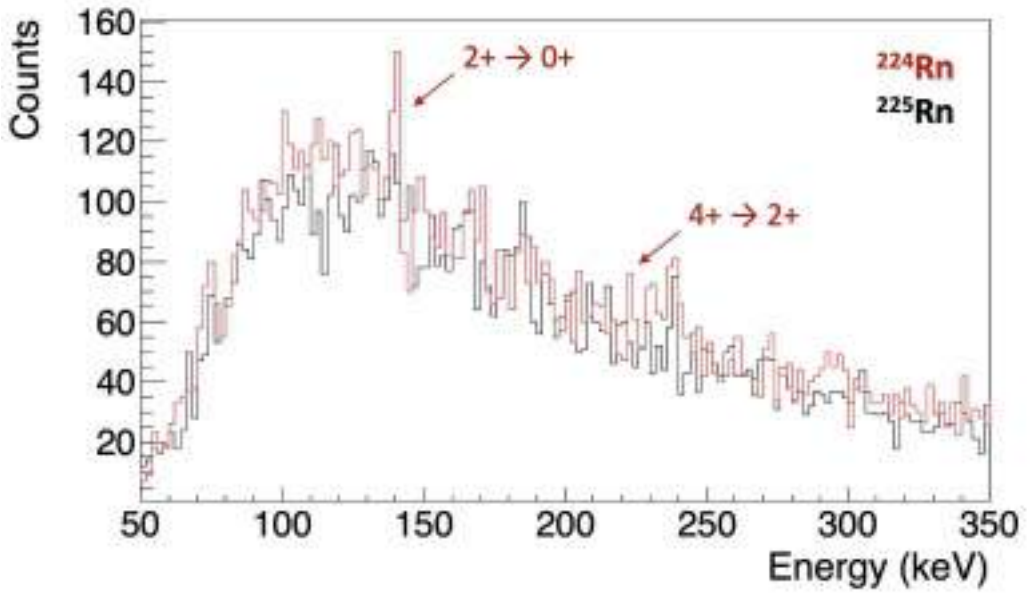

Figure 4.27: β -delayed γ -ray spectra for the decay ^{224}At$\rightarrow^{224}$Rn (red) and ^{225}At$\rightarrow^{225}$Rn (black).

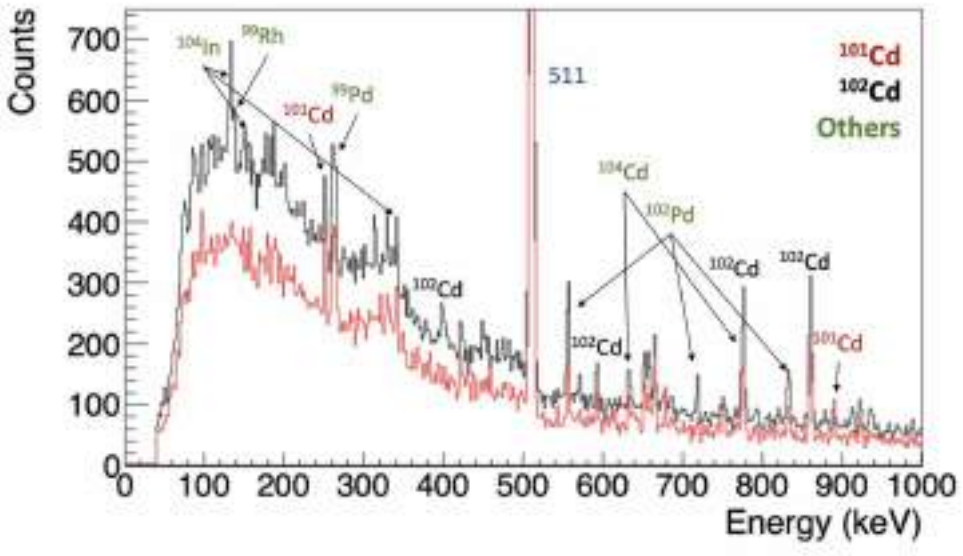

Figure 4.28: β -delayed γ -ray spectra for ^{101}Cd (red) and ^{102}Cd (black).

random coincidences. Therefore additional conditions will be studied in the future to further clean the spectrum, such high software thresholds in the AIDA decay branch, the elimination of in-spill events, or the request of a higher degree of coincidence.

Given the high statistics collected, we started investigating β decay spectra in the

off-spill time, where contributions to the γ spectrum can only be arising from β decay events, or randomly correlated background lines. This method consists in considering all γ rays in coincidence with the βPlastic detector in off-spill condition, i.e. when no beam is being delivered by the SIS-18. The spectrum in Fig. 4.29 shows contributions coming from all parents, without selection on specific branches. A more detailed description of the spectrum and the visible γ -transitions is given in Sec. 5.3.2. γ -γ coincidence matrices are to be built in order to disentangle specific decay patterns. One has to note the presence of a strong Compton background at energies below 500 keV, which is dominating the low-energy part of the spectrum.

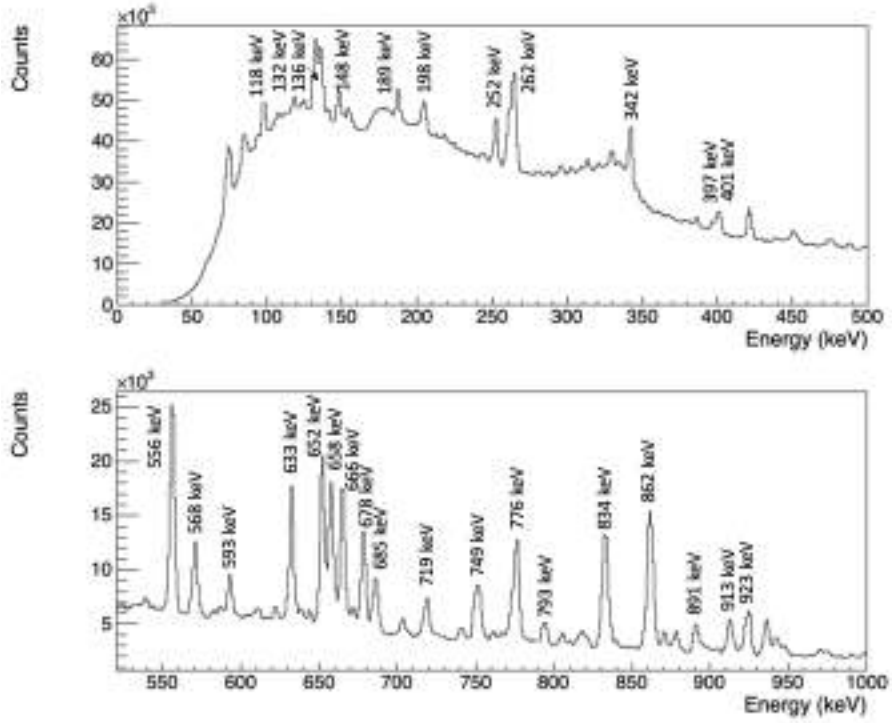

Figure 4.29: β -delayed γ -ray spectra gated on off-spill βPlastic events. The strongest peaks are labelled with their energies.

To further clean this spectrum, a coincidence condition with either of the two βPlastic detectors can be imposed. This is shown in Fig. 4.30: Here we can distinguish contributions coming from lighter (Z=43) nuclei being highlighted in the red spectrum (coincidence with downstream plastic detector), while those from heavier species (Z=49,50) are stronger in the black one (upstream plastic detector). This is owing to the different implantation depths of the species.

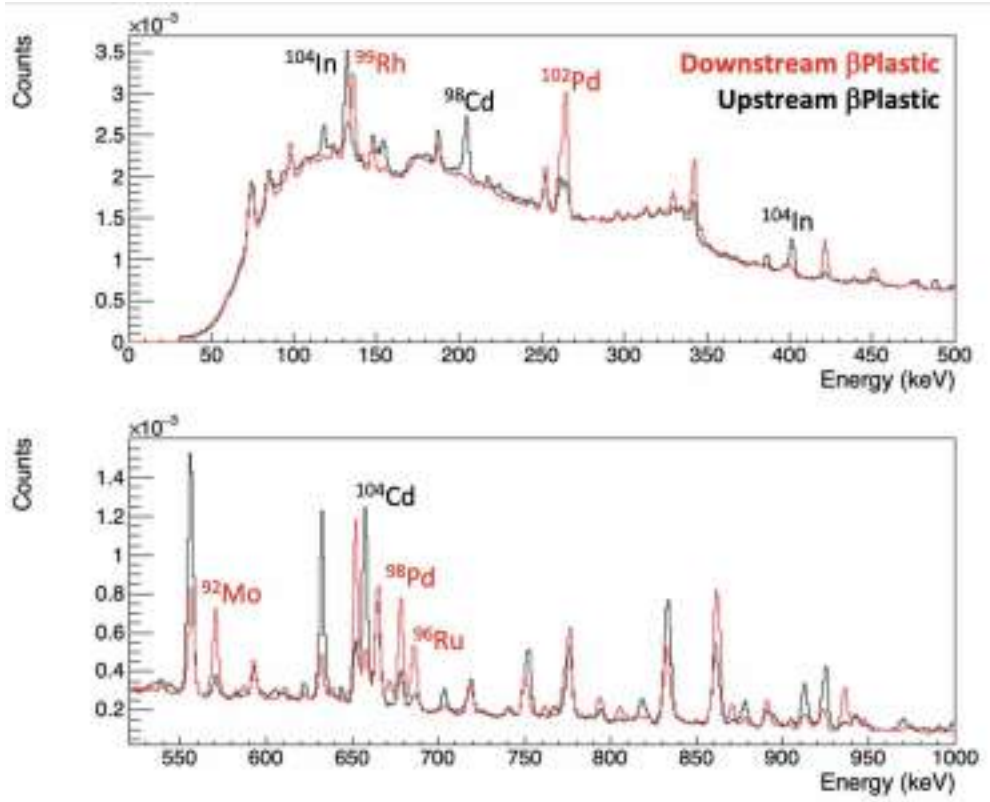

Figure 4.30: β -delayed γ -ray spectra gated on off-spill βPlastic events, for upstream (red) and downstream (black) detectors

CHAPTER 5

Results and discussion

5.1 β -decay half-lives determination in *Dataset1*

5.1.1 State of the art and present results

In general, there is a dearth of experimental information on the structure of heavy nuclei in the 220<A<230 transitional region between the Z=82 closed-shell region and the south-east corner of the A∼225, Island of Octupole Deformation. New spectroscopic results on these nuclei are important inputs to nuclear structure. Furthermore, the systematic study of their β-decay properties will help to probe the predictions of global nuclear models in more exotic nuclei with N>126, of relevance to understand the formation of the heaviest chemical elements through the r-process of explosive nucleosynthesis.

In the following we collect the spectroscopic and decay information previously known on the nuclei of interest for this thesis. They range from Z=84 to Z=88, Polonium to Francium isotopes, with mass numbers included within A=218 to A=230. These nuclei are at the border of the α emitting region, and some of them show a branching between α and β decays. The experimental information here reported comes from older studies performed mainly at ISOL facilities (such as ISOLDE, CERN), or using storage rings. The described region is not of easy access at ISOL facilities, requiring the use of Thorium targets.

Figure 5.1 shows schematically the orbitals active in the mass region of interest. The nuclei under analysis are all built starting from the ^{208}Pb core, filling the $\pi h_{9/2}$ and the $\nu h_{9/2}$ orbitals. As it can be seen from the figure, active proton-orbitals are all characterised by negative parity, while the neutron orbitals show a positive parity character. The β^- decay, transforming a neutron into a proton, will therefore mainly proceed through first-forbidden transitions, requiring a change in parity between the initial state in the mother and the final state in the daughter nucleus. In addition the selection rule on transitions between levels coming from different major shells limit the decays to transitions $\nu 1i_{13/2} \rightarrow \pi 1h_{11/2}$, and $\nu 1i_{13/2} \rightarrow \pi 1h_{9/2}$.

Light members of the Polonium isotopic chain decay via α emission up until mass A=219, being ^{219}Po, with a β -branching ratio of $28.2(20)\%$, the last known β emitter in the chain [55]. This is shown in Fig. 5.2 (top-left panel), where the light yellow shaded rectangle highlights α-decaying nuclei. ^{219}Po is also one of the heaviest isotopes whose half-life has been experimentally determined, together with $^{221-222}$Po, measured using the Schottky mass spectroscopy technique at the ESR storage ring at GSI, [56] with quite large experimental errors.

In our dataset, Polonium isotopes are implanted in the last layers of the DSSDs, between the second and third layers, with an implantation efficiency of 56%. Masses ranging between A=218 to A=223 are populated. The expected half-lives for these species

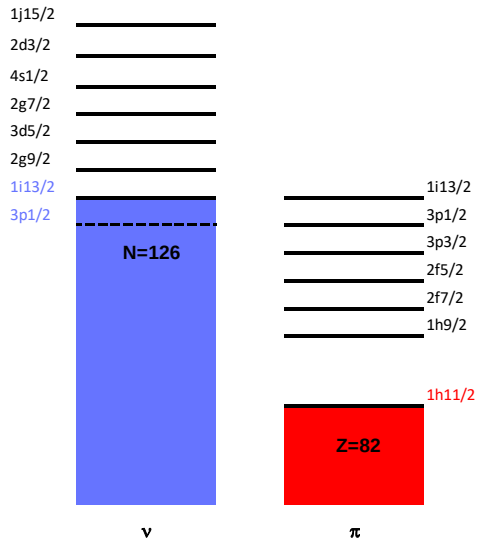

Figure 5.1: Active orbitals for neutrons (blue) and protons (red) in the Po-Fr region. Occupied orbitals are indicated with colours. The scale does not resemble the single particle energies.

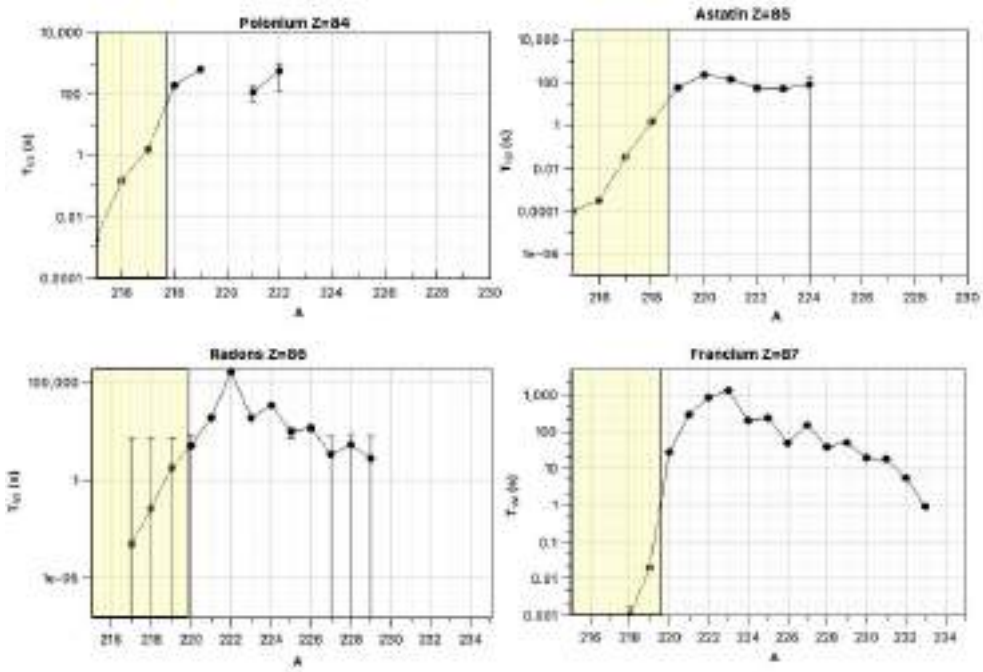

Figure 5.2: α-decay (yellow) and β -decay half-lives in seconds for polonium (top-left), astatine (top-right), radon (bottom-left) and francium isotopes (bottom-right). The errors are within the marker dimension, when not visible.

are, unfortunately, very long, of the order of hundreds of seconds and therefore not of easy access. In the populated nuclei there is no evidence of the presence of isomeric states in the time range at reach, that is lower than 10 μs. The decay patterns of ^{221}Po$\rightarrow^{221}$At and ^{222}Po$\rightarrow^{222}$At are not known at present.

In the case of the Z=85 Astatine isotopic chain, we implanted effectively nuclei with masses A=220-226, with an average implantation efficiency of 53% for fully stripped ions and 15% for H-like ions. As it is shown in Fig. 5.2 (top-right panel), they are all β emitters, and some of their half-lives are already measured. Even for nuclei in this isotopic chain such half-lives are quite long, and, therefore, not of easy access. Also in this case there was no evidence for isomeric states.

Low-lying states in $^{222-224-226}$Rn isotopes, the daughter nuclei populated by the decays ^{222,224,226}At$\rightarrow^{222,224,226}$Rn, have been recently assessed by safe-Coulomb excitation experiments induced on a ^{120}Sn at ISOLDE [57]. The level schemes obtained from these measurements, shown in Fig. 5.3, report states up to spin 10-12 $\hbar$, and show some of the linking transitions with negative parity bands, characteristic of the occurrence of octupole deformed shapes. Only in ^{222}Rn, however, the full sequence of negative parity states are measured up to J$^{\pi}$=9^{-}, and linking transitions connecting such states are fully identified. For the heavier systems only few negative-parity states have been identified.

Even if presenting a high background level, we could obtain a β -delayed spectrum for the decay ^{224}At$\rightarrow^{224}$Rn, which is reported in Fig. 5.4, where we can distinguish the $2^{+} \rightarrow 0^{+}$ and $4^{+} \rightarrow 2^{+}$ transitions at 136 and 222 keV.

The study of the decay of the odd-A ^{223}At and ^{225}At isotopes is more difficult as low energy γ-ray transitions are expected. One can expect to obtain first spectroscopic information also for the odd-A Rn isotopes, for which the last excited state known is the first 2^{+} state at 30 keV in ^{221}Rn.

Figure 5.2 (bottom-left panel) reports the half-lives known in the Rn (Z=86) isotopic chain. In our dataset we populated nuclei ranging from ^{224}Rn to ^{229}Rn, which have been implanted mainly in first layers of the AIDA set-up with an implantation efficiency ranging from 2% to 30%. β-decay half-lives of these nuclei have been already measured, and are used as reference for our $ion - \beta$ correlation procedure. One has sto note that the half-lives reported in literature show a rather large error bar.

The low-energy spectra of the odd-even nuclei ^{225}Fr and ^{227}Fr are well known from the β decay of ^{225}Rn [58] and ^{227}Rn [59], respectively. Here, a multitude of transitions with close-lying energies, some of them very low (down to 2 keV), were observed with dedicated setups.

Fr isotopes with masses ranging between A=226-230 have been successfully populated and implanted with an implantation efficiency of 3% for A=226-228 and 12% for A=229-230, on average. They are all expected to decay through $\beta-$ emission, with half-lives measured up to the ^{232}Fr [60].

The ^{230}Fr β-decay scheme is given in Ref. [62] based on coincidence data and γ-ray energy adjustments between levels. Forty-six γ rays have not been placed in the decay scheme, even if a number of them could fit according to energy difference considerations. Since coincidence data are not available, such placements could not be confirmed. A suggested spin for the parent ground state of J=3 is given by considering the feeding to the most populated states, J$^{\pi}$= 2^{+},4^{+}, even if the nature of the decay was not fixed. The transitions not placed in the level scheme amount to 22(5)$\%$ of the β^{-} decay, when the normalization factor of 0.114 is used.

The decay of ^{232}Fr $\rightarrow^{232}$Ra was recently studied at ISOLDE [61], and the built level scheme is reported in Fig.5.5. The authors propose J$^{\pi}$=$5^{+}, 5^{-}, 6^{-}$ for the ground state of the parent nucleus, in case allowed or forbidden transitions are considered, since the most

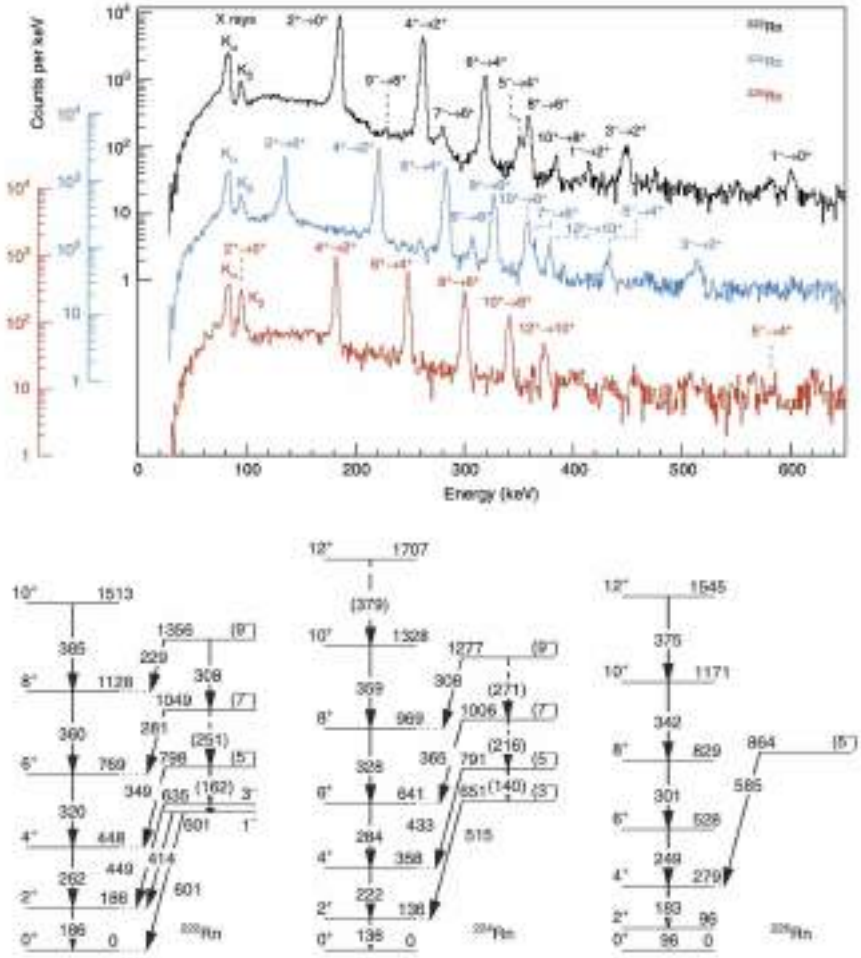

Figure 5.3: The γ -rays spectra (top panel) and level scheme (bottom panel) for ^{222}Rn (black), ^{224}Rn (blue) and ^{226}Rn (red) (adapted from [57]).

populated states are the 4^+ and 6^+ states in the daughter nucleus. These spins exclude direct ^{232}Fr ground-state to ^{232}Ra ground-state β-decay. The proposed spin ranges of the higher excited states in ^{232}Ra are then based on the ^{232}Fr ground-state spin choices discussed above and on the γ-decay characteristics of those states.

The region of the nuclei implanted in this experiment is highlighted in Fig. 5.6, which represent with red squares nuclei for which a finite probability for the delayed emission of neutrons is expected. β -delayed neutron (β n) emission probabilities in the Z $\geq$ 28 region are important input parameters in shaping the abundance curve of the astrophysical rapid neutron-capture (r) process and in the nuclear structure of the most neutron-rich nuclei, where the β n emission process competes with β decay.

Fig. 5.7 shows the detail of the heavy region, where nuclei in which the $P1n$ was measured are displayed in green, and nuclei in which the $Q_{\beta 1n}$ is non-zero. N-rich At nuclei are expected to show a non-negligible neutron-delayed branch, which has not been measured in the region. The investigation of P_n values is viable with our dataset. The

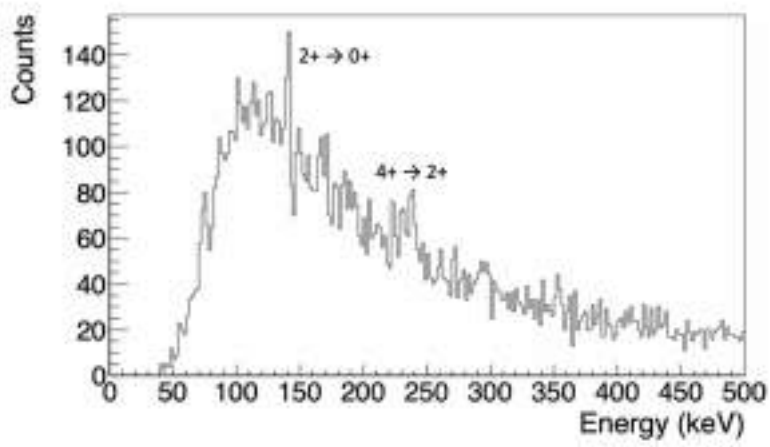

Figure 5.4: β -delayed γ -ray spectrum obtained for ^{224}Rn in this work, the $2^+ \rightarrow 0^+$ and $4^+ \rightarrow 2^+$ peaks are labelled.

direct measurement including the β-n branch in the Bateman equations describing the decay, given the long correlation times and expected low values for this branch, might not provide results, while the presence of γ transitions from the A-1 emitter can help assessing this decay branch using $ion - \beta - \gamma$ correlations.

5.1.2 Results on β -decay half-lives

The half-life of a β decay was calculated by fitting the spectrum obtained as the difference of the time stamps of the β and ion events. We started considering an isotope, whose half-life is already well known, which was populated in our dataset with enough statistics. The best candidate was the ^{227}Rn isotope, which decays with an half-life of $T_{1/2} = 20.2 \pm 0.4$ s as reported in Ref. [59].
In order to better account for the background we decided to extend the ion-β correlations to long times.
The decay spectrum is fitted using a convolution of the parent decay function and an exponential background, which takes into account both the decay of the daughter nucleus and the uncorrelated background:

$$f_1(t) = A_1 e^{-\frac{t}{T_{1/2}(Parent)} \cdot \ln 2} + A_2 e^{\frac{t}{B}} \tag{5.1}$$

with A_1, A_2 and B being the fitted parameters, $T_{1/2}$ in Eq. 5.1 is the β -decay half-life of the ion that we want to determine.

The contributions of the two functions are shown in the plot in Fig. 5.8: the parent decay curve is represented with a blue line, the background function with a green line. The total fitting function is given by the red line. The errors on the data points correspond to statistical uncertainties.

The reduced chi square of the fit was of $\chi^2 = 3.5$. The fitted value for the β -decay half-life is $T_{1/2}(^{227}Rn) = 16.1 \pm 0.3$ s. In order to prove the consistency of the fits, several tests were performed by varying the binning and lower limit of the range of the fit function (Fig. 5.9). The results of the fits are reported in Tab. 5.1, as a function of the binning and lower limit of the fit.

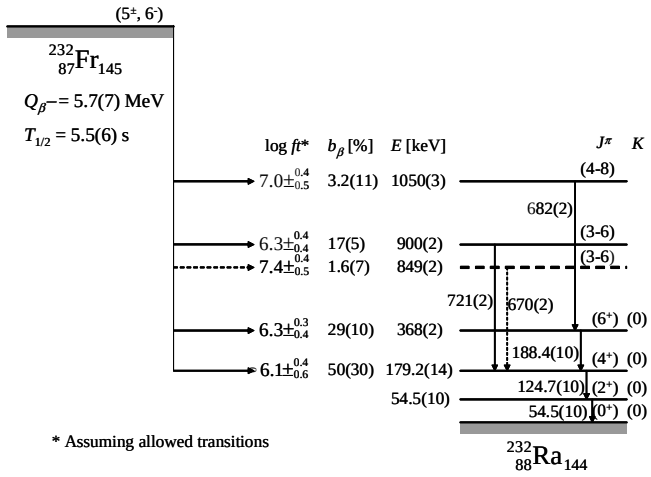

Figure 5.5: Beta-decay scheme for ^{232}Fr, adapted from Ref. [61].

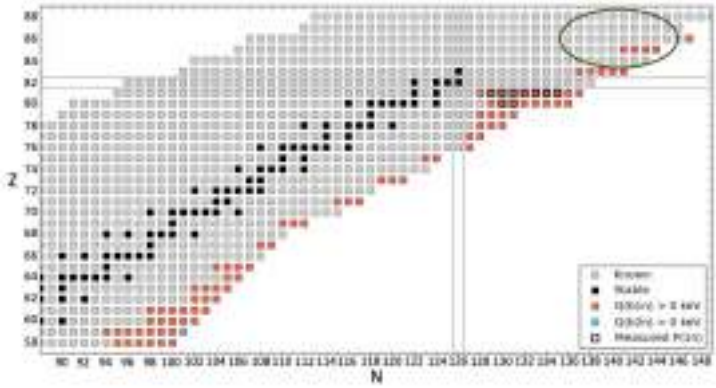

Figure 5.6: Chart of nuclides [63] for Z $\geq$ 57 nuclei. The outline surrounding the boxes indicates the measurement status of the P1n value, and colors represent the possibility of multiple beta-delayed neutron emissions. The region of interest for this thesis is indicated with a green circle (adapted from Ref. [64]).

The final value for ^{227}Rn β -decay half-life is given by the average of all the values in Tab. 5.1 and the error as the standard deviation of the same values, and corresponds to $T_{1/2}(^{227}Rn) = 16.7 \pm 1.4$ s, which is compatible within 3σ with the literature value of 20.2 ± 0.4 s from Ref. [59].

The β -decay half-life for ^{229}Rn was also measured with the same method, obtaining the result of $T_{1/2}(^{229}Rn) = 11.8 \pm 1.1$ s, which is in agreement with the literature value of $12^{+1.2}_{-1.3}$ s from Ref. [65] within 1σ.

Once we have confirmed the the correlation technique and the fitting procedure, thanks to the comparison with the previous adopted values of these two β decay half-lives, we applied the same procedure on nuclei whose β -decay half-life was never measured. The results for ^{225}At, ^{226}At, ^{220}Po and ^{223}Po are reported in Tab. 5.2.

At present the extraction of lifetimes longer than 20 s does not provide stable results,

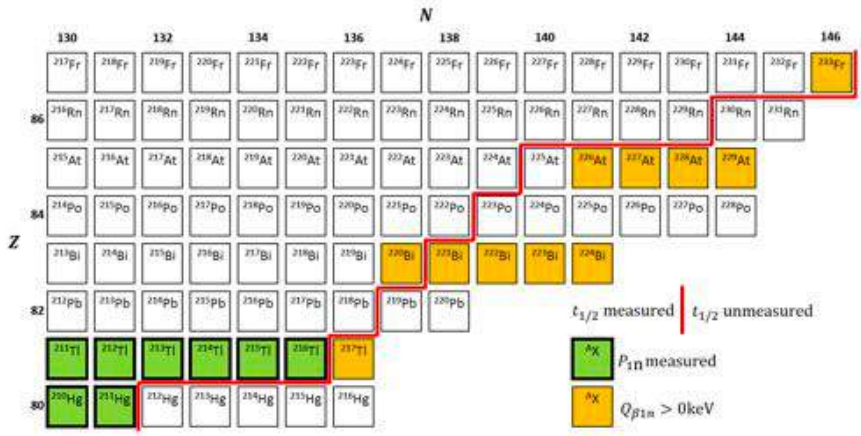

Figure 5.7: Detail of Fig. 5.6, for the heavier n-rich region. Nuclei in which the $P1n$ was measured are displayed in green, and nuclei in which the $Q_{\beta 1n}$ is non-zero. The β half-lives are known up to the red line.

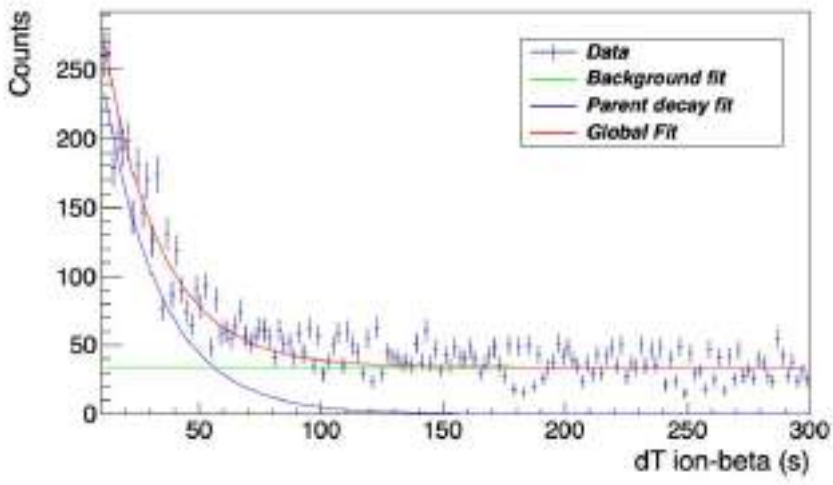

Figure 5.8: Fit of ^{227}Rn decay spectrum: the parent decay function contribution is given by the blue line, the background by the green line, while the total fit function is given by the red line.

owing to the increase in the random contributions given by the very long correlation times. We are currently working to establish a procedure to extract such values, comparing the decay patterns with MonteCarlo simulations [66]. As a result, no β -decay half-lives

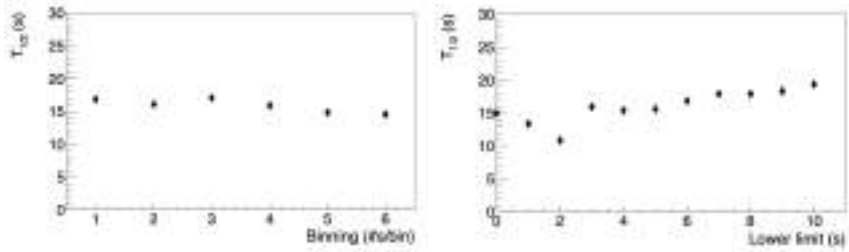

Figure 5.9: Value of the fitted β -decay half-life of ^{227}Rn as a function of the binning, ranging from 1 to 6 seconds per bin (left panel) and as a function of the lower limit of the fitting function, ranging from 0 to 10 seconds (right panel).

s/bin	$T_{1/2}(^{227}\text{Rn})$ (s)	$\sigma\, T_{1/2}(^{227}\text{Rn})$ (s)
1	16.8	0.6
2	16.1	0.3
3	17.0	0.3
4	15.9	0.3
5	14.8	0.2
6	14.6	0.5

Lower limit (s)	$T_{1/2}(^{227}\text{Rn})$ (s)	$\sigma\, T_{1/2}(^{227}\text{Rn})$ (s)
0	15.0	0.4
1	13.4	0.2
2	10.9	0.5
3	15.9	0.5
4	15.4	0.3
5	15.6	0.3
6	16.8	0.6
7	17.9	0.6
8	17.9	0.4
9	18.3	0.8
10	19.4	0.4

Table 5.1: Value of the fitted β -decay half-life of ^{227}Rn as a function of the binning and lower limit of the fit.

	Our work		Literature values	
Ion	$T_{1/2}$ (s)	$\sigma\, T_{1/2}$ (s)	$T_{1/2}$ (s)	$\sigma\, T_{1/2}$ (s)
^{227}Rn	16.7	1.4	20.2	0.4
^{229}Rn	11.8	1.1	12	$+1.2, -1.3$
^{225}At	15.8	1.3		
^{226}At	12.2	1.7		
^{220}Po	9	2		
^{223}Po	7.8	0.7		

Table 5.2: Final results for β -decay half-lives of ^{227}Rn, ^{229}Rn ^{225}At, ^{226}At, ^{220}Po and ^{223}Po.

longer than this value were confirmed or newly measured at the moment.

5.2 Comparison of the experimental results with theoretical predictions

5.2.1 Available theoretical models

Several methods for calculating β decay half-lives along the whole nuclear chart have been devised. Among the theoretical models present in literature, only a few (Ref. [67], [68], [69]) provide full β -decay tables for neutron rich isotopes. In this very exotic region, the models suffer, in particular, the shortage of experimental information.
In Ref. [67], Möller et al. performed a calculation on nuclear ground-states masses and deformations based on the Finite-Range Dropled Model and folded-Yukawa single particle potential, known as FRDM(2012). The β -decay half-lives and β -delayed neutron-emission probabilities are determined here from a Quasi-particle Random-Phase Approximation (QRPA), where first-forbidden decays are accounted for in a phenomenological treatment. Here, the single-particle energies and wave functions at the calculated ground-state deformation serve as starting point. The pairing gaps are calculated in a Lipkin–Nogami microscopic pairing model, and the odd-particle spins are obtained as the spin of the last occupied level, when this level is occupied by a single nucleon. The authors present continuous updates on their model results on the basis of new experimental findings.
Marketin et al. (Ref. [68]), provided a high precision data table of β -decay properties with the use of a self-consistent microscopic description based on the Relativistic Hartree-Bogoliubov (RHB) model for ground state of open- and closed-shell nuclei with the proton-neutron relativistic quasiparticle random phase approximation (pn-RQRPA) where the residual interaction is derived from the same density functional as was used for the ground state calculations. This framework also enables the treatment of first-forbidden transitions on an equal footing as the Gamow-Teller transitions. This model is suitable to describe properties of even-even nuclei, while approximations to include odd-A and odd-odd nuclei have been added. The authors computed the ground state of odd nuclei within the same model used for even-even nuclei, constraining the expectation value of the particle number operator to an odd number of protons and neutrons. Therefore, an even RHB state is obtained, having an energy which is different from the true odd nucleus ground state energy by the energy of the odd quasiparticle. Because of this approximation, the calculations provided by Marketin et al. are considered to be less reliable for odd mass and odd-odd nuclei.
The recent publication from Ney et al. (Ref.[69]) completes the previous work from the same authors (Ref.[70]) in providing a global, microscopic description of allowed and first-forbidden β -decay in even and odd nuclei from the valley of stability to the neutron drip-line. In their work, the authors choose a global Skyrme density functional and interpret it as a density-dependent effective interaction to calculate β -decay rates. The model uses the Finite-Amplitude Method (FAM) as a formulation of the random-phase approximation to speed the computation of nuclear response functions. As in odd-A and odd-odd nuclei the pairing is blocked and the HFB ground state contains a quasiparticle excitation, the calculations are more complex as the ground state is no longer invariant under time reversal. Therefore, in order to preserve time-reversal symmetry, the HFB blocked states are approximated using the Equal Filling Approximation (EFA). The EFA procedure is based on considering the unpaired nucleon as sitting half in a given orbital and the other half in the time-reversed partner. As an example, in the case of preserving spherical symmetry where the orbitals have the $2j + 1$ degeneracy the unpaired nucleon

is distributed among all possible angular momentum projections $m = -j, ..., j$ with equal probability $1/(2j + 1)$.
The nuclei we aim at studying in this thesis work belong to a region where β -decay half-lives are long (10 s-10 min range) and therefore the Q-values are rather small. In such cases, the few daughter states that contribute to the decay have an energy very close to the endpoint. The decay rate has a dependence on the fifth power of the difference between the two energies, so that even a small error in the Q-value might have a large effect on the β -decay rate. On the contrary, when the Q-value is large, many states contribute to the rate, and their energies are far from the endpoint. Because of this, the impact of errors in the Q-value on the rate is less important than errors in excitation energies or strengths.

In Fig. 5.10, our experimental measurements for β -decay half-lives mentioned in Sec. 5.1 are compared to the calculations performed in the framework of the three aforementioned models. The previously known data points are indicated by red squares, while the half-lives measured for the first time in this work are marked by open green diamonds. The three theoretical models are given by the dotted lines: Möller et al. (blue), Marketin et al. (yellow), Ney et al. (orange).

Data and predictions seem to scatter largely for the Po isotopic chain (upper panel), while they exhibit a constant trend in At and Rn ones (middle and bottom panels). An odd-even staggering is visible in the Rn isotopes, while this is less remarked in the Astatines. The theoretical models seem to agree better to the predictions in the Rn chain, while they largely deviate in At and, more markedly, for Po.

The three models predict a different balance between GT and FF transitions, of the order of 80% in Marketin et al., while being very small in the description of Möller et al.. This is at the basis of the predictions of shorter half-lives by the first model compared to the second, which becomes more evident at larger values of mass. The deviations seen between these predictions and the actual experimental values seem to point to a less important role of FF transitions, still, in this mass region. Further experimental data providing new half-lives and decay patterns will help elucidating the role of FF and GT transitions in this mass region.

Such results are important in the economy of the description of the r-process, since long decay times might indicate the existence of a bottleneck of the flow in this high-Z region, while faster decay flows will allow to reach heavy nuclei increasing Z rapidly.

We remind that these nuclei are at the limit of the fission recycling region, which contributes to the re-feeding of the r-process in two ways: providing new seed ions in the medium-mass region (around the humps of the fission fragment distribution), and providing fresh neutrons to be captured.

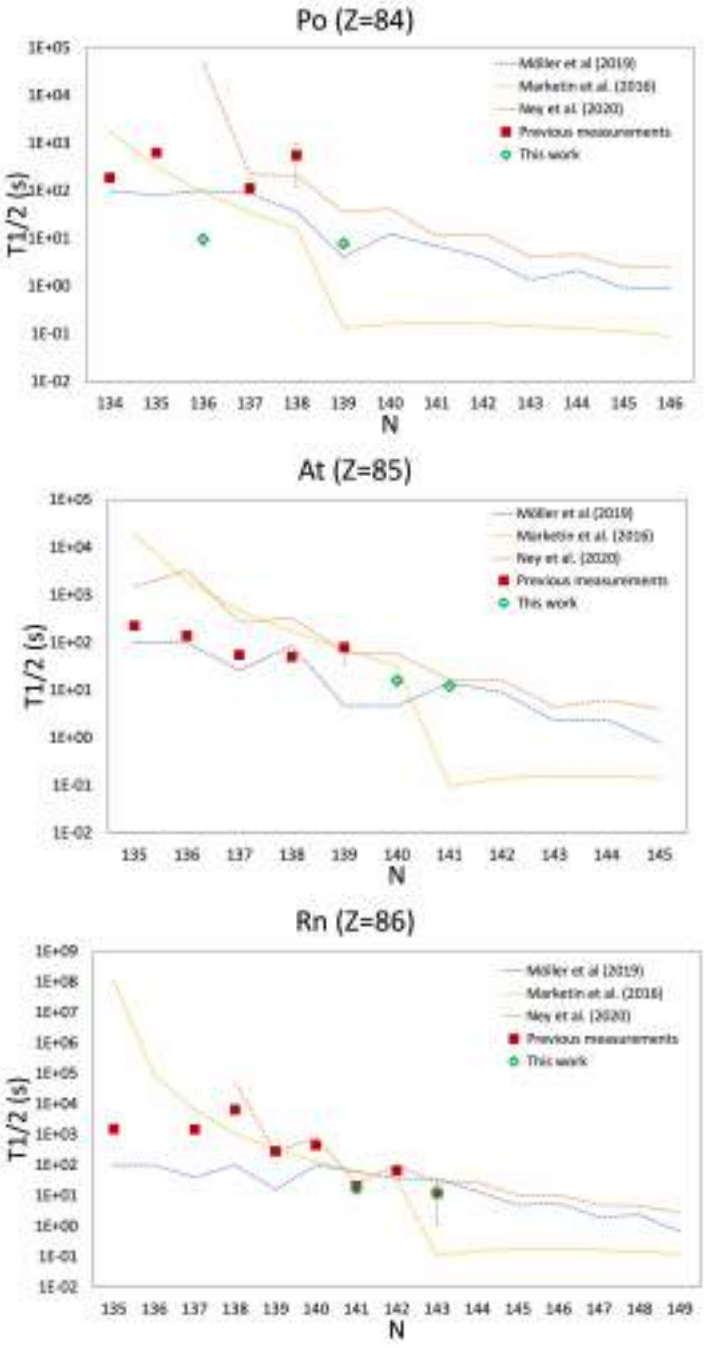

Figure 5.10: Comparison of our results (green diamonds) with literature values (red squares) and the results from the three theoretical models mentioned above: Ref. [67] (blue line), Ref. [68] (yellow line), Ref. [69] (orange line).

5.3 ^{100}Cd, ^{101}Cd and ^{102}Cd in *Dataset2*

5.3.1 What is known in the region

The region of the nuclide chart around ^{100}Sn is subject of a multitude of experimental and theoretical studies. Specific efforts have been directed towards assessing the robustness of the N=50 and Z=50 double shell closure, and the evolution of single-particle energies in this area of heavy nuclei, with similar proton and neutron numbers. In addition, being N$\sim$Z, the region is ideal to investigate the role of the proton-neutron pairing: protons and neutron occupy identical orbitals close to the Fermi energy, therefore the Pauli principle is lifted and both isoscalar (T=0) and isovector (T=1) proton-neutron-pair correlations are allowed.

Moreover, this is an ideal area to test the seniority symmetry, which describes the level scheme taking into account only the unpaired nucleons. The seniority scheme is established, in these nuclei, for a configuration of n protons with j=9/2 in the $g_{9/2}$ orbit. Deviations from this simple scheme have their origin in the mixing with close-by orbitals and by effect of core-excitations across the gap.

The long isotopic chains with Z around 50 serve as good testing grounds for nuclear models investigating the shell evolution and the interplay between pairing and quadruple correlations. Unlike the cases of Sn, in which the "generalized" seniority structure with neutron configurations can be expected in the low-lying states, understanding the situation in the Cd isotopic chain would be scientifically more challenging due to the enhancement of "collectivity" induced by two proton holes in $g_{9/2}$ orbits.

The difference between neighbouring isotopic chains is reflected in the trend of 2^+ energies: the E(2_1^+) in Pd, Te and Xe isotopic chain gradually increases with the neutron number towards N = 82, implying a smooth structural evolution from vibrational nature to a spherical shape. However, the situation in Cd isotopes is unusual: the 2_1^+ energy is rather constant, followed by a sudden increase in excitation energy in ^{130}Cd, indicating a different shape evolution with respect to nearby isotopes [71].

Proton-rich Cd isotopes have been recently revisited on the basis of the study of proton or β-delayed proton emission, with the refinement of half-lives measurements [72]. In addition, collinear laser spectroscopy data fixed spins and parities of the odd members of the chain, between A=101-109, confirming the $J^\pi=5/2^+$ ground state for all of them [73], and the electromagnetic moments, compared to Large-scale shell-model calculations using the SR88MHJM Hamiltonian, firmly establish the significance of the $\pi g_{9/2}$ contribution, and the importance of the joined filling, in particular of the close-lying $d_{5/2}$ and $g_{7/2}$ orbitals, for the observed nuclear structure.

The level scheme of p-rich Cd isotopes has been constructed on the basis of fusion-evaporation reactions, and is well assessed up to high spins. Details for each specific isotope will be given in the subsequent sections, together with the description of their decay.

5.3.2 Results on ^{100}Cd, ^{101}Cd and ^{102}Cd

The decay scheme of ^{100}Cd, ^{101}Cd and ^{102}Cd has been studied in *Dataset2* using γ - γ correlations and intensity measurements in the single germanium energy spectra. In Fig. 5.11, the total γ ray spectrum in coincidence with bPlast off spill is shown. The main peaks assigned to nuclei populated via β -decay are labelled. Many high-energy peaks could not be assigned and are labelled with a $*$ symbol.

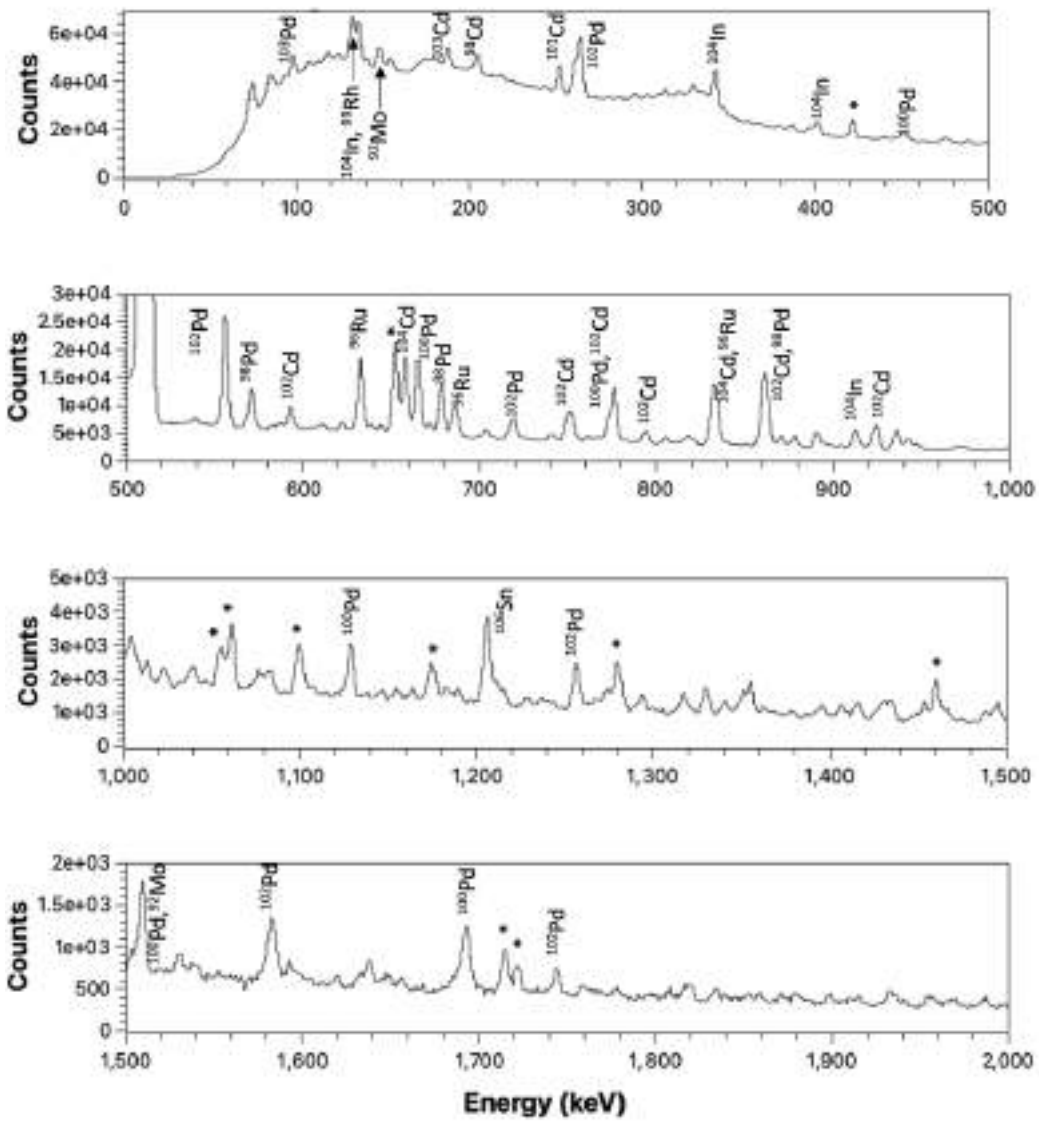

Figure 5.11: β -delayed γ -ray spectrum gated on off-spill βPlastic events. The strongest peaks are labelled, γ transitions which could not be assigned and are labelled with a $*$ symbol.

^{101}Cd

The decay scheme of ^{101}Cd is known from previous measurements, where the nucleus was produced and studied directly in an in-beam experiment. The reaction ^{58}Ni(^{50}Cr,2pαn)^{101}Cd was studied with the NORDBALL array [76], comprising a Neutron Wall and a Silicon Ball, and provided the level scheme in Fig.5.12 (left panel) [74].

The same nucleus was studied via β decay in Ref. [75], where the β -decay half-life was measured but only the first excited state at 252 keV could be placed in the level scheme (see Fig. 5.12, right panel). Other coincident γ rays could not be assigned to precise levels.

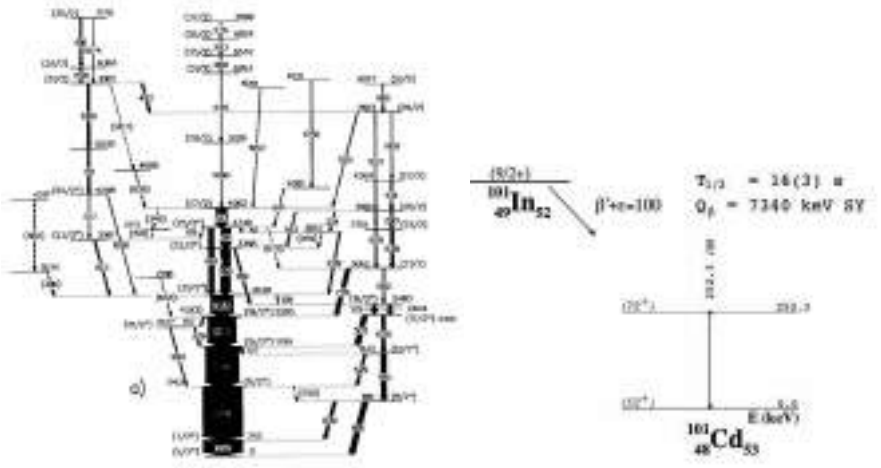

Figure 5.12: Left: Excited states of ^{101}Cd observed after the fusion-evaporation reaction ^{58}Ni(^{50}Cr,2pαn)^{101}Cd [74] (adapted from [74]. Right:Excited states of ^{101}Cd observed following the β decay of ^{101}In, [75] (adapted from [75]).

$J_i^\pi \rightarrow J_f^\pi$	E_x (keV)	E_γ (keV)	EM character	ICC	I_γ (%)
$7/2^+ \rightarrow 5/2^+$	252.90(27)	252.90(27)	$M1+E2$	0.048(11)	100(4)
$9/2^+ \rightarrow 7/2^+$	891.56(24)	640.43(34)	$M1+E2$	0.0036(2)	17(2)
$9/2^+ \rightarrow 5/2^+$	891.56(24)	891.56(24)	$E2$	0.00148(2)	35(6)
$11/2^+ \rightarrow 7/2^+$	1144.46(36)	891.56(24)	$E2$	0.00148(2)	30(6)

Table 5.3: γ -ray transitions assigned to ^{101}Cd. The following quantities are listed: the spin-parity of initial (J_i^π) and final (J_f^π) states, the energy of the initial level (E_x), the energy of the γ ray (E_γ), its electromagnetic character, its internal conversion coefficient (ICC) and its relative γ intensity (I_γ).

As mentioned in 4.8, at present we are not able to produce ion-β -γ correlation spectra, and the study of the decay scheme in these nuclei comes from the analysis of off-spill spectra in coincidence with the decay branch in AIDA and the β -plastic scintillator detectors. This has the advantage of maintaining a high statistics in the spectra, allowing for γ -γ coincidence studies.

We were, therefore, able, to extend the knowledge on β -delayed γ -ray transitions, by adding two levels to the β -delayed level scheme and providing I_β and $\log ft$ values.
In Fig. 5.13, the γ -γ coincidence transitions are shown. In the top panel, the 639- and 891-keV transitions are observed in coincidence with the 252 keV γ transition. In the bottom panel, instead, the 252- is observed in coincidence with the 891-keV line.

The measured γ transitions are reported in Tab. 5.3, extracted from germanium singles spectra, corrected for their efficiencies. The value of the γ relative intensity for the 891 keV transition, being a doublet in the previously-proposed level scheme (see Fig. 5.12), was extrapolated considering its relative intensity (58%) with respect to the 639 keV transition from the same level given by Ref. [74]. Internal conversion coefficients for the given γ transitions, accounting for negligible contribution, were calculated using the BrICC online calculator [77].

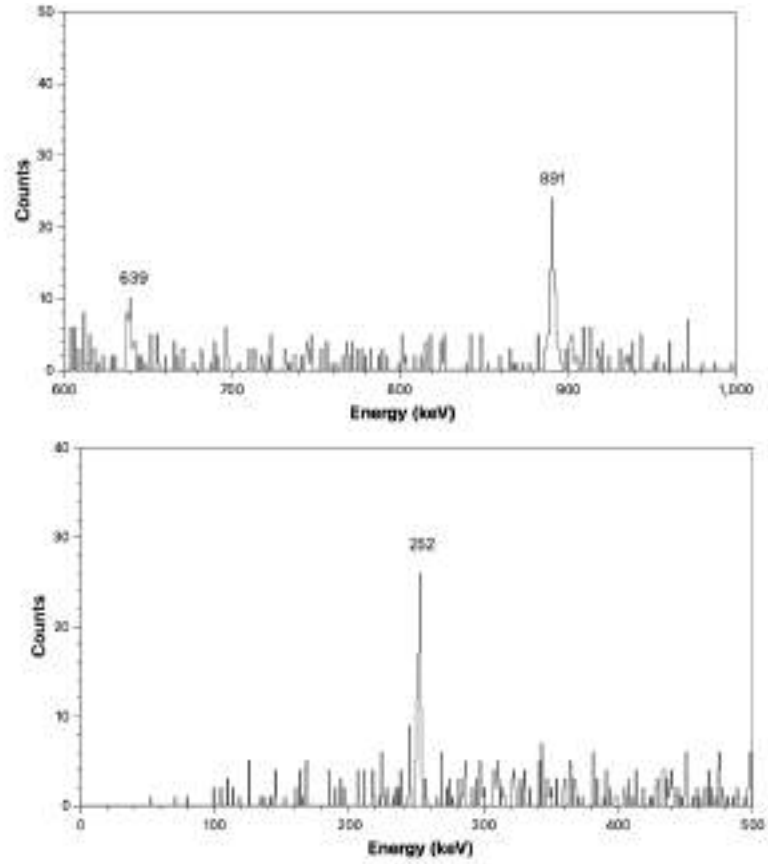

Figure 5.13: Gamma-ray spectra in coincidence with the 252 keV (top) and 891 keV transition (bottom).

In Tab. 5.4, the β intensities and logft values for the measured levels are listed. The β feedings (I_β) were calculated by subtracting the gamma intensities (I_γ) of the transitions which feed the level to the ones which depopulate the level itself: $I = I_\gamma^{(out)} - I_\gamma^{(in)}$, divided by the total feeding of the ground state. The beta feedings for each level was used to extract the logft value, using the online tool provided by the NNDC website [78]. In this work, the I_β and logft values given are referred to $\beta+$ and EC decays altogether, as the two contributions cannot be distinguished. The Q-value used for logft calculations in this work was calculated considering the mass ^{101}In reported in a recent publication [79]), obtaining the value $Q = 7291(5)$ keV. The ^{101}In β -decay half-life considered is a weighted value between Ref. [75] and [80], and amounts to $T_{1/2} = 15.1(3)$ s.

The aforementioned results are summarised in the proposed level scheme in Fig. 5.14, where transitions newly added to the β -delayed scheme are shown in red.

The results are compared to theoretical predictions, obtained using Large-Scale Shell Model calculations in the model space jj4_45, including proton $0f_{5/2}$, $1p_{3/2}$, $1p_{1/2}$, $0g_{9/2}$ orbitals and neutron orbitals $0f_{5/2}$, $1p_{3/2}$, $1p_{1/2}$, $0g_{9/2}$, $0g_{7/2}$, $1d_{5/2}$, $1d_{3/2}$, $2s_{1/2}$, $0h_{11/2}$ allowing for one particle one hole excitations between two major shells. The single particle energies of the Hamiltonian are fixed to nuclei around ^{90}Zr [81]. As it can be seen

J^π	E_x (keV)	Calculated E_x (keV)	I_β (%)	logft	Calculated logft
$(7/2^+)$	252.90(27)	219.0	41(6)	5.28(7)	6.0708
$(9/2^+)$	891.56(24)	974.0	37(5)	5.10(6)	6.1870
$(11/2^+)$	1144.46(36)	1055.0	22(5)	5.23(10)	6.2758

Table 5.4: I_β assigned to ^{101}Cd levels. The following quantities are listed: the spin-parity of the level (J^π), the energy of the initial level (E_x), its β intensity (I_β), logft value and logft value obtained with shell-model calculations.

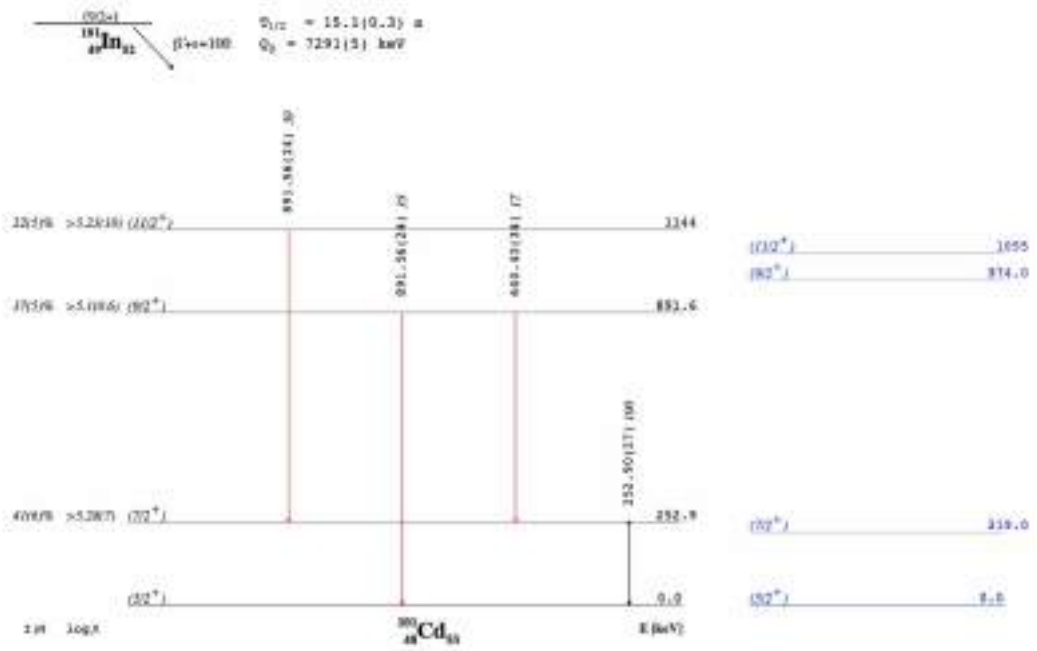

Figure 5.14: Decay scheme of ^{101}Cd obtained in this work (left panel), the level scheme obtained in the theoretical calculation is displayed in blue (right panel).

in Fig. 5.14, the levels energies and ordering, shown in blue, are in good agreement with the experimental values.

The theoretical calculation confirms that a proton in the $0g_{9/2}$ shell is converted into a neutron placed in the $0g_{7/2}$ shell in the daughter nucleus. As discussed in the previous section 5.3.1, the spin and parity of ^{101}Cd has been fixed by a collinear laser experiment to J$^\pi$=5/2$^+$, therefore ruling out the direct ground-state-to-ground-state feeding from the J$^\pi$=9/2$^+$ of the parent nucleus. The extracted I$_\beta$ values suggest a strong feeding to the first three excited state, supporting their spin and parity proposed assignments as $7/2^+$, $9/2^+$ and $11/2^+$, if an allowed character of the transition is assumed. The logft values obtained in this work are consistent with allowed β decay, as explained in Sec. 1.4.4. The calculated values point to a similar feeding pattern, even if the absolute value deviates from the experimental findings.

^{100}Cd

The β -delayed level scheme of ^{100}Cd was studied in previous years in Ref. [82]. In the work by Plettner et al., ^{100}Cd was populated via β decay, where the mother nucleus ^{100}In was produced in the reaction ^{50}Cr(^{58}Ni,αp3n)^{100}In. The β -delayed γ rays were measured using HPGe detectors of EUROBALL type and a total absorption spectrometer [83]. The resulting decay scheme is shown in Fig. 5.15.

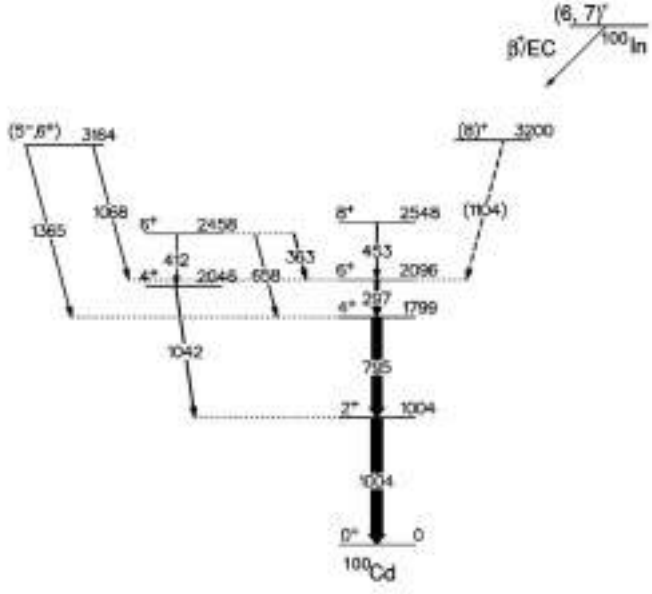

Figure 5.15: β -delayed level scheme of ^{100}Cd observed in Ref. [82] (adapted from [82]).

In our work, we have used γ -γ coincidences to confirm the previously proposed level scheme, as shown Fig. 5.16. In the top panel, the 297- and 795-keV transitions are observed in coincidence with the 1004 keV γ transition. In the middle panel, instead, the 297- and 1004-keV transitions are observed in coincidence with the 795-keV line. In the bottom panel, the 795- and 1004-keV transitions are observed in coincidence with the 297-keV line.

In Tab. 5.5, we list the values obtained in this work for I_γ transition probabilities for the three γ ray transitions.

$J_i^\pi \rightarrow J_f^\pi$	E_x (keV)	E_γ (keV)	EM character	ICC	I_γ (%)
$2^+ \rightarrow 0^+$	1004.9(17)	1004.9(17)	$E2$	0.001130(6)	100(6)
$4^{+(1)} \rightarrow 2^+$	1798.9(17)	794.99(5)	$M1+E2$	0.00195(3)	85(6)
$6^{+(1)} \rightarrow 4^{+(1)}$	2096.79(18)	269.91(5)	$M1+E2$	0.029(5)	39(3)

Table 5.5: γ -ray transitions assigned to ^{100}Cd. The following quantities are listed: the spin-parity of initial (J_i^π) and final (J_f^π) states, the energy of the initial level (E_x), the energy of the γ ray (E_γ), its electromagnetic character, its internal conversion coefficient (ICC) and its relative γ intensity (I_γ).

Unlike the previous measurements, the relative I_γs measured in this work suggest

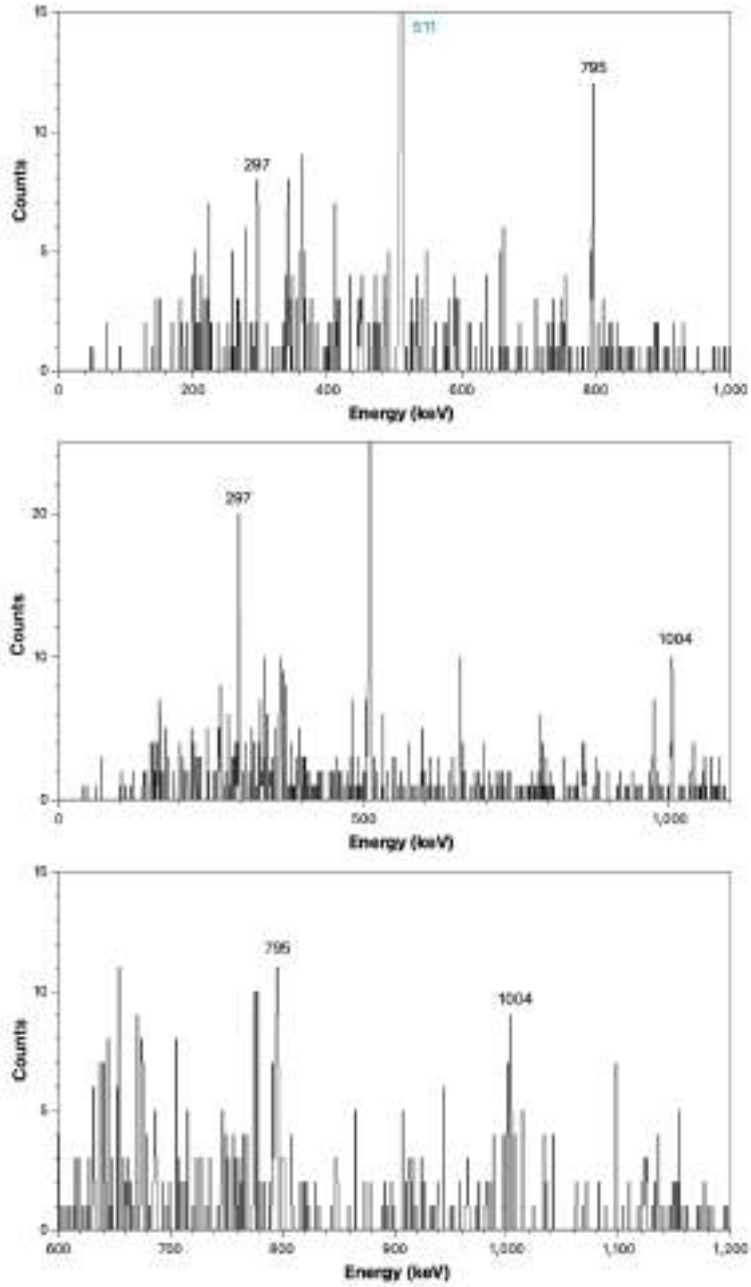

Figure 5.16: Gamma-ray spectra in coincidence with the 1004 keV (top), 795 keV (middle) and 297 keV transition (bottom).

a non-zero probability to populate the 1004 keV level directly via β decay. This could indicate the possibility of the existence of a low-spin isomer in ^{100}In, like the systematics for higher mass even In isotopes suggests. It is likely that this was not observed in Ref. [82] because of the use of a fusion-evaporation reaction to populate the mother nucleus, which

populates mainly yrast states.

^{101}In is part of our cocktail beam, but unfortunately the statistics collected for this nucleus is not sufficient to assess the existence of a long-living state excited by the fragmentation reaction. This will be followed up when proper ion-β γ correlations will be built, studying the decay pattern and decay half-lives of the γ -rays.

^{102}Cd

The nucleus ^{102}Cd was also studied in previous works via β decay, in Ref. [84], and the level scheme is reported in Fig. 5.17. Here, the mother nucleus ^{102}In was produced in the reaction ^{50}Cr(^{58}Ni,xpyn)^{102}In and the γ rays emitted by the daughter nucleus were measured using the Cluster Cube, a HPGe detector array [85] coupled to a total absorption spectrometer (TAS) [83].

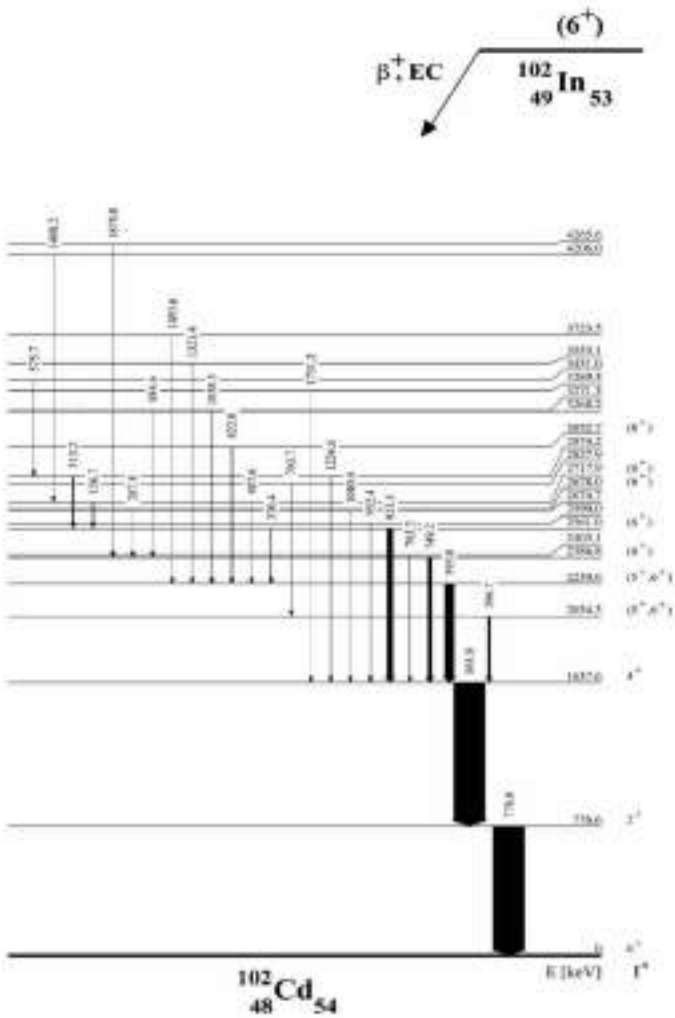

Figure 5.17: β -delayed level scheme of ^{102}Cd reported in Ref. [84] (adapted from [84]).

In this work, we have observed the transitions to the lowest spin levels and have assigned them to ^{102}Cd thanks to the analysis of γ -γ coincidence spectra, reported in Fig. 5.18 and Fig. 5.19. In the top panel of Fig. 5.18, we observe in coincidence with the 776 keV transition, the 397-, 593-, 749-, 861- and 923-keV transitions. The transitions marked in red belong to the de-excitation of ^{92}Mo ([86–88]), that has a transition at a similar energy (773 keV). In the middle panel of Fig. 5.18, we observe the 397-, 593-, 749-, 776- and 923-keV transitions in coincidence with the 861 keV transition. Here, the transitions marked in red belong to ^{98}Pd ([89]), which shows a transition with a very close energy value (863 keV). In the bottom panel of Fig. 5.18, we observe the 776- and 861-keV transitions in coincidence with the 396 keV line, while in red transitions belonging to ^{100}Pd ([90–92]) are shown and Compton background lines are labelled in green.

In Fig. 5.19, in the top panel we observe the 330-, 776- and 861-keV transitions in coincidence with the 596 keV line. In the middle panel we observe instead the 776- and 861-keV transitions in coincidence with the 749 keV line, where transitions belonging to ^{100}Pd are highlighted with red labels. In the bottom panel, the 776- and 861-keV transitions are observed in coincidence with the 923 keV transitions.

In Tab. 5.6, we report our measured values for the transitions energies and I_γ relative intensities.

$J_i^\pi \rightarrow J_f^\pi$	E_x (keV)	E_γ (keV)	EM character	ICC	I_γ (%)
$2^+ \rightarrow 0^+$	777.35(2)	777.35(2)	$E2$	0.00206(3)	100(2)
$4^+ \rightarrow 2^+$	1638.85(20)	861.5(2)	$E2$	0.001608(23)	90(12)
$(5^+, 6^+)^{(1)} \rightarrow 4^+$	2036.83(23)	397.98(14)	$M1+E2$	0.0126(8)	16(1)
$6^{+(1)} \rightarrow 4^+$	2236.83(26)	593.63(12)	$M1+E2$	0.00428(16)	12(6)
$(6^+)^{(2)} \rightarrow 4^+$	2389.52(22)	750.67(10)	$E2$	0.00241(16)	22(4)
$(6^+)^{(3)} \rightarrow 4^+$	2562.72(23)	923.87(11)	$E2$	0.001368(20)	21(3)

Table 5.6: γ -ray transitions assigned to ^{102}Cd. The following quantities are listed: the spin-parity of initial (J_i^π) and final (J_f^π) states, the energy of the initial level (E_x), the energy of the γ ray (E_γ), its electromagnetic character, its internal conversion coefficient (ICC) and its relative γ intensity (I_γ).

In this case, as in ^{100}Cd, we observe relative I_γs which is related to a non-zero probability to populate the 776 keV level directly via β decay. This suggests, also in this case, the possibility of the existence of a low-spin -decaying isomer in ^{102}In, like the systematics for higher mass even In isotopes suggest, which could not be observed in the previous studies [84].

To summarise, the results for ^{101}Cd point at allowed β decay transitions for the populated excitation levels. This is in good agreement with the shell-model calculations for the given nucleus, as described in Sec.5.3.2.

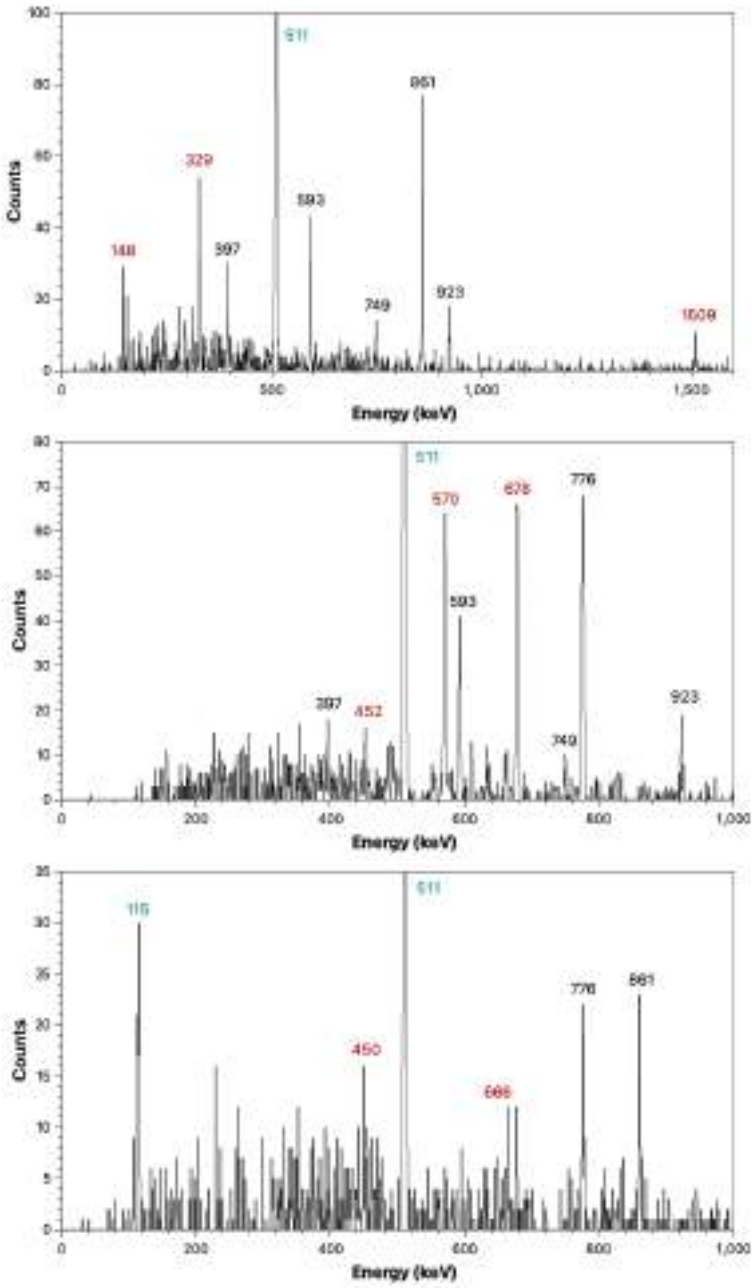

Figure 5.18: Gamma-ray spectra in coincidence with the 776 keV (top), 861 keV (middle) and 396 keV transition (bottom).

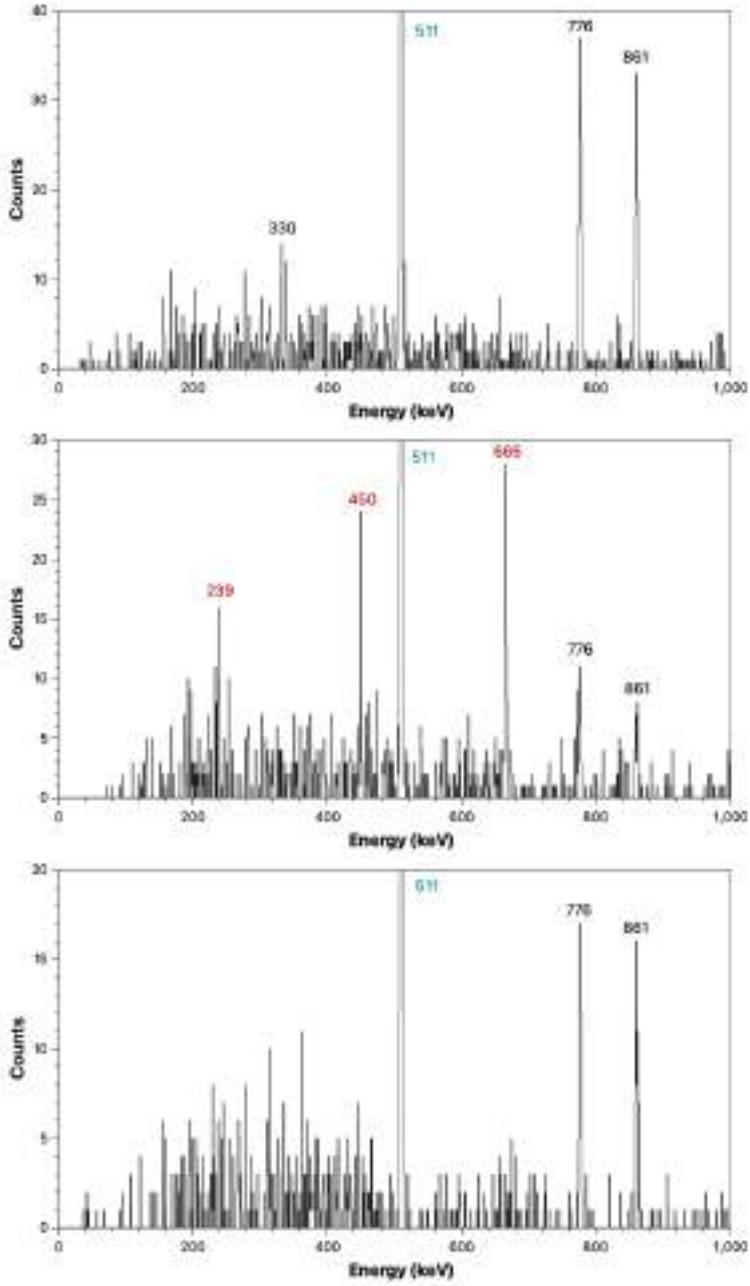

Figure 5.19: Gamma-ray spectra in coincidence with the 593 keV (top), 749 keV (middle) and 923 keV transition (bottom).

Conclusions and future directions

The work presented in this thesis is focused on experimental results from two experiments performed using the FRS+DESPEC setup at GSI-FAIR in spring 2021. The two experiments aimed at studying two different regions of the nuclear chart, extending from the heavy n-rich side around A$\sim$ 225 (*Dataset1*) towards the p-rich ^{100}Sn region (*Dataset2*) .

Information on β decay for nuclei in the A$\sim$ 225 region, being beyond N=126, is useful to test the predictions of global nuclear models in exotic nuclei, and describe the r-process of explosive nucleosynthesis. The proton-rich ^{100}Sn region, instead, is a great testing ground for nuclear models studying the evolution of shell structure and the interplay between pairing and quadrupole correlations.

The thesis describes the experimental set-up, data taking, and analysis procedures. First experimental results for the two datasets are reported on.

The main result from *Dataset1* is the measurement of β -decay half-lives in the populated nuclei. This provides a confirmation of previously obtained values in ^{227,229}Rn and a first measurement in ^{220,223}Po and ^{225,226}At. Several theoretical models are available to describe lifetimes in the region and the predictions vary largely. The competition between allowed and first forbidden transitions, expected to play a strong role in this region, is treated in different ways by the models pointing to a less important role of first forbidden transitions than expected in this mass region. Such results are important for the description of the r-process, since long decay times might indicate the existence of a bottleneck of the flow in this high-Z region, while faster decay flows would allow to reach heavy nuclei increasing Z rapidly.

The results from *Dataset2* allowed to extend the present knowledge of the β -delayed decay pattern in ^{100,101,102}Cd. New levels were added to the level scheme of ^{101}Cd, and the I_β and logft values were obtained for the first time for this decay. The I_β values suggest a strong feeding to the first three excited states, supporting their spin and parity proposed assignments. In addition the extracted logft values are consistent with allowed β decay. Large-scale shell model calculations were performed, showing a good agreement with the measured energies and logft values of those low-lying excited states. In ^{100,102}Cd, the measured relative γ -intensities suggest, the possibile existence of a low-spin isomer in ^{100,102}In, as observed for higher-mass even indium isotopes, but not reported in previous measurements.

Further developments in the analysis of both datasets are foreseen in the future. For *Dataset1*, we plan to work on the characterisation and removal of the high-background level in the β -delayed γ -ray spectra to study their decay scheme. This will allow to assess if any of the populated nuclei display octupole deformation. In *Dataset2*, the work will be mainly devoted to perform cleaner ion-β -γ correlations in order to be able to

isolate the β -delayed γ -ray spectrum for each implanted ion. With this, we would be able to assess with a higher precision the transitions and therefore the level schemes of each nuclei. Moreover, in both datasets, we plan to use the data provided by the FATIMA array to perform lifetimes measurements of β populated levels.

Appendices

APPENDIX A

Background sources in γ -ray spectra

The background spectrum in germanium detectors in shown in Fig. A.1, where energy peaks are marked with labels. The environmental background transitions are listed in Tab. A.1.

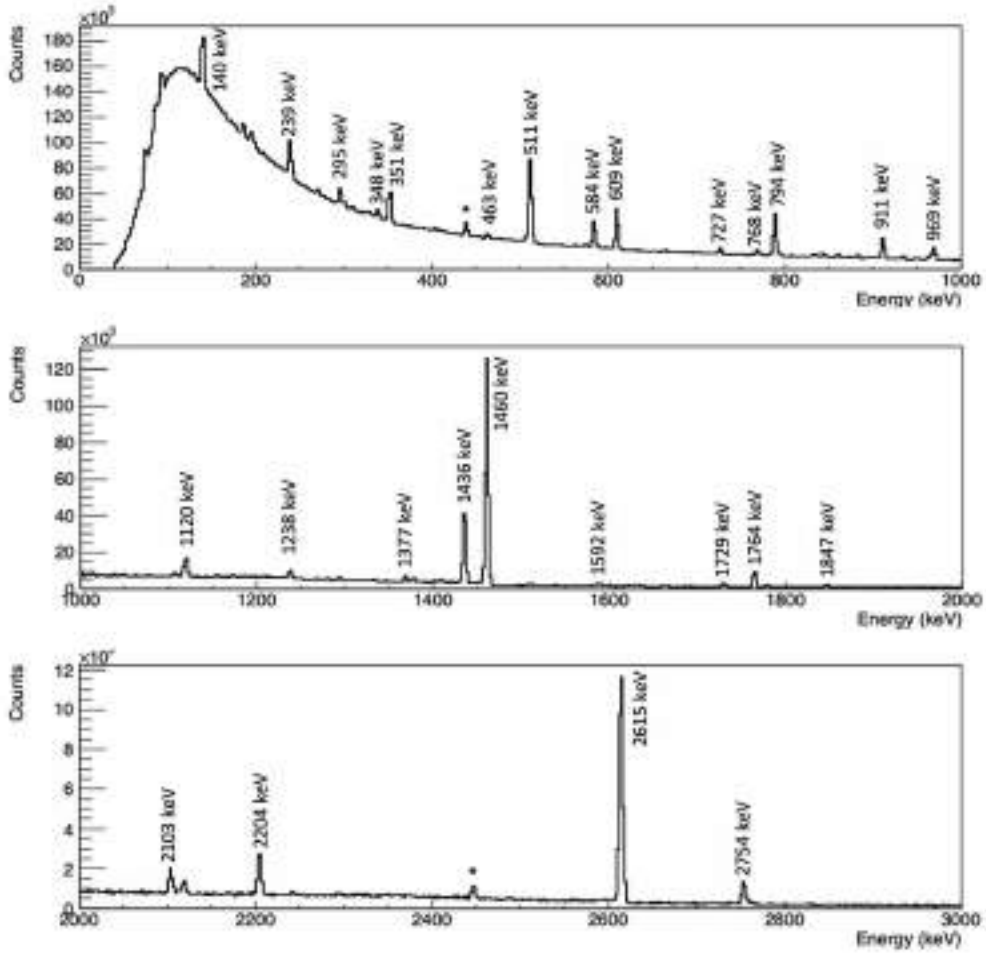

Figure A.1: Background spectrum in germanium detectors, energy peaks are marked with labels.

Energy (keV)	Transition	Nucleus
236	$1/2^+ \rightarrow 3/2^+$	^{227}Th $\xrightarrow{\alpha}$ ^{223}Ra
239	$0^{(-)} \rightarrow 1^{(-)}(g.s)$	^{212}Pb $\xrightarrow{\beta-}$ ^{212}Bi
241	$2^+ \rightarrow 0^+(g.s)$	^{212}Po $\xrightarrow{\alpha}$ ^{224}Ra
295	$1^- \rightarrow 1^-(g.s)$	^{214}Pb $\xrightarrow{\beta-}$ ^{214}Bi
338	$3^- \rightarrow 2^+$	^{228}Ac $\xrightarrow{\beta-}$ ^{228}Th
351	$3/2^+ \rightarrow 1/2^+(g.s)$	^{211}Bi $\xrightarrow{\alpha}$ ^{207}Tl
352	$0^-, 1^- \rightarrow 1^-(g.s)$	^{214}Pb $\xrightarrow{\beta-}$ ^{214}Bi
463	$4^+ \rightarrow 2^+$	^{228}Ac $\xrightarrow{\beta-}$ ^{228}Th
511		$e^- - e^+$ annihilation
584	$5^- \rightarrow 3^-$	^{212}Po $\xrightarrow{\alpha}$ ^{208}Pb
609	$2^+ \rightarrow 0^+(g.s)$	^{214}Bi $\xrightarrow{\beta-}$ ^{214}Po
727	$2^+ \rightarrow 0^+(g.s)$	^{212}Bi $\xrightarrow{\beta-}$ ^{212}Po
768	$2^+ \rightarrow 2^+(g.s)$	^{214}Bi $\xrightarrow{\beta-}$ ^{214}Po
794	$2^- \rightarrow 1^-$	^{228}Ac $\xrightarrow{\beta-}$ ^{228}Th
911	$2^+ \rightarrow 2^+$	^{228}Ac $\xrightarrow{\beta-}$ ^{228}Th
969	$2^+ \rightarrow 0^+$	^{228}Ac $\xrightarrow{\beta-}$ ^{228}Th
1120	$2^+ \rightarrow 0^+(g.s)$	^{214}Bi $\xrightarrow{\beta-}$ ^{214}Po
1238	$2^+ \rightarrow 2^+$	^{214}Bi $\xrightarrow{\beta-}$ ^{214}Po
1368	$2^+ \rightarrow 0^+$	^{24}Na $\xrightarrow{\beta-}$ ^{24}Mg
1377	$2^+ \rightarrow 0^+$	^{214}Bi $\xrightarrow{\beta-}$ ^{214}Po
1460	$2^+ \rightarrow 0^+(g.s)$	^{40}K $\xrightarrow{\epsilon}$ ^{40}Ar
1592		Double escape of 2615 keV
1620	$1^+ \rightarrow 0^+(g.s)$	^{212}Bi $\xrightarrow{\beta-}$ ^{212}Po
1729	$2^+ \rightarrow 0^+(g.s)$	^{214}Bi $\xrightarrow{\beta-}$ ^{214}Po
1764	$1^+ \rightarrow 0^+(g.s)$	^{214}Bi $\xrightarrow{\beta-}$ ^{214}Po
1847	$2^+ \rightarrow 0^+(g.s)$	^{214}Bi $\xrightarrow{\beta-}$ ^{214}Po
2103		Single escape of 2615 keV
2204	$1^+ \rightarrow 0^+(g.s)$	^{214}Bi $\xrightarrow{\beta-}$ ^{214}Po
2615	$3^- \rightarrow 0^+(g.s)$	^{212}Po $\xrightarrow{\alpha}$ ^{208}Pb
2754	$4^+ \rightarrow 2^+$	^{214}Bi $\xrightarrow{\beta-}$ ^{214}Po

Table A.1: Environmental background transitions.

The neutron induced γ -ray transitions in the FATIMA and HPGe detectors are listed in Tab. A.2 and Tab. A.4, respectively. The internal activity lines in FATIMA are listed in Tab. A.3.

Energy (keV)	Transition	Nucleus
166	$5/2^+ \rightarrow 3/2^+(g.s)$	^{139}La
217	$5/2^- \rightarrow 3/2^-(g.s)$	^{79}Br
275	$5/2^- \rightarrow 3/2^-(g.s)$	^{81}Br
306	$1/2^-, 3/2^- \rightarrow 3/2^-(g.s)$	^{79}Br
382	$5/2^+ \rightarrow 3/2^-(g.s)$	^{79}Br
398	$1/2^-, 3/2^- \rightarrow 3/2^-(g.s)$	^{79}Br
523	$5/2^- \rightarrow 3/2^-(g.s)$	^{79}Br
538	$1/2^-, 3/2^- \rightarrow 3/2^-(g.s)$	^{81}Br
560	$7/2^- \rightarrow 5/2^-(g.s)$	^{81}Br
566	$3/2^- \rightarrow 3/2^-(g.s)$	^{81}Br
767	$5/2^- \rightarrow 3/2^-(g.s)$	^{81}Br
789	$5/2^+ \rightarrow 3/2^-(g.s)$	^{81}Br
828	$3/2^- \rightarrow 3/2^-(g.s)$	^{81}Br
832	$1/2^-, 3/2^- \rightarrow 3/2^-(g.s)$	^{79}Br
836	$7/2^- \rightarrow 3/2^-(g.s)$	^{81}Br

Table A.2: Neutron induced γ -ray transitions in the FATIMA detectors.

Energy (keV)	Transition	Nucleus
789	$2^+ \rightarrow 0^+(g.s)$	$^{138}\text{La} \xrightarrow{\beta-} {}^{138}\text{Ce}$
1436	$2^+ \rightarrow 0^+(g.s)$	$^{138}\text{La} \xrightarrow{\epsilon} {}^{138}\text{Ba}$

Table A.3: Internal activity γ -ray transitions in the FATIMA detectors.

Energy (keV)	Transition	Nucleus
140	$7/2^+ \rightarrow 1/2^-(g.s)$	$^{74}\text{Ge}(n,\gamma)^{75}\text{Ge}^*$
596	$2^+ \rightarrow 0^+(g.s)$	$^{74}\text{Ge}(n,n'\gamma)^{74}\text{Ge}^*$

Table A.4: Neutron induced γ -ray transitions in the Germanium detectors.

APPENDIX B

Calibration coefficients for FATIMA and Germanium arrays

Germanium detectors were calibrated using a linear function as follows:

$$E_{HPGe}(keV) = A \times Ch_{HPGe} + B, \tag{B.1}$$

where Ch_{HPGe} is the ADC channel number, A and B are the calculated calibration coefficients. Tab. B.1 reports on the coefficients obtained for the 28 channels of the EUROBALL array, where the first column accounts for the channel, the second and third channel for coefficients A and B.

The calibration of the FATIMA detectors was performed with a third order polynomial function:

$$E_{FATIMA}(keV) = A \times Ch^3_{FATIMA} + B \times Ch^2_{FATIMA} + C \times Ch_{FATIMA} + D, \tag{B.2}$$

where Ch_{FATIMA} is the ADC channel number, A, B, C, D are the calculated calibration coefficients. The coefficients obtained for the 36 $LaBr_3$ detectors are listed in Tab. B.2, where in the first column the detector number is given, and in the others coefficients A, B, C, D are listed.

Channel	A	B
0	2.772492×10^{-3}	3.140516×10^{-1}
1	1.743406×10^{-3}	2.691045×10^{-1}
2	1.925030×10^{-3}	7.639626×10^{-2}
3	2.868216×10^{-3}	3.818794×10^{-1}
4	2.778265×10^{-3}	3.295770×10^{-2}
5	2.662915×10^{-3}	2.345621×10^{-1}
6	2.591360×10^{-3}	6.866065×10^{-1}
7	3.270474×10^{-3}	4.607764×10^{-1}
8	3.537539×10^{-3}	1.073704
9	3.297686×10^{-3}	9.492539×10^{-1}
10	3.625930×10^{-3}	-7.709081×10^{-2}
11	3.439862×10^{-3}	-7.028174×10^{-2}
12	3.576875×10^{-3}	2.423582×10^{-1}
13	1.790227×10^{-3}	3.938124×10^{-1}
14	3.524506×10^{-3}	8.569223×10^{-1}
15	4.894369×10^{-3}	8.978774×10^{-1}
16	5.280803×10^{-3}	-2.113560×10^{-1}
17	3.441664×10^{-3}	8.580371×10^{-1}
18	3.444186×10^{-3}	3.879673×10^{-1}
19	3.413445×10^{-3}	2.939780×10^{-1}
20	3.041359×10^{-3}	3.296505×10^{-1}
21	1.891441×10^{-3}	3.006256×10^{-1}
22	1.993352×10^{-3}	3.082964×10^{-1}
23	2.023123×10^{-3}	6.062046×10^{-1}
24	1.871989×10^{-3}	9.697276×10^{-2}
25	2.012769×10^{-3}	3.649300×10^{-1}
26	2.023858×10^{-3}	1.492218×10^{-1}
27	1.828219×10^{-3}	$-1.3772484 \times 10^{-1}$

Table B.1: Calibration coefficients of the HPGe array. The first column accounts for the channel, the second and third columns for coefficients A and B.

Channel	A	B	C	D
0	4.557478×10^{-11}	-4.884243×10^{-7}	1.296329×10^{-1}	-1.257799
1	4.119702×10^{-11}	-6.985598×10^{-7}	1.328557×10^{-1}	-1.603657
2	2.947629×10^{-11}	-6.689835×10^{-7}	1.349679×10^{-1}	1.029869
3	5.727859×10^{-11}	-6.308376×10^{-7}	1.313189×10^{-1}	0.848578
4	2.048536×10^{-11}	-5.991804×10^{-7}	1.326729×10^{-1}	1.226349
5	4.682707×10^{-11}	-5.905306×10^{-7}	1.308316×10^{-1}	0.725079
6	2.805433×10^{-11}	-4.737290×10^{-7}	1.338217×10^{-1}	1.561421
7	3.307706×10^{-11}	-6.262870×10^{-7}	1.329416×10^{-1}	2.010445
8	3.135305×10^{-11}	-4.395357×10^{-7}	1.319505×10^{-1}	1.306835
9	4.863571×10^{-11}	-8.204915×10^{-7}	1.336307×10^{-1}	1.171111
10	3.025484×10^{-11}	-6.391639×10^{-7}	1.338581×10^{-1}	1.546279
11	3.994982×10^{-11}	-3.038323×10^{-7}	1.307930×10^{-1}	1.775256
12	1.370958×10^{-10}	-1.230107×10^{-6}	1.368080×10^{-1}	5.578519
13	2.873724×10^{-11}	-5.144096×10^{-7}	1.308106×10^{-1}	7.060399
14	2.937065×10^{-11}	-2.118805×10^{-7}	1.282105×10^{-1}	4.755455
15	1.353535×10^{-11}	-3.015773×10^{-7}	1.299055×10^{-1}	4.128893
16	3.157872×10^{-11}	-2.000592×10^{-7}	1.273580×10^{-1}	1.762015
17	8.572955×10^{-11}	-6.705951×10^{-7}	1.268818×10^{-1}	-0.577355
18	1.962634×10^{-11}	-4.641828×10^{-7}	1.331751×10^{-1}	2.758113
19	9.047489×10^{-11}	-4.209197×10^{-7}	1.261530×10^{-1}	1.639334
20	6.139744×10^{-11}	-1.104772×10^{-6}	1.374363×10^{-1}	0.661419
21	1.246207×10^{-10}	-1.550096×10^{-6}	1.336566×10^{-1}	-1.105814
22	5.004671×10^{-11}	-3.558696×10^{-7}	1.298308×10^{-1}	1.299566
23	5.681122×10^{-11}	-5.626221×10^{-7}	1.310290×10^{-1}	-1.103228
24	7.909022×10^{-11}	-4.848092×10^{-7}	1.297349×10^{-1}	5.180081
25	2.534765×10^{-11}	-5.856928×10^{-7}	1.341268×10^{-1}	2.694365
26	8.783098×10^{-11}	-1.247496×10^{-6}	1.343974×10^{-1}	-0.839905
27	1.673113×10^{-11}	-2.413487×10^{-7}	1.257413×10^{-1}	0.179148
28	3.659789×10^{-11}	-2.186816×10^{-7}	1.316413×10^{-1}	1.697677
29	8.349148×10^{-11}	-7.139090×10^{-7}	1.296865×10^{-1}	0.175427
30	6.446615×10^{-11}	-3.654607×10^{-7}	1.278541×10^{-1}	2.546452
31	1.089538×10^{-11}	-1.111873×10^{-8}	1.299432×10^{-1}	3.085152
32	2.885911×10^{-11}	-5.506239×10^{-7}	1.318379×10^{-1}	-0.022099
33	1.852716×10^{-11}	-6.205129×10^{-7}	1.353605×10^{-1}	-0.228727
34	4.291262×10^{-11}	-6.017840×10^{-7}	1.329696×10^{-1}	1.228718
35	3.250709×10^{-11}	-5.186339×10^{-7}	1.352585×10^{-1}	-0.288213

Table B.2: Calibration coefficients of the FATIMA array. The first column accounts for the channel, the second, third, fourth and fifth columns for coefficients A, B, C, D.

Bibliography

[1] C. A. Bertulani. *Nuclear Physics in a Nutshell*. Princeton Univeristy Press, 2007.

[2] K.S. Krane. *Introductory Nuclear Physics*. John Wiley and Sons, 1988.

[3] A. Obertelli and H. Sagawa. *Nuclear Physics and Standard Model of Elementary Particles*. Springer, 2021.

[4] R. F. Casten. *Nuclear Structure from a Simple Perspective*. Oxford Studies in Nuclear Physics, 1990.

[5] J. Erler et al. "The limits of the nuclear landscape". In: *Nature* 486 (2012), pp. 509–512.

[6] S. R. Stroberg et al. "Ab Initio Limits of Atomic Nuclei". In: *Physical Review Letters* 126 (2021), pp. 022501–022501.

[7] Andrea Gottardo. "Isomer decay spectroscopy in the region of neutron-rich lead isotopes from relativistic ^{238}U fragmentation". PhD thesis. Università degli Studi di Padova, 2011.

[8] T. Kubo. "In-flight RI beam separator BigRIPS at RIKEN and elsewhere in Japan". In: *Nuclear Instruments and Methods in Physics Research Section B: Beam Interactions with Materials and Atoms* 204 (2003), pp. 97–113. DOI: https://doi.org/10.1016/S0168-583X(02)01896-7.

[9] A.S. Goldhaber. "Statistical models of fragmentation processes". In: *Physics Letters B* 53.4 (1974), p. 306. DOI: https://doi.org/10.1016/0370-2693(74)90388-8.

[10] Y. Eisenberg. "Interaction of Heavy Primary Cosmic Rays in Lead". In: *Physical Review* 96 (1954), pp. 1378–1382. DOI: https://doi.org/10.1103/PhysRev.96.1378.

[11] J.-J. Gaimard and K.-H. Schmidt. "A reexamination of the abrasion-ablation model for the description of the nuclear fragmentation reaction". In: *Nuclear Physics A* 531.3 (1991), pp. 709–745. DOI: https://doi.org/10.1016/0375-9474(91)90748-U.

[12] Fabio Farinon. "Unambiguous Identification and Investigation of Uranium Projectile Fragments Discovery of 63 New Neutron-rich Isotopes in the Element Range 61≤Z≤78 at the FRS". PhD thesis. Justus-Liebig Universität Gieβen, 2011.

[13] G. Benzoni. "β decay studies of the most exotic nuclei". In: *Proceedings of the International School of Physics "Enrico Fermi"* (2019).

[14] M.R. Mumpower et al. “The impact of individual nuclear properties on r-process nucleosynthesis”. In: *Progress in Particle and Nuclear Physics* 86 (2016), p. 86. DOI: https://doi.org/10.1016/j.ppnp.2015.09.001.

[15] K. L. Kratz. “Nuclear-data input to the classical r-process: The case of β-decay properties”. In: *AIP Conference Proceedings* 1852 (2017), p. 030001. DOI: https://doi.org/10.1063/1.4984852.

[16] E.M. Burbidge et al. “Synthesis of the Elements in Stars”. In: *Reviews of Modern Physics* 29 (1957), p. 547. DOI: https://doi.org/10.1103/RevModPhys.29.547.

[17] M. Arnould et al. “The r-process of stellar nucleosynthesis: Astrophysics and nuclear physics achievements and mysteries”. In: *Physics Reports* 450 (2007), p. 97. DOI: https://doi.org/10.1016/j.physrep.2007.06.002.

[18] H.E. Suess and H.C. Urey. “Abundances of the Elements”. In: *Reviews of Modern Physics* 28 (1956), p. 53. DOI: https://doi.org/10.1103/RevModPhys.28.53.

[19] *https://www.nasa.gov*. URL: https://www.nasa.gov.

[20] B. Pfeiffer et al. “Stellar and nuclear-physics constraints on two r-process components in the early galaxy”. In: *Nuclear Physics A* 688 (2001), p. 575. DOI: https://doi.org/10.1016/S0375-9474(01)00792-8.

[21] D. Argast et al. “Neutron star mergers versus core-collapse supernovae as dominant r-process sites in the early Galaxy”. In: *Astronom. Astrophys.* 416 (2004), p. 997. DOI: https://doi.org/10.1051/0004-6361:20034265.

[22] B. Pfeiffer et al. “Nuclear structure studies for the astrophysical r-process”. In: *Nuclear Physics A* 693 (2001), p. 282. DOI: https://doi.org/10.1016/S0375-9474(01)01141-1.

[23] E. Pian. “Spectroscopic identification of r-process nucleosynthesis in a double neutron-star merger”. In: *Nature* 551.7678 (2017), pp. 67–70. DOI: https://doi.org/10.1038/nature24298.

[24] W.J. Huang et al. “The Ame2020 atomic mass evaluation”. In: *Chinese Physics C* 45 (2021), p. 030002. DOI: https://doi.org/10.1088/1674-1137/abddb0.

[25] T. Kajino and G. J Mathews. “Impact of new data for neutron-rich heavy nuclei on theoretical models for r-process nucleosynthesis”. In: *Reports on Progress in Physics* 80 (2017), p. 084901. DOI: https://doi.org/10.1088/1361-6633/aa6a25.

[26] O. Hall et al. “β -delayed neutron emission of r-process nuclei at the N=82 shell closure”. In: *Physics Letters B* 816 (2021), p. 136266. DOI: https://doi.org/10.1016/j.physletb.2021.136266.

[27] *https://www.nndc.bnl.gov*. URL: https://www.nndc.bnl.gov.

[28] *https://www.gsi.de/en/*. URL: https://www.gsi.de/en/.

[29] H. Geissel et al. “The GSI projectile fragment separator (FRS): a versatile magnetic system for relativistic heavy ions”. In: *Nuclear Instruments and Methods in Physics Research Section B: Beam Interactions with Materials and Atoms* 70.1 (1992), pp. 286–297. DOI: https://doi.org/10.1016/0168-583X(92)95944-M.

[30] G. Münzenberg. “The separation techniques for secondary beams”. In: *Nuclear Instruments and Methods in Physics Research Section B: Beam Interactions with Materials and Atoms* 70.1 (1992), pp. 265–275. DOI: https://doi.org/10.1016/0168-583X(92)95942-K.

[31] F. Knoll. *Radiation Detection and Measurement*. USA: John Wiley & sons Inc., 2010.

[32] H. Geissel et al. "The Super-FRS project at GSI". In: *Nuclear Instruments and Methods in Physics Research Section B: Beam Interactions with Materials and Atoms* 204 (2003), p. 71. DOI: https://doi.org/10.1016/S0168-583X(02)01893-1.

[33] *https://wiki.gsi.de/pub/FRS/S2VTPC21/tpcmanual.pdf*. URL: https://wiki.gsi.de/pub/FRS/S2VTPC21/tpcmanual.pdf.

[34] *https://www-windows.gsi.de/frs/technical/FRSsetup/detectors/music.asp*. URL: https://www-windows.gsi.de/frs/technical/FRSsetup/detectors/music.asp.

[35] A. Mistry et al. "The DESPEC setup for GSI and FAIR". In: *Nuclear Instruments and Methods in Physics Research Section A: Accelerators, Spectrometers, Detectors and Associated Equipment* 1033.1 (2022), p. 166662. DOI: https://doi.org/10.1016/j.nima.2022.166662.

[36] *https://edms.cern.ch/ui/file/1865809/2/TDR_HISPEC_DESPEC_AIDA_public.pdf*. URL: https://edms.cern.ch/ui/file/1865809/2/TDR%7B%5C_%7DHISPEC%7B%5C_%7DDESPEC%7B%5C_%7DAIDA%7B%5C_%7Dpublic.pdf.

[37] *General machine timing system at GSI and FAIR, 2021*. URL: https://www-acc.gsi.de/wiki/Timing/WebHome.

[38] A.Banerjee et al. "Analog front-end for FPGA-based readout electronics for scintillation detectors". In: *Nuclear Instruments and Methods in Physics Research Section A: Accelerators, Spectrometers, Detectors and Associated Equipment* 1028 (2022), p. 166357. DOI: https://doi.org/10.1016/j.nima.2022.166357.

[39] M. Rudigier et al. "FATIMA - FAst TIMing Array for DESPEC at FAIR". In: *Nuclear Instruments and Methods in Physics Research Section A: Accelerators, Spectrometers, Detectors and Associated Equipment* 969.1 (2020), p. 163967. DOI: https://doi.org/10.1016/j.nima.2020.163967.

[40] *https://g-wiki.gsi.de/pub/SWiki/FATIMA/TDR_HISPEC_DESPEC_FATIMA_public.pdf*. URL: https://g-wiki.gsi.de/pub/SWiki/FATIMA/TDR%7B%5C_%7DHISPEC%7B%5C_%7DDESPEC%7B%5C_%7DFATIMA_public.pdf.

[41] J. Simpson. "The Euroball spectrometer". In: *Zeitschrift für Physik A - Hadrons and nuclei* 358 (1997), p. 139. DOI: https://doi.org/10.1007/s002180050290.

[42] J. Hoffmann. "New TASCA data acquisition hardware development for the search of element 119 and 120". In: *GSI Scientific Report 2011* 253 (2012), p. 13.

[43] O. B. Tarasov and D. Bazin. "LISE++: Radioactive beam production with in-flight separators". In: *Nuclear Instruments and Methods in Physics Research Section B: Beam Interactions with Materials and Atoms* 266 (2008), p. 4657. DOI: https://doi.org/10.1016/j.nimb.2008.05.110.

[44] J. Vesić et al. "Simulations of rare-isotope beams for the HISPEC/DESPEC experiments at the Super-FRS". In: *Nuclear Instruments and Methods in Physics Research Section A: Accelerators, Spectrometers, Detectors and Associated Equipment* (2022), p. 167714. DOI: https://doi.org/10.1016/j.nima.2022.167714.

[45] H. Weick et al. "Energy-loss straggling of (200–1000) MeV/u uranium ions". In: *Nuclear Instruments and Methods in Physics Research Section B: Beam Interactions with Materials and Atoms* 193 (2002), p. 1. DOI: https://doi.org/10.1016/S0168-583X(02)00718-8.

[46] H. Weick et al. “mproved accuracy of the code ATIMA for energy-loss of heavy ions in matter”. In: *GSI Scientific Report 2017* (2017).

[47] *http://web-docs.gsi.de/ weick/atima*. URL: http://web-docs.gsi.de/~weick/atima.

[48] D. J. Morrissey. “Systematics of momentum distributions from reactions with relativistic ions”. In: *Physical Review C* 39 (1989), p. 460. DOI: https://doi.org/10.1103/PhysRevC.39.460.

[49] K. Sümmerer. “Improved empirical parametrization of fragmentation cross sections”. In: *Physical Review C* 86 (2012), p. 014601. DOI: https://doi.org/10.1103/PhysRevC.86.014601.

[50] C. Scheidenberger et al. “Direct observation of systematic deviations from the Bethe stopping theory for relativistic heavy ions”. In: *Physical Review Letters* 73 (1994), p. 50. DOI: https://doi.org/10.1103/PhysRevLett.73.50.

[51] C. Scheidenberger et al. “Charge states of relativistic heavy ions in matter”. In: *Nuclear Instruments and Methods in Physics Research Section B: Beam Interactions with Materials and Atoms* 142.4 (1998), p. 441. DOI: https://doi.org/10.1016/S0168-583X(98)00244-4.

[52] G. Audi et al. “The Ame2012 atomic mass evaluation”. In: *Chinese Physics C* 36.12 (2012), p. 1287. DOI: https://doi.org/110.1088/1674-1137/36/12/002.

[53] W. J. Huang. “The Ame2016 atomic mass evaluation”. In: *Chinese Physics C* 41.3 (2017), p. 030002. DOI: https://doi.org/10.1088/1674-1137/41/3/030002.

[54] *https://radware.phy.ornl.gov/gf3/*. URL: https://radware.phy.ornl.gov/gf3/.

[55] D. A. Fink et al. “In-Source Laser Spectroscopy with the Laser Ion Source and Trap: First Direct Study of the Ground-State Properties of ^{217,219}Po”. In: *Physical Review X* 5 (2015), p. 011018. DOI: https://doi.org/10.1103/PhysRevX.5.011018.

[56] L. Chen et al. “Discovery and investigation of heavy neutron-rich isotopes with time-resolved Schottky spectrometry in the element range from thallium to actinium”. In: *Physics Letters B* 691.5 (2010), pp. 234–237. DOI: https://doi.org/10.1016/j.physletb.2010.05.078.

[57] P. A. Butler et al. “The observation of vibrating pear-shapes in radon nuclei”. In: *Nature Communications* 10 (2019), p. 2473. DOI: https://doi.org/10.1038/s41467-019-10494-5.

[58] D. G. Burke et al. “Search for stable octupole deformation in 225Fr”. In: *Nuclear Physics A* 612.1 (1997), pp. 91–142. DOI: https://doi.org/10.1016/S0375-9474(96)00311-9.

[59] W. Kurcewicz et al. “The nuclear structure of 227Fr”. In: *Nuclear Physics A* 621.4 (1997), pp. 827–852. DOI: https://doi.org/10.1016/S0375-9474(97)00190-5.

[60] S. Kreim et al. “Competition between pairing correlations and deformation from the odd-even mass staggering of francium and radium isotopes”. In: *Physical Review C* 90 (2014), p. 024301. DOI: https://doi.org/10.1103/PhysRevC.90.024301.

[61] K. Peräjärvi et al. “The beta-decay scheme of ^{232}Fr and the K = 0 ground-state band in ^{232}Ra”. In: *The European Physical Journal A - Hadrons and Nuclei* 21 (2004), pp. 7–10. DOI: https://doi.org/10.1140/epja/i2004-10038-4.

[62] W. Kurcewicz et al. "Collective states in ^{230}Ra fed by β -decay of ^{230}Fr". In: *Nuclear Physics A* 464.1 (1987), pp. 1–8. DOI: https://doi.org/10.1016/0375-9474(87)90418-0.

[63] S.Ciccone. *BDNE-Chart*. 2015. URL: https://github.com/ciccons/TRIUMF-BDNE-Chart.

[64] J. Liang et al. "Compilation and Evaluation of Beta-Delayed Neutron Emission Probabilities and Half-Lives for Z > 28 Precursors". In: *Nuclear Data Sheets* 168 (2020), pp. 1–116. DOI: https://doi.org/10.1016/j.nds.2020.09.001.

[65] D. Neidherr et al. "Discovery of ^{229}Rn and the Structure of the Heaviest Rn and Ra Isotopes from Penning-Trap Mass Measurements". In: *Physical Review Letters* 102 (2009), p. 112501. DOI: https://doi.org/10.1103/PhysRevLett.102.112501.

[66] T. Kurtukian-Nieto, J. Benlliure, and K.-H. Schmidt. "A new analysis method to determine β -decay half-lives in experiments with complex background". In: *Nuclear Instruments and Methods in Physics Research Section A: Accelerators, Spectrometers, Detectors and Associated Equipment* 589.3 (2008), pp. 472–483. DOI: https://doi.org/10.1016/j.nima.2008.02.098.

[67] P. Möller et al. "Nuclear properties for astrophysical and radioactive-ion-beam applications (II)". In: *Atomic Data and Nuclear Data Tables* 125 (2019), pp. 1–192. DOI: https://doi.org/10.1016/j.adt.2018.03.003.

[68] T. Marketin, L. Huther, and G. Martınez-Pinedo. "Large-scale evaluation of β-decay rates of r-process nuclei with the inclusion of first-forbidden transitions". In: *Physical Review C* 93 (2016), p. 025805. DOI: https://doi.org/10.1103/PhysRevC.93.025805.

[69] E. M. Ney et al. "Global description of β^- decay with the axially deformed Skyrme finite-amplitude method: Extension to odd-mass and odd-odd nuclei". In: *Physical Review C* 102 (2020), p. 034326. DOI: https://doi.org/10.1103/PhysRevC.102.034326.

[70] M. T. Mustonen and J. Engel. "Global description of β^- decay in even-even nuclei with the axially-deformed Skyrme finite-amplitude method". In: *Physical Review C* 93 (2016), p. 014304. DOI: https://doi.org/10.1103/PhysRevC.93.014304.

[71] T. R. Rodríguez, J. L. Egido, and A. Jungclaus. "On the origin of the anomalous behaviour of 2+ excitation energies in the neutron-rich Cd isotopes". In: *Physics Letters B* 668.5 (2008), pp. 410–413. DOI: https://doi.org/10.1016/j.physletb.2008.08.072.

[72] J. Park et al. "New and comprehensive β- and βp-decay spectroscopy results in the vicinity of ^{100}Sn". In: *Physical Review C* 99 (2019), p. 034313. DOI: https://doi.org/10.1103/PhysRevC.99.034313.

[73] D. T. Yordanov et al. "Spins and electromagnetic moments of $^{101-109}$Cd". In: *Physical Review C* 98 (2018), p. 011303. DOI: https://doi.org/10.1103/PhysRevC.98.011303.

[74] M. Palacz et al. "In-beam γ -ray spectroscopy of ^{101}Cd". In: *Nuclear Physics A* 608 (1996), pp. 227–242. DOI: https://doi.org/10.1016/0375-9474(96)00287-4.

[75] M. Huyse et al. "Decay Study of Neutron-Deficient of ^{101}In". In: *Zeitschrift for Physik A - Atomic Nuclei* 330 (1988), pp. 121–122. DOI: https://doi.org/10.1007/BF01287275.

[76] B. Herskind. "The NORDBALL — A multidetector system for the study of nuclear structure". In: *Nuclear Physics A* 447 (1986), pp. 395–412. DOI: https://doi.org/10.1016/0375-9474(86)90619-6.

[77] T. Kibédi et al. "Evaluation of theoretical conversion coefficients using BrIcc". In: *Nuclear Instruments and Methods in Physics Research Section A: Accelerators, Spectrometers, Detectors and Associated Equipment* 589 (2008), pp. 202–229. DOI: https://doi.org/10.1016/j.nima.2008.02.051.

[78] M. Emeric and A. Sonzogni. *https://www.nndc.bnl.gov/logft/*. URL: https://www.nndc.bnl.gov/logft/.

[79] M. Mougeot et al. "Mass measurements of $^{99-101}$In challenge ab initio nuclear theory of the nuclide ^{100}Sn". In: *Nature Physics* 17 (2021), pp. 1099–1103. DOI: https://doi.org/10.1038/s41567-021-01326-9.

[80] J. Szerypo et al. "Decay properties of ground–state and isomer of ^{103}In". In: *Zeitschrift für Physik A* 359 (1997), pp. 117–126. DOI: https://doi.org/10.1063/1.57353.

[81] Yuan Cenxi. Private Communication. 2022.

[82] C. Plettner et al. "β decay of ^{100}In". In: *Physical Review C* 66 (2002), p. 044319. DOI: https://doi.org/10.1103/PhysRevC.66.044319.

[83] M. Karny et al. "Coupling a total absorption spectrometer to the GSI on-line mass separator". In: *Nuclear Instruments and Methods in Physics Research Section B: Beam Interactions with Materials and Atoms* 126 (1997), pp. 411–415. DOI: https://doi.org/10.1016/S0168-583X(96)01007-5.

[84] M. Gierlik et al. "Gamow–Teller strength distribution near ^{100}Sn. The beta decay of ^{102}In". In: *Nuclear Physics A* 724 (2003), pp. 313–332. DOI: https://doi.org/10.1016/S0375-9474(03)01572-0.

[85] Z. Hu et al. "Energy and efficiency calibration of an array of six Euroball Cluster detectors used for beta-decay studies". In: *Nuclear Instruments and Methods in Physics Research Section A: Accelerators, Spectrometers, Detectors and Associated Equipment* 419.1 (1998), pp. 121–131. DOI: https://doi.org/10.1016/S0168-9002(98)01137-1.

[86] V. S. Belyavenko et al. "Study of the Decay Schemes of ^{89}Mo and ^{92}Tc Nuclei". In: *Izvestiya Akademii Nauk SSSR Serija Fiziceskaja* 49 (1985), p. 103.

[87] J. C. De Lange et al. "The level structure of 92Tc". In: *Nuclear Physics A* 258 (1976), pp. 141–151. DOI: https://doi.org/10.1016/0375-9474(76)90535-2.

[88] J. Konijn et al. *The Decay of 4.4 m ^{92}Tc*. Tech. rep. IKO 1967/1968 Progress,P24. 1968.

[89] Z. Hu et al. "β decay of ^{98}Ag : Evidence for the Gamow-Teller resonance near ^{100}Sn". In: *Physical Review C* 62 (2000), p. 064315. DOI: https://doi.org/10.1103/PhysRevC.62.064315.

[90] S. Rastikerdar et al. "The decay of 100Ag". In: *Journal of Physics G: Nuclear Physics* 9.5 (1983), p. 555. DOI: https://doi.org/10.1088/0305-4616/9/5/008.

[91] H. I. Hayakawa, I. Hyman, and J. K. P. Lee. "Decay of ^{100}Ag". In: *Physical Review C* 22 (1980), pp. 247–251. DOI: https://doi.org/10.1103/PhysRevC.22.247.

[92] L. Batist et al. “Gamow-Teller Strength Distribution in Beta-Decay of ^{100}Ag from Total-Absorption Gamma Spectrometry”. In: *Zeitschrift für Physik A - Hadrons and nuclei* A351 (1995), p. 149.

List of Publications of Marta Polettini

As of 30th January 2023

Refereed publications

Authors: J.J. Valiente-Dobón, R. Menegazzo, A. Goasduff, D. Agguiaro, P. Aguilera, F. Angelini, M. Balogh, D. Bazzacco, J. Benito, G. Benzoni, N. Bez, M. Bolognesi, S. Bottoni, D. Brugnara, S. Carollo, P. Cocconi, A. Cogo, J. Collado, F.C.L. Crespi, A. Ertoprak, R. Escudeiro, F. Galtarossa, E.R. Gamba, A. Gambalonga, B. Góngora Servín, A. Gottardo, A. Gozzelino, M. Gulmini, Z. Huang, T. Marchi, D. Mengoni, P. Modanese, D.R. Napoli, J. Pellumaj, R.M. Pérez-Vidal, S. Pigliapoco, E. Pilotto, L. Ramina, M. Rampazzo, W. Raniero, M. Rebeschini, K. Rezynkina, D. Rosso, M. Scarcioffolo, D. Scarpa, M. Sedlák, R. Smith, N. Toniolo, F. Veronese, V. Volpe, L. Zago, I. Zanon, G. Zhang, R. Abels, M.L. Allegrini, C. Aufranc, G. Baulieu, C. Belkhiria, M. Benettoni, D. Benini, M. Bentley, M. Biasotto, M. Blaizot, J. Blasco Miquel, C. Boiano, A. Boston, H. Boston, A. Boujrad, P. Bourgault, A. Bracco, S. Brambilla, I. Burrows, F. Camera, S. Capra, A. Capsoni, R. Cash, J.V. Civera, E. Clément, S. Coelli, M. Cordwell, L. Corradi, S. Coudert, G. De Angelis, L. De Ruvo, G. Debras, M. Del Fabbro, J. Diklić, N. Dosme, G. Duchene, B. Duclos, J. Dudouet, J. Eberth, S. Elloumi, C. Everett, S. Fantinel, M. Fillinger, E. Fioretto, C. Fransen, A. Gadea, L. Gibelin, V. González, J. Goupil, C. Görgen, A. Grant, K. Green, J. Ha, T. Hartnett, K. Henseler, H. Hess, R. Hirsch, C. Houarner, J. Jacob, T. Joannem, D.S. Judson, N. Karkour, M. Karolak, M. Kebbiri, J. Kieffer, M. Labiche, X. Lafay, P. Le Jeannic, A. Lefevre, E. Legay, F. Legruel, S. Lenzi, S. Leoni, D. Linget, M. Liptrot, A. López-Martens, A. Lotodé, L. Manara, L. Ménager, T. Mijatović, B. Million, A. Minarello, G. Montagnoli, P. Morrall, I. Mullacrane, J. Nyberg, G. Philippon, **M. Polettini**, F. Popieul, A. Pullia, F. Recchia, P. Reiter, G. Richardt, M. Rocchini, A. Roger, F. Saillant, E. Sanchis, Md.S.R. Laskar, G. Secci, M.-H. Sigward, J. Simpson, N. Solenne, F. Spee, A.M. Stefanini, O. Stézowski, S. Szilner, N. Templeton, Ch. Theisen, S. Thiel, F. Tomasi, S. Tzvetkov, D. Vigano, E. Viscione, O. Wieland, K. Wimmer, G. Wittwer and M. Zielińska, "Conceptual design of the AGATA 2π array at LNL",Nuclear Instruments and Methods in Physics Research Section A: Accelerators, Spectrometers, Detectors and Associated Equipment, Volume 1049, 2023, 168040, ISSN 0168-9002, https://doi.org/10.1016/j.nima.2023.168040

Authors: S. Jazrawi, A. Yaneva, **M. Polettini**, B. Das, P.H. Regan, M. Górska, B. Cederwall, J. Jolie, H.M. Albers, M.M.R. Chishti, A. Banerjee, N. Hubbard, A.K. Mistry, M. Rudigier, G. Benzoni, J. Gerl, A.M. Bruce, Zs Podolyák, B.S. Nara Singh, G.X. Zhang, S. Alhomaidhi, C. Appleton, T. Arici, A. Blazhev, T. Davinson, A. Esmaylzadeh, L.M. Fraile,

G. Häfner, O. Hall, P.R. John, V. Karayonchev, I. Koujoharov, N. Kurz, M. Mikolajczuk, N. Pietralla, S. Pietri, J.M. Regis, E. Sahin, L. Sexton, H. Schaffner, C. Scheidenberger, A. Sharma, J. Vesic, H. Weick, V. Werner, R. Lozeva, M. Si, "Commissioning the FAst TIMing array (FATIMA) at FAIR Phase-0: Half-lives of excited states in the N=50 isotones 96Pd and 94Ru", Radiation Physics and Chemistry, 2022, 110234, ISSN 0969-806X, https://doi.org/10.1016/j.radphyschem.2022.110234

Authors: A.K. Mistry, H.M. Albers, T. Arıcı, A. Banerjee, G. Benzoni, B. Cederwall, J. Gerl, M. Górska, O. Hall, N. Hubbard, I. Kojouharov, J. Jolie, T. Martinez, Zs. Podolyák, P.H. Regan, J.L. Tain, A. Tarifeno-Saldivia, H. Schaffner, V. Werner, G. Ağgez, J. Agramunt, U. Ahmed, O. Aktas, V. Alcayne, A. Algora, S. Alhomaidhi, F. Amjad, C. Appleton, M. Armstrong, M. Balogh, K. Banerjee, P. Bednarczyk, J. Benito, C. Bhattacharya, P. Black, A. Blazhev, S. Bottoni, P. Boutachkov, A. Bracco, A.M. Bruce, M. Brunet, C.G. Bruno, I. Burrows, F. Calvino, R.L. Canavan, D. Cano-Ott, M.M.R. Chishti, P. Coleman-Smith, M.L. Cortés, G. Cortes, F. Crespi, B. Das, T. Davinson, A. De Blas, T. Dickel, M. Doncel, A. Ertoprak, A. Esmaylzadeh, B. Fornal, L.M. Fraile, F. Galtarossa, A. Gottardo, V. Guadilla, J. Ha, E. Haettner, G. Häfner, H. Heggen, P. Herrmann, C. Hornung, S. Jazrawi, P.R. John, A. Jokinen, C.E. Jones, D. Kahl, V. Karayonchev, E. Kazantseva, R. Kern, L. Knafla, R. Knöbel, P. Koseoglou, G. Kosir, D. Kostyleva, N. Kurz, N. Kuzminchuk, M. Labiche, J. Lawson, I. Lazarus, S.M. Lenzi, S. Leoni, M. Llanos-Expósito, R. Lozeva, A. Maj, J.K. Meena, E. Mendoza, R. Menegazzo, D. Mengoni, T.J. Mertzimekis, M. Mikolajczuk, B. Million, N. Mont-Geli, A.I. Morales, P. Morral, I. Mukha, J.R. Murias, E. Nacher, P. Napiralla, D.R. Napoli, B.S. Nara-Singh, D. O'Donnell, S.E.A. Orrigo, R.D. Page, R. Palit, M. Pallas, J. Pellumaj, S. Pelonis, H. Pentilla, A. Pérez de Rada, R.M. Pérez-Vidal, C.M. Petrache, N. Pietralla, S. Pietri, S. Pigliapoco, J. Plaza, **M. Polettini**, C. Porzio, V.F.E. Pucknell, F. Recchia, P. Reiter, K. Rezynkina, S. Rinta-Antila, E. Rocco, H.A. Rösch, P. Roy, B. Rubio, M. Rudigier, P. Ruotsalainen, S. Saha, E. Şahin, Ch. Scheidenberger, D.A. Seddon, L. Sexton, A. Sharma, M. Si, J. Simpson, A. Smith, R. Smith, P.A. Söderström, A. Sood, A. Soylu, Y.K. Tanaka, J.J. Valiente-Dobón, P. Vasileiou, J. Vasiljevic, J. Vesic, D. Villamarin, H. Weick, M. Wiebusch, J. Wiederhold, O. Wieland, H.J. Wollersheim, P.J. Woods, A. Yaneva, I. Zanon, G. Zhang, J. Zhao, R. Zidarova, G. Zimba, A. Zyriliou, "The DESPEC setup for GSI and FAIR", Nuclear Instruments and Methods in Physics Research Section A: Accelerators, Spectrometers, Detectors and Associated Equipment, Volume 1033, 2022, 166662, ISSN 0168-9002,
https://doi.org/10.1016/j.nima.2022.166662

Authors: N. Marchini, A. Nannini, M. Ottanelli, A. Saltarelli, G. Benzoni, E. R. Gamba, A. Goasduff, A. Gottardo, J. Ha, T. Krings, M. Perri, **M. Polettini**, M. Rocchini, and P. Sona, "Electric monopole transitions and structure of low-spin states in ^{106}Pd", Phys. Rev. C, Volume 105, 2022, 054304, https://doi.org/10.1103/PhysRevC.105.054304

Authors: B. Das, B. Cederwall, C. Qi, M. Górska, P. H. Regan, Ö. Aktas, H. M. Albers, A. Banerjee, M. M. R. Chishti, J. Gerl, N. Hubbard, S. Jazrawi, J. Jolie, A. K. Mistry, **M. Polettini**, A. Yaneva, S. Alhomaidhi, J. Zhao, T. Arici, S. Bagchi, G. Benzoni, P. Boutachkov,2 T. Davinson, T. Dickel, E. Haettner, O. Hall, Ch. Hornung, J. P. Hucka, P. R. John, I. Kojouharov, R. Knöbel, D. Kostyleva, N. Kuzminchuk, I. Mukha, W. R. Plass, B. S. Nara Singh, J. Vasiljevic,1 S. Pietri, Zs. Podolyák, M. Rudigier, H. Rösch, E. Sahin, H. Schaffner, C. Scheidenberger, F. Schirru, A. Sharma, R. Shearman, Y. Tanaka, J. Vesic, H. Weick, H. J. Wollersheim, U. Ahmed, A. Algora, C. Appleton, J. Benito, A. Blazhev, A. Bracco, A. M. Bruce, M. Brunet, R. Canavan, A. Esmaylzadeh, L. M. Fraile, G.

Häfner, H. Heggen, D. Kahl, V. Karayonchev, R. Kern, A. Korgul, G. Kosir, N. Kurz, R. Lozeva, M. Mikolajczuk, P. Napiralla, R. Page, C. M. Petrache, N. Pietralla, J.-M. Régis, P. Ruotsalainen, L. Sexton, V. Sanchez-Temble, M. Si, J. Vilhena, V. Werner, J. Wiederhold, W. Witt, P. J. Woods, and G. Zimba, "Nature of seniority symmetry breaking in the semimagic nucleus ^{94}Ru", Phys. Rev. C, Volume 105, 2022, L031304, ISSN 24699993 24699985, https://doi.org/10.1103/PhysRevC.105.L031304

Authors: Akashrup Banerjee, Michael Wiebusch, **Marta Polettini**, Andrew Mistry, Henning Heggen, Henning Schaffner, Helena M. Albers, Nikolaus Kurz, Magda Górska, Jürgen Gerl, "Analog front-end for FPGA-based readout electronics for scintillation detectors", Nuclear Instruments and Methods in Physics Research Section A: Accelerators, Spectrometers, Detectors and Associated Equipment, Volume 1028, 2022, 166357, ISSN 0168-9002,
https://doi.org/10.1016/j.nima.2022.166357

Authors: A. Goasduff, D. Mengoni, F. Recchia, J.J. Valiente-Dobón, R. Menegazzo, G. Benzoni, D. Barrientos, M. Bellato, N. Bez, M. Biasotto, N. Blasi, C. Boiano, A. Boso, S. Bottoni, A. Bracco, S. Brambilla, D. Brugnara, F. Camera, S. Capra, A. Capsoni, P. Cocconi, S. Coelli, M.L. Cortés, F.C.L. Crespi, G. de Angelis, F.J. Egea, C. Fanin, S. Fantinel, A. Gadea, E.R. Gamba, A. Gambalonga, C. Gesmundo, G. Gosta, A. Gottardo, A. Gozzelino, E.T. Gregor, M. Gulmini, J. Ha, K. Hadyńska-Klęk, A. Illana, R. Isocrate, G. Jaworski, P.R. John, S.M. Lenzi, S. Leoni, S. Lunardi, M. Magalini, N. Marchini, B. Million, V. Modamio, A. Nannini, D.R. Napoli, G. Pasqualato, J. Pellumaj, R.M. Pérez-Vidal, S. Pigliapoco, **M. Polettini**, C. Porzio, A. Pullia, L. Ramina, G. Rampazzo, M. Rampazzo, M. Rebeschini, K. Rezynkina, M. Rocchini, M. Romanato, D. Rosso, A. Saltarelli, M. Scarcioffolo, M. Siciliano, D.A. Testov, D. Tomasella, F. Tomasi, N. Toniolo, C.A. Ur, S. Ventura, F. Veronese, E. Viscione, V. Volpe, O. Wieland, I. Zanon, S. Ziliani, G. Zhang, D. Bazzacco, "The GALILEO γ -ray array at the Legnaro National Laboratories", Nuclear Instruments and Methods in Physics Research Section A: Accelerators, Spectrometers, Detectors and Associated Equipment, Volume 1015, 2021, 165753, ISSN 0168-9002, https://doi.org/10.1016/j.nima.2021.165753

Publications under review

Authors: **M. Polettini**, G. Benzoni, J. Pellumaj, J. J. Valiente-Dobón, G. Zhang, D. Mengoni, R. M. Perez Vidal, Z. Huang, N. Hubbard, H. M. Albers, A. Bracco on behalf of the HISPEC-DESPEC collaboration for S460 experiment, "β -decay half-lives measurements in A$\sim$225 Po-Fr nuclei", accepted by Acta Physica Polonica B: Proceedings Supplement

Authors: **M. Polettini**, G. Benzoni, J. Pellumaj, J. J. Valiente-Dobón, G. Zhang, D. Mengoni, R. M. Perez Vidal, Z. Huang, A. Bracco for the HISPEC-DESPEC collaboration for S460 experiment, "β -decay studies in the 220 $<$A$<$ 230 Po-Fr region", submitted to Journal of Physics: Conference Series (INPC 2022)

M.M.R. Chishti, S. Jazrawi, R. Shearman, P.H. Regan, Zs. Podolyák, S.M. Collins, M. Górska, B. Cederwall, A. Yaneva, G.X. Zhang, A. Goasduff, H.M. Albers, S. Alhomaidhi, A. Banerjee, A.M. Bruce, G. Benzoni, B. Das, T. Davinson, L.M. Fraile, J. Gerl, G. Häfner, J. Jolie, N. Hubbard, P.R. John, R. Lozeva, A.K. Mistry, B.S. Nara Singh, M. Mikolajczuk, **M. Polettini**, N. Pietralla, J.M. Regis, M. Rudigier, E. Sahin, A. Sharma, M. Si, J. Vesic, V. Werner, "Response of the FAst TIMing Array (FATIMA) for DESPEC at FAIR Phase-0", submitted to Nuclear Instruments and Methods in Physics Research Section A: Accelera-

tors, Spectrometers, Detectors and Associated Equipment

Publications in conference proceedings

Authors: **M. Polettini** for the S460 experiment and HISPEC-DESPEC Collaboration, "Beta decay studies and search for octupole deformation in the A∼225 Po-Fr nuclei", EPJ Web of Conferences 268, 00009 (2022) - LNES 2021,
https://doi.org/10.1051/epjconf/202226800009

Authors: **M. Polettini**, J. Pellumaj, G. Benzoni, J. J. Valiente-Dobón, G. Zhang, D. Mengoni, R. M. Perez Vidal, D. Genna, A. Bracco, G. Aggez U. Ahmed, Ö. Aktas, M. Al Aqueel, B. Alayed, H. M. Albers, A. Algora, S. Alhomaidhi, C. Appleton, T. Arici, M. Armstrong, K. Arnswald, M. Balogh, A. Banerjee, J. Benito Garcia, A. Blazhev, S. Bottoni, P. Boutachkov, A. Bruce, C. Bruno, F. Camera, B. Cederwall, M. M. R. Chishti, M. L. Cortés, D. M. Cox, F. C. L. Crespi, B. Das, T. Davinson, G. De Angelis, T. Dickel, M. Doncel, R. Donthi, A. Ertoprak, R. Escudeiro, A. Esmaylzadeh, L. M. Fraile, L. Gaffney, E. R. Gamba, J. Gerl, M. Górska, A. Gottardo, J. Ha, E. Haettner, O. Hall, H. Heggen, Y. Hrabar, N. Hubbard, S. Jazrawi, P. R. John, J. Jolie, C. Jones, D. Joss, D. Judson, D. Kahl, V. Karayonchev, E. Kazantseva, R. Kern, L. Knafla, I. Kojouharov, A. Korgul, W. Korten, P. Koseoglou, G. Kosir, D. Kostyleva, T. Kurtukian-Nieto, N. Kurz, N. Kuzminchuk, M. Labiche, S. Lenzi, S. Leoni, M. Llanos Expósito, R. Lozeva, T. J. Mertzimekis, M. Mikolajczuk, B. Million, A. K. Mistry, A. Morales, I. Mukha, J. R. Murias, D. Napoli, B. S. Nara Singh, D. O'Donnell, S. E. A. Orrigo, R. Page, S. Pelonis, J. Petrovic, N. Pietralla, S. Pietri, S. Pigliapoco, Zs. Podolyak, C. Porzio, B. Quintana Arnes, F. Recchia, P. H. Regan, J.-M. Régis, P. Reiter, K. Rezynkina, P. Roy, M. Rudigier, P. Ruotsalainen, E. Sahin, L. G. Sarmiento, M.-M. Satrazani, H. Schaffner, C. Scheidenberger, L. Sexton, A. Sharma, J. Smallcombe, P.-A. Söderström, A. Sood, P. Vasileiou, J. Vesic, J. Vilhena, L. Waring, H. Weick, V. Werner, J. Wiederhold, O. Wieland, K. Wimmer, H. J. Wollersheim, P. Woods, A. Yaneva, I. Zanon, J. Zhao, R. Zidarova, S. Ziliani, G. Zimba, A. Zyriliou, "Decay studies in the A∼225 Po-Fr region from the DESPEC campaign at GSI in 2021", IL NUOVO CIMENTO 45 C (2022) 125, https://doi.org/10.1393/ncc/i2022-22125-5

Authors: S. Capra, S. Ziliani, A. Goasduff, S. Leoni, A. Pullia, G. Benzoni, S. Bottoni, F. Camera, F. C. L. Crespi, E Gamba, L. Iskra, B. Million, **M. Polettini**, O. Wieland, B. Fornal, N. Cieplicka-Orynczak, M. Ciemala, J. Duenas, A. Gadea, D. Mengoni, D. Brugnara, L. Cortes, A. Gottardo, E. Gregor, G. Pasqualato, F. Recchia, J. J. Valiente Dobon, J. Pellumaj, I. Zanon, G. Zhang, F. Galtarossa, "GALTRACE: A highly segmented silicon detector array for charged particle spectroscopy and discrimination", IL NUOVO CIMENTO 45 C (2022) 98, https://doi.org/10.1393/ncc/i2022-22098-3

Authors: **M. Polettini**, S. Jazrawi, M. M. R. Chishti, A. Yaneva, B. Das, A. Banerjee, N. Hubbard, A. K. Mistry, H. M. Albers, R. Shearman, M. Górska, J. Gerl, P. H. Regan, B. Cederwall, J. Jolie, S. Alhomaidhi, T. Arici, G. Benzoni, P. Boutachkov, T. Davinson, T. Dickel, E. aettner, O. Hall, H. Heggen, P. R. John, I. Kojouharov, N. Kurz, B. S. Nara Singh, S. ietri, Zs. Podolyak, M. Rudigier, E. Sahin, H. Schaffner, C. Scheidenberger, A. Sharma, J. Vesic, H. Weick, H. J. Wollersheim, U. Ahmed, Ö. Aktas, A. Algora, C. Appleton, J. enito, A. Blazhev, A. Bracco, A. Bruce, M. Brunet, R. Canavan, A. Esmaylzadeh, L. M. raile, H. Grawe, G. Häfner, D. Kahl, V. Karayonchev, R. Kern, G. Kosir, R. Lozeva, P. apiralla, R. Page, C. M. Petrache, J. Petrovic, N. Pietralla, J.-M. Régis, P. uotsalainen, L. Sexton, V. Sanchez-Temble, M. Si, J. Vilhena, V. Werner, J. Wiederhold, W. Witt, P. Woods,

G. Zimba "DESPEC Phase-0 campaign at GSI", IL NUOVO CIMENTO 44 C (2021) 67, https://doi.org/10.1393/ncc/i2021-21067-8

Authors: Akashrup Banerjee, **Marta Polettini**, Henning Heggen, Henning Schaffner, Michael Wiebusch, Michael Traxler, Nikolaus Kurz, and Jürgen Gerl "Ultra short nuclear lifetimes measured with fast detectors and faster electronics", Proc. SPIE 11494, Hard X-Ray, Gamma-Ray, and Neutron Detector Physics XXII, 1149405 (20 August 2020), https://doi.org/10.1117/12.2567973